

ABSTRACT

MAHALE, TUSHAR RAMKRISHNA. Electron Beam Melting of Advanced Materials and Structures. (Under the direction of Denis Cormier and Ola Harrysson).

Layered manufacturing has for long been used for the fabrication of non-functional parts using polymer-based processes. Developments in laser beam and electron beam welding technologies and their adoption to layered manufacturing has made it possible to fabricate high-density functional parts in metal irrespective of the level of complexity. The Electron Beam Melting (EBM) process by Arcam AB is one such layered manufacturing process that utilizes a focused electron beam to process metal powder, layer by layer, in a vacuum environment. Research conducted as part of this body of work looks into the development of both bulk materials in the form of metal alloys and ceramic metal-matrix composites as well as the development of tunable mechanical & thermal metamaterials. Simulation models to approximate electron beam melting were suggested using commercial finite element analysis packages. A framework was developed based on the finite difference method to simulate layered manufacturing using Arcam AB's electron beam melting process. The outputs from the simulation data could be used to better understand the local melting, grain evolution, composition and internal stresses within freeform-fabricated metal parts.

© Copyright 2009 by Tushar Ramkrishna Mahale

All Rights Reserved

Electron Beam Melting of Advanced Materials and Structures

by
Tushar Ramkrishna Mahale

A dissertation submitted to the Graduate Faculty of
North Carolina State University
In partial fulfillment of the
Requirements for the degree of
Doctor of Philosophy

Industrial Engineering

Raleigh, North Carolina

2009

APPROVED BY:

Harvey West

Edward Grant

Denis Cormier
Co-Chair of Advisory Committee

Ola Harrysson
Chair of Advisory Committee

DEDICATION

This work is dedicated to my parents Mr. Ramkrishna Vishnu Mahale & Mrs. Veena Ramkrishna Mahale. Thanks for your patience folks!

Another person Tushar would specifically like to dedicate this work to is his niece.

Tushar's sister, Sonali, is expecting a baby around the end of October. It's a tight race!

BIOGRAPHY

Tushar Mahale was born on the 24th March, 1976, in Mumbai, India. He attended Hansaraj Morarji Public School, Mumbai, India; Indian Language School, Lagos, Nigeria; Bombay Cambridge School, Mumbai, India for his primary and secondary schooling. He attended Parle College (now Sathaye College) for his pre-university education. During his Junior year of college, Tushar developed an interest in exploring Personal Fabrication technology using Rapid Prototyping. After graduating with a Bachelor of Engineering in Production Engineering, from the University of Pune in 1997, Tushar joined the Rapid Prototyping Cell of the Indian Institute of Technology-Bombay (IIT B) in August 1997 as a Senior Research Engineer . In January 2000, Tushar moved to North Carolina State University, Raleigh, NC; to pursue a Master's Degree in Industrial Engineering. He graduated in 2003 after having conducted preliminary research on the development of a Three Dimensional Electrophotographic Printing Process. After completion of his Master's degree, Tushar continued at NC State University to pursue a PhD Industrial & Systems Engineering. The focus of his research has been on the development of new materials with applications in both aerospace and medical industry using the electron beam melting process. Tushar plans to investigate research and products that could arise from the integration of manufacturing, biology and computing. Tushar believes that a flattened world requires communities to rely more on innovation and entrepreneurship than ever before. He would like to introduce the general

community to personal fabrication methods as tools for innovation, science, technology
& education.

ACKNOWLEDGMENTS

For their guidance and support, Tushar would like to thanks Dr.Denis Cormier, Dr.Ola Harrysson, Dr.Harvey West, Dr.Edward Grant and Mr.Jason Low

For their patience, support and trust, Tushar would like to thank my parents Mr. Ramkrishna Mahale & Mrs. Veena Mahale, my sister Mrs.Sonali Sohani and the rest of the super extended family

For their inspiration and help, Tushar would like to thank a great group of friends including Cohan Carlos, Parikshit Kulkarni, Kent Meiswinkel, Dr.Ketan Bhatt, Dr. Rajeev Prabhakar, Ron Aman, Kyle Knowlson, Alderson Neira, Bela Bapat; the list goes on.

For lessons on taking a break from work while dangling on rocks, Tushar would like to thank Dr.Hartmut Wege, Hua-Ying Ling, Monica Cu, David Kaplan Tim Ehlich, Lisa Yuan

For a home away from home, Tushar would like to thank the local coffee shops, Global Village, Cup-a-Joe, Helios, Café Driade

For their awesome company in my experiments with food, Tushar would like to thank Monica Cu, Dhanashree Mayenkar, Lisa Yuan, Tim Ehlich, Dr.Olivier Cayre, Dr. Hartmut Wege and Dr.Susan Lai-Yuen

For making this research possible, I would like to thank the wonderful folks at Arcam

AB

TABLE OF CONTENTS

LIST OF TABLES.....	xi
LIST OF FIGURES	xiii
Chapter 1 Introduction	1
1.1 Background.....	1
1.2 Rapid Prototyping.....	2
1.2.1 Laminate Based Metal RP Systems.....	2
1.2.2 Binder Based Processes	4
1.2.3 Direct Metal Melting Processes.....	8
1.3 ARCAM Electron Beam Melting (EBM) Process.....	11
1.3.1 ARCAM S12 Hardware.....	11
1.3.2 System Calibration.....	14
1.3.3 ARCAM S12 Control Software and Process Parameters.....	16
1.4 Conclusion.....	18

Chapter 2	Electron Beam Melting of GRCo-84.....	20
2.1	Introduction	20
2.2	Literature Review	22
2.3	Electron Beam Manufacturing of GRCo-84.....	23
2.4	Results	30
2.4.1	Chemical Composition of EBM GRCo-84 Samples	30
2.4.2	Mechanical Properties of EBM GRCo-84 Samples	31
2.5	GRCo-84 Conclusions.....	35
Chapter 3	Electron Beam Melting of γ -Titanium Aluminide.....	37
3.1	Introduction	37
3.2	Background.....	39
3.2.1	Literature Review	39
3.2.2	Previous Research at North Carolina State University.....	45
3.3	EBM Based Combustion Synthesis of Titanium Aluminide.....	49
Chapter 4	Electron Beam Melting of Aluminum 2024.....	55

4.1	Fabricating Al-2024 on the EBM S12	61
4.2	Non-Stochastic Al-2024 Foams.....	80
4.3	Conclusion	83
Chapter 5 Electron Beam Melting of Metamaterials.....		84
5.1	Introduction	84
5.2	CAD Issues	87
5.3	Metal Foams	89
5.4	Manufacture of Non-Stochastic Metal Meshes on the EBM.....	92
5.4.1	Mechanical Testing of Non-Stochastic Foams.....	94
5.4.2	Cryogenic Testing of EBM Manufactured Non-stochastic Foams.....	103
5.5	Conclusion	118
Chapter 6 Other Materials Developed using the Arcam EBM System.....		121
6.1.1	Copper	122
6.1.2	7075 and 6061 Aluminum Alloys	124
6.1.3	Lunar Regolith Simulant.....	137

Chapter 7	Modeling the Electron Beam Melting Process	144
7.1	Understanding Electron Beam Layered Manufacturing	147
7.1.1	Causes of “Smoke”	148
7.1.2	Melting cycles.....	154
7.2	Simulation.....	165
7.2.1	Finite Elements Method.....	165
7.2.2	Finite Difference Method	172
Chapter 8	Conclusion	182
References	189

LIST OF TABLES

Table 2-1	Properties of GRCop-84.....	21
Table 2-2	ICP Elemental Analysis of Alloying Elements for GRCop-84.....	31
Table 3-1	Selected material properties for TiAl and nickel superalloys [43].....	38
Table 3-2	ICP elemental analysis results (NSL and NCSU Combined Results).....	48
Table 3-3	ICP results of chamber-deposited metallic film.....	49
Table 4-1	Properties of aluminum alloy 2024.....	56
Table 4-2	Initial Al-2024 EBM test observations.....	63
Table 4-3	Small Sample Build Observations for Al-2024.....	65
Table 4-4	Processing conditions for Al-2024 test specimens.....	69
Table 4-5	Density and porosity in Al-2024 specimens	71
Table 4-6	UTS comparison of as-processed and aged Al-2024 specimens.....	78
Table 5-1	Summary of lattice compression test results.....	99
Table 5-2	Dimensions of samples for conductivity tests.....	107
Table 5-3	Top Temperature for each sample.....	110
Table 5-4	Observations on the effect of radiant heat.....	117
Table 6-1	Key physical properties of pure titanium, aluminum & copper.....	122
Table 6-2	ICP analysis of EBM processed samples of Aluminum alloy 7075	126
Table 6-3	Summary of EDS results for “Black” 7075 aluminum alloy powder	128
Table 6-4	EDS Analysis of sample from the hood.....	130

Table 6-5	EDS results of reused 7075 alloy powder	130
Table 6-6	EDS analysis on the “Blobs” formed during the melting of 7075 alloy	132
Table 6-7	Composition of JSC-1 lunar regolith simulant.....	138
Table 7-1	Electrical and physical properties of EBM materials.....	159

LIST OF FIGURES

Figure 1-1	Laminated metal transformer cores	3
Figure 1-2	Conventional 3D printing process	5
Figure 1-3	Fused Deposition Modeling (FDM)	6
Figure 1-4	Selective Laser Sintering (SLS).....	7
Figure 1-5	Droplet based net-form fabrication.....	9
Figure 1-6	Schematic diagram of the Arcam S12 system (Drawing not to scale)	13
Figure 1-7	Scanning parameters for the EBM process.....	17
Figure 2-1	GRCop-84 powder with Cr ₂ Nb particles dispersed in a copper matrix.....	22
Figure 2-2	GRCop-84 hourglass samples fabricated via EBM	25
Figure 2-3	Micrographs of EBM-processed GRCop-84	25
Figure 2-4	Heating strategies for influencing microstructure of GRCop-84.....	26
Figure 2-5	Current and Speed Vs. Part Height for Various Speed Functions and Layer Thicknesses.....	29
Figure 2-6	Graph of 0.2% offset yield stress for GRCop-84.....	32
Figure 2-7	Elongation at UTS versus temperature for GRCop-84.....	33
Figure 2-8	UTS as a function of temperature for GRCop-84.....	34
Figure 2-9	Low Cycle Fatigue (LCF) test results for GRCop-84.....	34
Figure 3-1	Typical γ -TiAl processing methods[43]	40
Figure 3-2	Selective reaction synthesis via printing of molten Al droplets [45].....	45

Figure 3-3	Ti6Al4V turbocharger compressor wheel fabricated via EBM	46
Figure 3-4	Illustration of balling in TiAl sample	47
Figure 3-5	Successful EBM TiAl test specimen.....	47
Figure 3-6	Initial results of reaction synthesis of TiAl via EBM	52
Figure 3-7	XRD plot for selectively reaction synthesized titanium aluminide	53
Figure 4-1	Configuration for initial feasibility testing of Al2024	62
Figure 4-2	Configuration for small sample tests of Al 2024	64
Figure 4-3	Surface roughness of initial Al-2024 specimens	66
Figure 4-4	ASTM E-8 tensile test specimen dimensions in millimeters	67
Figure 4-5	Effect of scan length on Al-alloy 2024's surface finish	68
Figure 4-6	Photographs of Al-2024 Test Specimens.....	70
Figure 4-7	Sample I-I with UTS of approximately 21.25 MPa.....	72
Figure 4-8	Sample I-II with UTS of approximately 11.25 MPa.....	73
Figure 4-9	Sample II-I with UTS of approximately 10MPa.....	73
Figure 4-10	Sample II-II with UTS of approximately 325MPa and elongation of 1.57%	74
Figure 4-11	Sample I-I Aged, UTS approximately 42.5MPa.....	76
Figure 4-12	Sample I-II aged, UTS of approximately 187.5MPa	76
Figure 4-13	Sample II-I aged, UTS of 11.5MPa	77
Figure 4-14	Sampled II-II aged, UTS of 225MPa.....	77
Figure 4-15	Turbochargers fabricated in Al-2024 via the EBM process	80

Figure 4-16	Aluminum Mesh Load Vs. Displacement Test Results	82
Figure 5-1	Negative refractive index materials developed using a C-ring resonator	85
Figure 5-2	An ordered structure similar to a 3D photonic crystal.....	85
Figure 5-3	Examples of stochastic and non-stochastic foams	86
Figure 5-4	Grid generated using Hyperfun.....	88
Figure 5-5	Discrete constrained stochastic mesh structure.....	89
Figure 5-6	Stochastic copper foam	91
Figure 5-7	Top, front, and dimetric views of hexagonal lattice structures.....	94
Figure 5-8	Influence of beam angle, beam thickness, and layer thickness on bonding between layers	95
Figure 5-9	Range of strut qualities	95
Figure 5-10	Lattice compression test orientation convention.....	97
Figure 5-11	Compression test results for 4mm structures with maximum loading up to 1300 lbs	97
Figure 5-12	Compression test results for 5mm structures with maximum loading of up to 550 lbs	98
Figure 5-13	Lattice compression test results for 6mm structures.....	98
Figure 5-14	Compressive strength and elastic modulus versus relative structure density	101
Figure 5-15	Lattice structure flex test setup	102
Figure 5-16	Load displacement plots for 4-mm structures.....	102

Figure 5-17	Micrographs of EBM fabricated lattice beams (a) 100x, (b) 200x	107
Figure 5-18	Test samples (a) Sample 1 (b) Sample 2 (c) Sample 4	108
Figure 5-19	Setup of the experiment with sample 1 mounted to aluminum blocks and cryocooler.....	110
Figure 5-20	Bottom block temperature vs. applied power	111
Figure 5-21	Conductivity Vs. Temperature for Ti6Al4V alloy.....	112
Figure 5-22	Temperature profiles from CosmosWorks (a) Sample2 (b) Sample 3	113
Figure 5-23	Heat flux results from CosmosWork	114
Figure 5-24	Scanning Electron Micrographs of lattice structure reveal particles sintered to the lattice structures; this increases the effective surface area of the part.	116
Figure 5-25	Total power Vs. Temperature with approximate curve fitting	117
Figure 5-26	Negative Poisson's Ratio Materials Built On the EBM	120
Figure 6-1	EBM processed pure copper	123
Figure 6-2	Cracks in EBM processed 7075 a) Micrograph taken parallel to the E-beam scan direction b) Micrograph taken perpendicular to the E-beam scan direction c) top-view of the sample	125
Figure 6-3	SEM image of “Black” 7075 aluminum alloy powder	128
Figure 6-4	A closer look at a “Black” 7075 powder particle	129
Figure 6-5	Aluminum alloy 7075 vapors deposited on the system hood	129
Figure 6-6	Reused 7075 alloy powder.....	130

Figure 6-7	“Blobs” formed during the melting of 7075 alloy powder	131
Figure 6-8	SEM images of E-Beam scans on a 7075 aluminum plate	133
Figure 6-9	Comparison’s between Mechanically Alloyed Powder & Pre-alloyed Powder of 7075 a) Mechanically Alloyed b) Prealloyed	135
Figure 6-10	Optical micrograph of EBM processed 6061 with Fe-Al intermetallic....	137
Figure 6-11	Ball milled aluminum regolith mixture with 20% aluminum loading.....	139
Figure 6-12	Sintering of a single layer of pure aluminum via low current heating.....	140
Figure 6-13	EBM processed JSC-1 lunar regolith simulant with 50% aluminum melted at 60KV acceleration voltage a) Top surface of EBM processed part b) Close up revealing regolith embedded in aluminum matrix	141
Figure 6-14	100% JSC-1 Lunar regolith stimulant fixture sintered using the EBM process.....	142
Figure 7-1	Electron beam interaction with substrate.....	146
Figure 7-2	Type I particle charging	149
Figure 7-3	Type II particle charging.....	153
Figure 7-4	Monte Carlo simulations of beam & substrate interactions[119]	155
Figure 7-5	Influence of powder density on charging	158
Figure 7-6	Angle of incidence of an electron beam	161
Figure 7-7	Relationship between backscattering and angle of the incident electron beam on aluminum substrate.....	162

Figure 7-8	Relationship between backscattering coefficient and the angle of incidence of an electron beam.....	163
Figure 7-9	Interaction between spherical powder used in EBM processing and the electron beam.....	164
Figure 7-10	Simulation of the initial heating of a Start plate embedded in a bed of Aluminum Powder	166
Figure 7-11	Arcam AB's model for electron beam melting.....	167
Figure 7-12	Variable density mesh generated along the circular path	168
Figure 7-13	Beam scan path over a region meshed to uniform density	170
Figure 7-14	Simulation of e-beam scanned over 7075 powder carried out in COMSOL [®] by breaking down the part into voxels to facilitate the tracing of the beam.	171
Figure 7-15	High speed electron beam scan paths during sintering.....	173
Figure 7-16	A discretized slice file (SLC).....	175
Figure 7-17	Profile of an electron beam scanning over homogenous low thermal conductivity material. Effect of radiant heat loss has been ignored	177
Figure 7-18	Approximating level of sintering.....	179
Figure 7-19	Selective resolution for large data sets.....	181
Figure 8-1	Visible light emitted by preheated powder bed when a) loose b) sintered	184
Figure 8-2	Massively parallel algorithms using Matlab [®] parallel computation toolbox	187

Figure 8-3 Electron beam scanned a) without b) with a spin 188

Chapter 1 Introduction

1.1 Background

In 2003, North Carolina State University (NC State) acquired the first, Arcam EBM S12 machine in North America. This gave NC State the opportunity to be integrally involved in process development and optimization from its early stages. In subsequent years, the team has initiated or been directly involved in several new material research projects for the EBM.

During experiments related to new material development, the failure of a build experiment meant repeating the experiment from the beginning and the loss of time due to part cool down and machine clean up. Secondly, part failure is a discrete event; i.e., the means of measuring the extent of success or failure of the part built, and any corrective action needed was based completely on the operator's subjective experience and "reflex action".

The experience gained from both successes and failures makes a compelling case for research into developing a strategy for material development for the EBM process. In this document, data from experiments related to the EBM system are presented, and suggestions for future research are made for developing a strategy for new material development strategies.

1.2 Rapid Prototyping

In the early 1990s, freeform fabrication of metals became a focus for a large portion of the additive manufacturing research community. One of the main applications that researchers desired was the development of production tools via near net fabrication. With these tools available to them, researchers would reduce build lead-time and reduce cost building and reworking tools.

The trends in the development of metal-based Rapid Prototyping (RP) systems took three different routes as listed below:

- Laminate based metal RP systems
- Binder based processes
- Direct metal melting processes

1.2.1 Laminate Based Metal RP Systems

Laminate based RP systems involve two separate processes: (1) the cutting of 2D laminates and (2) the stacking and joining of the cut sections. This technology was popularized within the RP community by a manufacturer named Helisys, that marketed the technology specifically for pattern makers from the casting industry.

Unknowingly, laminate-based layered manufacturing has for long been used in the manufacturing of metal components for many years. One of the prime examples would

be cores of transformers that are made by joining metal laminates. What distinguishes the old laminates based manufacturing with rapid prototyping systems is the automation and integration of the cutting and joining steps[1].

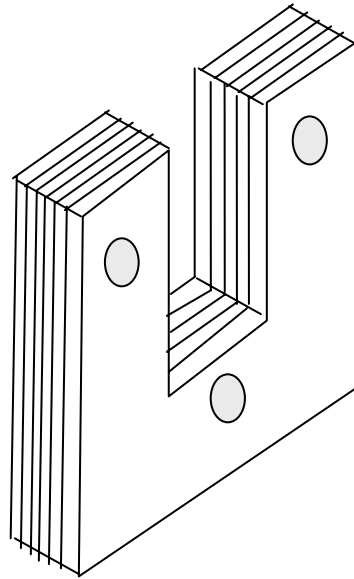


Figure 1-1 Laminated metal transformer cores

Numerous researchers throughout the 1990s experimented with developing a laminate based layered manufacturing systems to make production tools[2, 3]. What distinguished these new systems from the old laminate based manufacturing was the automation and integration of the cutting and joining processes.

Himmer et al [3] developed a system that cut the laminates using a CO₂ laser. The cut sheets were joined either by welding, adhesives, or simply by means of screws or other anchors. The built parts were post processed with a laser or 3-axis milling machine to

remove any built up edges and to finish the part to the desired surface finish requirements.

Kong et al [4, 5] developed a process called Ultrasonic Consolidation for ultrasonically fusing precut sheets of metal using ultrasonic welding.

The obvious limitation of laminate based component manufacture is its limited ability to produce overhanging regions and the anisotropic strength characteristics exhibited by the parts built by this method.

1.2.2 Binder Based Processes

After the commercial acceptance of the polymer and ceramic-based RP systems, researchers experimented with adapting the existing process technology for manufacturing metal parts.

The 3D Printing research group at Massachusetts Institute of Technology initiated research on converting the 3D Printing process to print metal parts [6-8]. An organic binder was used to selectively bind metal powder on the build plane of the 3D printing system. The loosely bound powder metal parts (green parts) produced by this system were sintered in a furnace to form either sintered or fully dense metal parts. Any voids that existed near the surface of the part were infiltrated with bronze. This system was later commercialized by a company named Prometal. Shivpuri et al [9] have

demonstrated the use of this technology for producing dies for forging Al-7075 components.

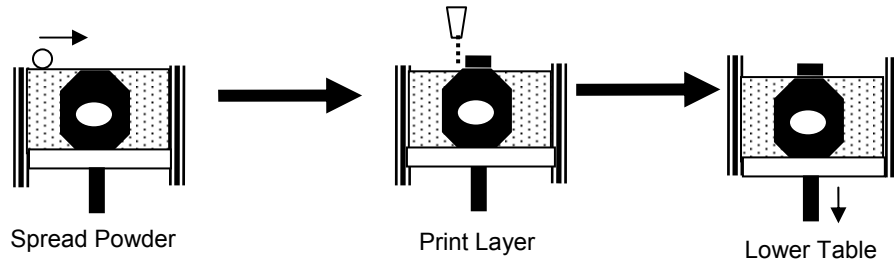


Figure 1-2 Conventional 3D printing process

Fused Deposition Modeling (FDM), a commercial system, continuously extrudes and lays down a thermoplastic filament from a base stock of the same thermoplastic wire but with a larger diameter. The process was adapted to deposit green metal and ceramic parts by compounding the metal or ceramic powder with a thermoplastic binder and then extruding it to form the base stock wires that would be accepted into the FDM system [10, 11]. Dense metal or ceramic parts were obtained via sintering and infiltration of the green parts in a furnace.

Greulich et al [12] have come up with an adaptation of the FDM system that uses powder rather than wires to directly make dense metal parts. Dense metal parts are limited to low melting point alloys and the use of a binder-based system was suggested for alloys with a higher melting point.

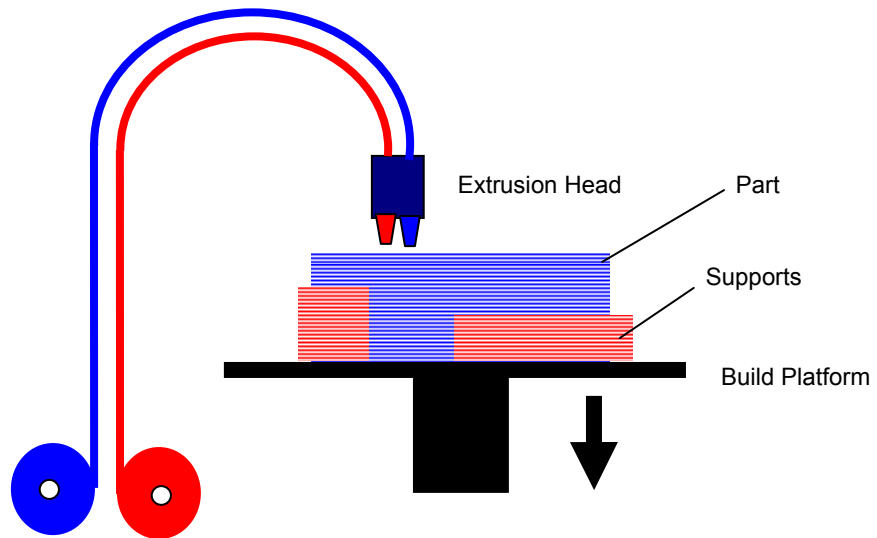


Figure 1-3 Fused Deposition Modeling (FDM)

The selective laser sintering (SLS) process was developed at the University of Texas at Austin and was later commercialized by DTM Corp. The early models of the system used low power lasers (10W-20W) to selectively sinter a variety of thermoplastic polymers.

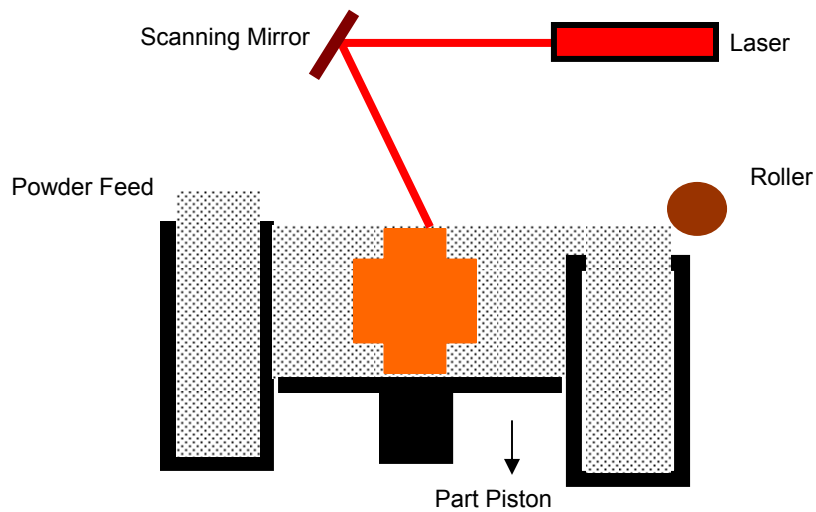


Figure 1-4 Selective Laser Sintering (SLS)

Research in the field of adapting this process for manufacturing tooling inserts started with the use of polymer coated (polyamide) metal powder [13, 14]. The nylon on the powder acted like a binder when it was melted by a laser to form a green part. The green part was then passed through the standard processes of binder burn out, sintering and infiltration to form tool inserts.

Later process improvements upgraded the laser to anywhere between a 70W-1000W to directly achieve sintering of the metal powders. The new build themes varied from manufacturing parts with dense skins and sintered insides to making fully dense parts. Some processes used a two-phase powder system consisting of one low melting point and one high melting point metal. Similar to the polymer binder; the low melting point metal acted like a binder for making a green part of the high melting point metal [14-21].

Eoplex Technologies Inc. has developed a process called High Volume Print Forming (HVPF) capable of making heterogeneous parts in metals, ceramics and polymers [22, 23]. The process builds parts via screen-printing layers of engineered inks. The ink consists of metal or polymer particles suspended in a photopolymer. It is possible to selectively print inks of different materials within a single layer. The layers are assembled to form a green part followed by burn out and sintering operations to generate the finished item. High print resolution and capabilities to manufacture across a large range of materials in a single part makes this process attractive. The limitations are the very large size of the machine and the need for a high volume production.

1.2.3 Direct Metal Melting Processes

A number of researchers have experimented with droplet printing of metals [24-29]. Methods for generating the molten metal droplets vary between using a piezoelectric crystal to apply a bias on the nozzle to eject a drop onto the substrate [26-29] or applying pulses of inert gas at a high pressure to the reservoir of metal sitting behind the nozzle [24, 25, 30]. The rapid solidification of the droplet on contact with the substrate leads to fine grain sizes. This is particularly desirable for aluminum alloys where toughness is desirable. One of the biggest hurdles in the wide acceptance of this method is due to its feasibility with only the low melt metals.

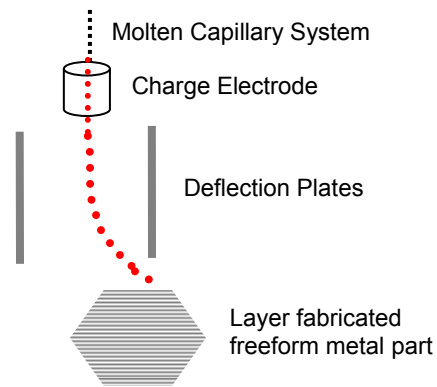


Figure 1-5 Droplet based net-form fabrication

A combination of additive and subtractive fabrication called Shape Deposition Manufacturing (SDM) was developed at Carnegie Mellon University [31, 32]. The process progresses in the following steps:

- Deposition of material using an appropriate welding method
- 5-axis CNC machining of the slice using first order shape approximation for the slice
- Shot peening for stress relief

The process was adapted for manufacture of heterogeneous materials as well as making meso-scale dense metal parts. One of the challenges with this process is the possibility of tool gouging into the previous layer while 5-axis machining of surfaces at an acute angle to the X-Y plane. The current research of this group focuses on adapting the technology for making fuel cells and tissue scaffolds. A number of variants of this process have been developed at various research groups.

Laser melting has been one of the most widely used techniques for direct freeform fabrication of dense metal parts. The direct adaptation of the commercial selective laser sintering processes (liquid phase sintering) is one example of laser based processing of metals.

The direct fabrication of a part in a bed powder poses three problems

- The powder in the immediate neighborhood of the melted region sinters and melts to the part causing an uneven surface finish (this is also seen in the Electron Beam Melting process)
- The presence of loose powder around the melt region makes it difficult to model the melting process as the radiated heat loss from the powder becomes a parameter of uncertainty.
- The melting of metal requires an inert atmosphere around it to prevent contamination or oxidation of the powder. This is done by: (1) A localized shroud of inert gas around the melt pool, or (2) having the entire build envelope in an inert atmosphere. The jet of inert gas being delivered at the metal laser interface blows away the powder from the bed.

To avoid the above mentioned problems, some researchers [33-35] have developed processes where the raw material is specifically delivered to the point of interaction between the metal and the laser. The raw material (generally powder) is delivered from the side into the melt pool generated by the laser or it is delivered co-axially to the laser.

1.3 ARCAM Electron Beam Melting (EBM) Process

Arcam's S12 EBM system[36] is the first commercial electron beam based layered manufacturing system designed for producing dense freeform metal parts. The important aspects of the hardware and process variables that could have a significant effect on the processing of parts are briefly described here. The hardware and software configurations described in this document are the earliest configurations for the Arcam AB's S12 system. The machine continuously goes through hardware and software upgrades as part of the maintenance contract.

1.3.1 ARCAM S12 Hardware

The system can be broken down into the following hardware components:

Build Chamber

The fabrication of the part actually happens in the build chamber. The chamber also houses almost all the mechanical components of the system including the build tank, powder feeders and raking systems.

Build Tank

Build tank is literally a steel tank with a platform in the XY plane capable of moving along the Z-axis. The part is fabricated over a start plate that is preheated prior to the start of the build. The current build tank is capable to building parts 250mm x 250mm x 250mm (we have built parts of a maximum size of approx. 200mm in the XY plane).

Powder Feeder & Raking system

The powder is stored inside two hoppers located in the top left and right corners of the build chamber. The raking system picks up a calibrated dose from the two hoppers and spreads a thin uniform layer over the bed of powder in the build tank (refer Figure 1-6). The rakes that carry out the powder spreading are disposable and are made out of thin sheets of spring steel.

Control System

The control system consists of a computer, programmable logic controller, signal amplifier and a set of DC power supplies.

High Voltage Power Supply

The high voltage power supply located at the bottom of the control cabinet. It provides power to the following components (refer Figure 1-6):

- Heating the filament
- Grid cup-filament bias voltage
- Acceleration voltage for the electrons

Vacuum System

The company recommends operational vacuum for the electron gun between 10^{-7} and 10^{-6} mBar. The build chamber is held between 10^{-3} and 10^{-4} mBar. These vacuums are achieved using two turbo pumps aided by a backing pump

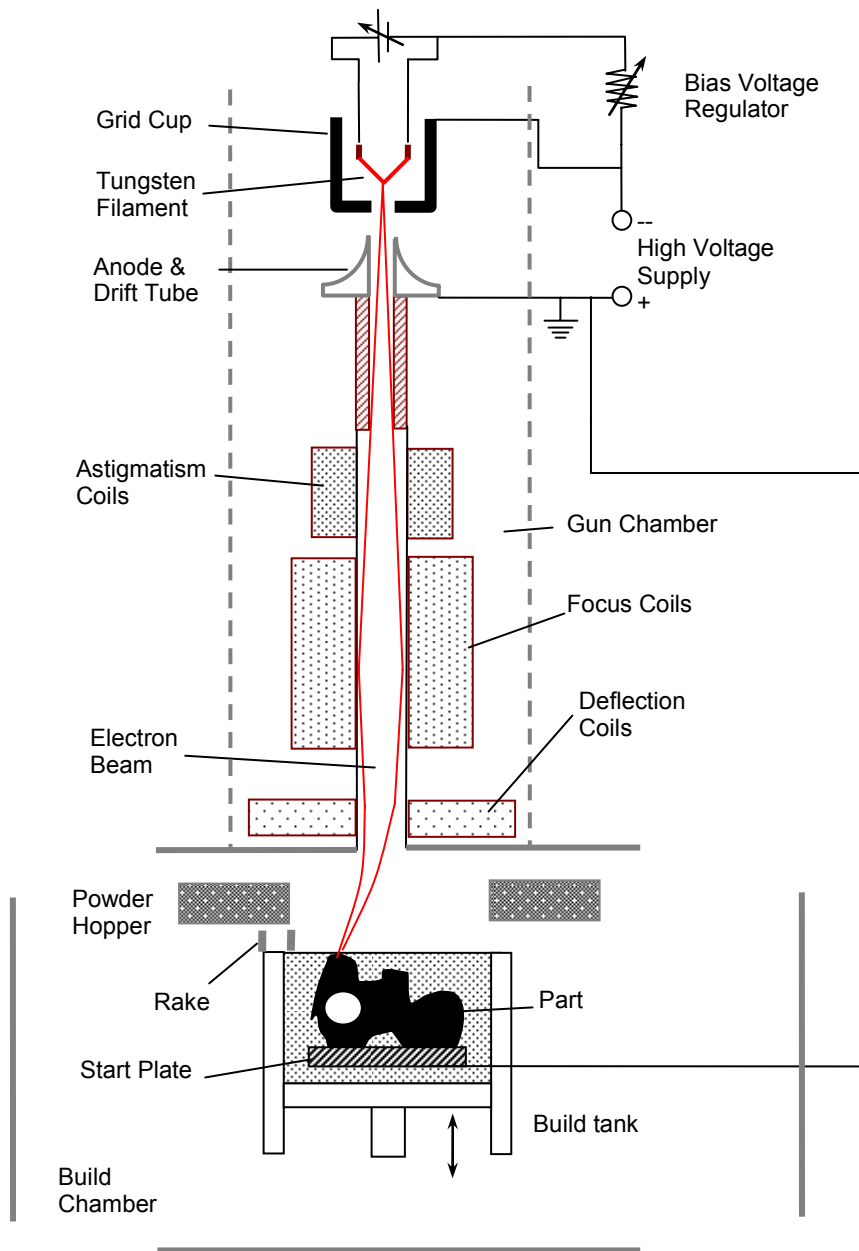


Figure 1-6 Schematic diagram of the Arcam S12 system (Drawing not to scale)

Electron Beam Column

The electron beam column consists of a cathode assembly, a drift tube-anode assembly, focus coils, astigmatism coils and deflection coils.

The cathode assembly consists of a tungsten filament based cathode and a grid cup. The tungsten filament is electrically heated to the point where the tip of the filament is white hot. A potential difference between filament and the anode, accelerates electrons from the filament towards the anode. The electrons that are not absorbed by the anode pass through the drift tube and eventually interact with the part.

A negative bias on the grid cup with respect to the filament controls the amount of electrons that finally reach the anode (and eventually the processed part).

The cross sectional geometry of the beam is controlled by the focus coils and the astigmatism coils. The position of the beam over the surface of the part in the build plane is controlled by a set of deflection coils [36].

1.3.2 System Calibration

The accuracy and reliability of the part produced by the system is to a large extent based on the soundness of the calibration. The system calibration consists of two components.

Rake Calibration

A calibrated rake accurately controls the amount of powder that is being dispensed from the powder feeders into the build plane. When too little powder is dispensed it leads to an uneven distribution or lack of powder across the build plane. An excess of dispensed powder leads to shortage of powder in the later layers of the build. Another consequence of excess dispensing is the spillover of the powder from the rack back onto the build plane. This leads to the development of non-uniform layer thickness that can eventually lead to the development of “smoke” during the processing of that particular layer.

Beam Calibration

Beam calibration can further be divided into two parts: (1) The first involves calibration of beam position with respect to magnetic fields applied by the deflection coils. This is done by storing the position of the beam over an X-Y grid consisting of 49 points and (2) The focusing of the beam and correction of the astigmatism of the beam on each of the individual points on the X-Y grid. Interpolation is then used to calculate the position of the beam between the points. The main drawback of the beam calibration approach is that it leaves room for human error during calibration of the beam. It should be noted that deflection based beam control makes it possible to operate the beam over a very large range of scan speeds. This cannot be achieved with a conventional X-Y gantry.

1.3.3 ARCAM S12 Control Software and Process Parameters

Similar to conventional RP systems, Arcam's S12 systems use sliced data in the form of a file format called SLC. The SLC file defines the geometry of individual two dimensional cross-sections and the distance between two adjacent slices.

As stated earlier in section 1.3, the build process begins with the heating of a build plate of a compatible material to a suitable temperature. Once the plate is heated to a predetermined temperature, the system progresses with the building of the actual part.

Multiple SLC files can be run concurrently to define various processing conditions within a given build layer. The most important amongst these are themes (sets of process settings) for:

- Preheating and sintering the entire build region. This is for (1) minimizing thermal gradient and hence the internal stresses within the part and, (2) providing conductivity paths for the incident electrons before the beginning of a melt cycle.
- Sintering of powder in the regions located below overhangs. Higher sintering provides (1) additional mechanical support to overhanging sections and, (2) higher conductivity for the electrons from the electron beam to flow out of the powder bed.
- Melting of the powder defined by the actual part

For the sake of nomenclature, the first three of the files processed by the system have been allocated by the Arcam Control software as “Preheating files” or “phd files”. Up to two additional files are allocated as “Postheating files” or “pod files”. One file is meant specifically for defining the actual melting parameters. The precedence of executing the files for any given layer is preheating -> melting -> postheating.

Each of these files [37] contains contour and inner raster features. The contours are defined by the perimeter for that layer and up to five concentric offsets of the perimeter can be used. The inner raster patterns used to melt the bulk of the part look similar to that shown in the figure 1-7.

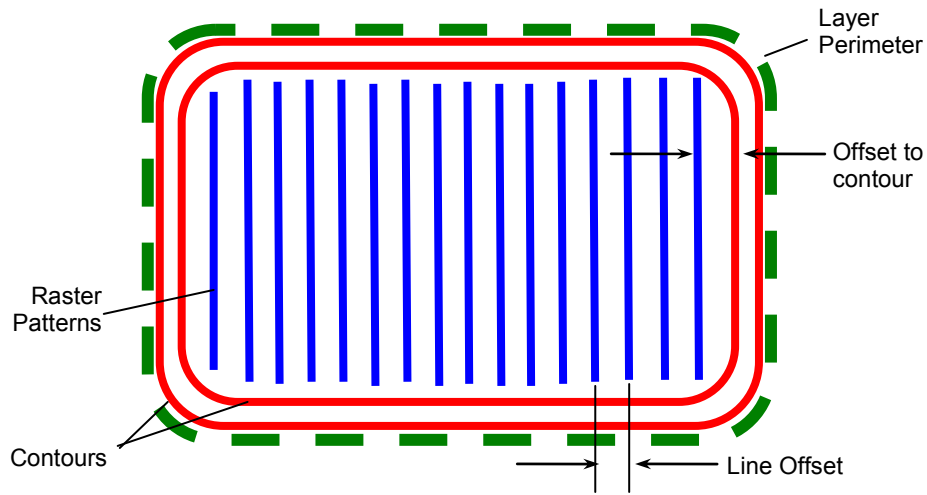


Figure 1-7 Scanning parameters for the EBM process

The process parameters of the preheat and postheat files can be defined manually. There are close to 25 parameters in each of the preheat and postheat files. The main parameters include:

- Minimum and maximum beam current, and the number of times the beam scan is to be repeated. The beam current is ramped linearly from the minimum to the maximum beam current during every scan
- Scanning speed of the electron beam
- Distance between individual scan lines (referred to as line offset)
- Line order for the hatch pattern.

This body of work shall examine the role these process parameters play in the development of new materials using Arcam AB's Electron Beam Melting System.

1.4 Conclusion

The Electron Beam Melting (EBM) process has distinct advantages over the existing methods used for fabricating fully dense metal parts

- The high vacuum atmosphere necessary to process a part using the EBM minimizes the possibility of part contamination due to any rogue gases within the build envelope.
- Laser based melting is mostly a surface phenomenon and the absorption of incident light by the processed material is dependent on the wavelength. This limits the variety of metals that can be processed on a laser based system. Unlike

a laser, an electron beam consists of electrons of finite mass that are moving at a high velocity and transfer their energy to the processed material through their impact with the material. The electrons travel deep into the material as they transfer their kinetic energy to other electrons within the material.

- The electron beam in Arcam's S12 EBM system is controlled by magnetic deflection coils. This reduces the number of moving parts in the EBM system while simultaneously permitting the electron beam scans to achieve speeds as high as 40,000 mm/s. The large scan speeds aid in increasing the build speeds while simultaneously opening the possibility of controlling the microstructure evolution within a part.

As described above, the electron beam melting process provides numerous advantages for the additive manufacturing of metals. Having said that, the large variety of scanning styles and selection of process parameters offers new challenges for processing materials and enhancing properties of the finished parts using the electron beam melting process. Chapters two through seven shall build upon lessons learned through development of process models whose objective is to contribute to a more structured approach to new material development using the electron beam melting process.

Chapter 2 Electron Beam Melting of GRCop-84

2.1 Introduction

Cu-8Cr-4Nb (GRCop-84) is a dispersion strengthened copper-based alloy developed by researchers at NASA's Glenn Research Center in the 1990's. The chromium and niobium exist in the form of intermetallic Cr₂Nb in a matrix of copper. The dispersion of small intermetallic particles (roughly 0.1-10μm) inhibits the grain growth in copper. At low temperatures, small grain boundaries act as barriers to dislocations, thus strengthening the material. The stability of Cr₂Nb particles at elevated temperature prevents the loss of strength of the alloy at high temperature. The Hall and Petch relationship explains the relationship of the grain size to part strength.

$$\sigma_y = \sigma_o + \frac{k_y}{\sqrt{d}}$$

where σ_y is the yield strength, σ_o is the frictionless stress resistance, k_y is the Hall-Petch slope; a constant and d is the grain diameter. This equation provides a means of accounting for the presence of grain boundaries and the randomization of crystal orientation in polycrystalline materials (macroscopically these variations manifest themselves as isotropic properties).

Table 2-1 Properties of GRCop-84

ALLOY COMPOSITION		PHYSICAL & MECHANICAL PROPERTIES	
<u>Component</u>	<u>At. %</u>		
		Yield Strength 150K	275MPa
		Yield Strength 1000K	40MPa
Cu	88%	UTS 150K	575MPa
Cr	8%	UTS 1000K	40MPa
Nb	4%	Elongation 150K	20%
		Elongation 1000K	20%
		Thermal conductivity 150K	270 W/mK
		Thermal conductivity 1000K	290 W/mK
		Electrical resistivity 150K	1.2 μΩ.cm
		Electrical resistivity 500K	3.5μΩ.cm

GRCop-84 was specifically designed for high heat flux operations where strength is retained over a very large thermal gradient. It is targeted for applications such as the Space Shuttle's main combustion chamber (MCC) liner. GRCop-84 is generally fabricated in powder form via gas atomization. The powder is then extruded into sheets, plates, or tubes by encapsulating powder in steel or copper cans that are removed after extrusion. It may also undergo hot isostatic pressing (HIP'ing) or forming over a substrate using a cold spraying technique. However, the alloy is not readily cast, as Cr₂Nb precipitates produced during the casting process can grow into the cm size range

[38]. It has excellent strength at extreme temperatures while maintaining good creep, low-cycle fatigue lives and low thermal expansion [39].

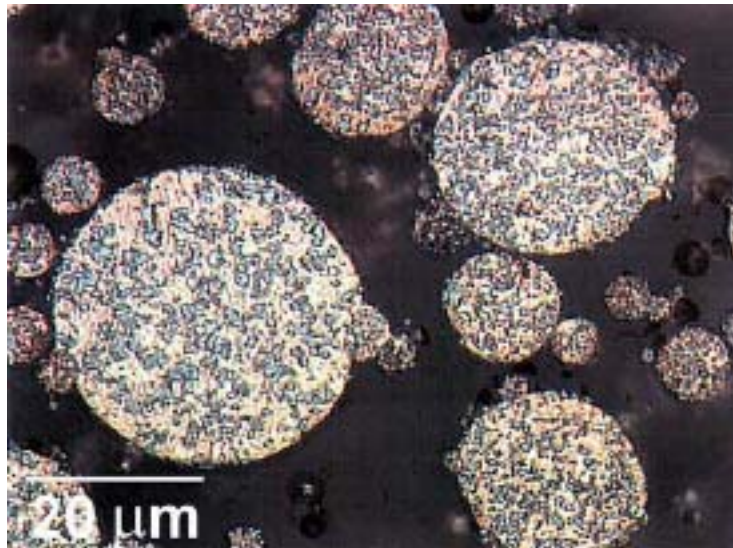


Figure 2-1 GRCop-84 powder with Cr₂Nb particles dispersed in a copper matrix

2.2 Literature Review

Studies on oxidation-reduction resistance [40, 41] of several copper-based alloys of interest for high temperature applications found that GRCop-84 had excellent static and cyclic oxidation resistance. This characteristic makes it an attractive material as a liner for rockets. Following 40-50 oxidation-reduction cycles, a protective Cr-Nb oxide film was observed on the GRCop-84 samples that provided excellent protection against blanching.

Ellis and Keller [39] studied the thermophysical properties of GRCop-84 in comparison with NARloy-Z (cu-3 wt.% Ag-0.5 wt.% Zr) which is currently used as the main combustion chamber liner material. The GRCop-84 had a much lower coefficient of thermal expansion. A lower CTE results in lower thermally induced stresses. Practically speaking, this translates into longer life for the liner. This is obviously desirable for a Reusable Launch Vehicle (RLV).

Ellis [38] provides a broad overview of the GRCop-84 material. In general, rapid solidification processes must be used with the material to prevent Cr₂Nb precipitates from growing in size during solidification. GRCop-84 is most commonly produced in powdered form via argon gas atomization. GRCop-84 has also been by vacuum plasma spraying onto mandrels [42].

2.3 Electron Beam Manufacturing of GRCop-84

The precipitation and agglomeration of Cr₂Nb in most conventional casting processes makes it almost impossible to make parts by any conventional casting process (particularly thick cross sections). The electron beam freeform fabrication process makes it possible to retain the small particle size of Cr₂Nb due to the very small size of the weld pool and its accelerated cooling due to the surrounding cooler powder; an ideal processing method.

Preliminary experiments intended to determine the feasibility of processing GRCop-84 with the EBM process provided the motivation for establishing a less ad-hoc procedure for new material development. A set of parameters called a build theme is suggested for all the materials commercially sold by Arcam. These themes automatically calculate the speed and current requirements for processing the part. The exact method by which these parameters are generated is not completely understood. The parameters that influence the automatic power calculation are the maximum current, the layer cross-sectional area and something called the “speed function” which has discrete values ranging from -10 to 200. The actual relation between this speed function and the speed and current used for processing has not been made available outside of Arcam, but the parameter seems to influence the scanning speed of the electron beam.

Tensile test coupons and samples resembling liners for rocket engines were built using a speed function value of 10, maximum current limit of 27mA, and a seed value for scanning speed of 1000mm/s (Figures 2-2 and 2-3). The properties of the samples produced on the EBM are discussed in the next section.



Figure 2-2 GRCop-84 hourglass samples fabricated via EBM

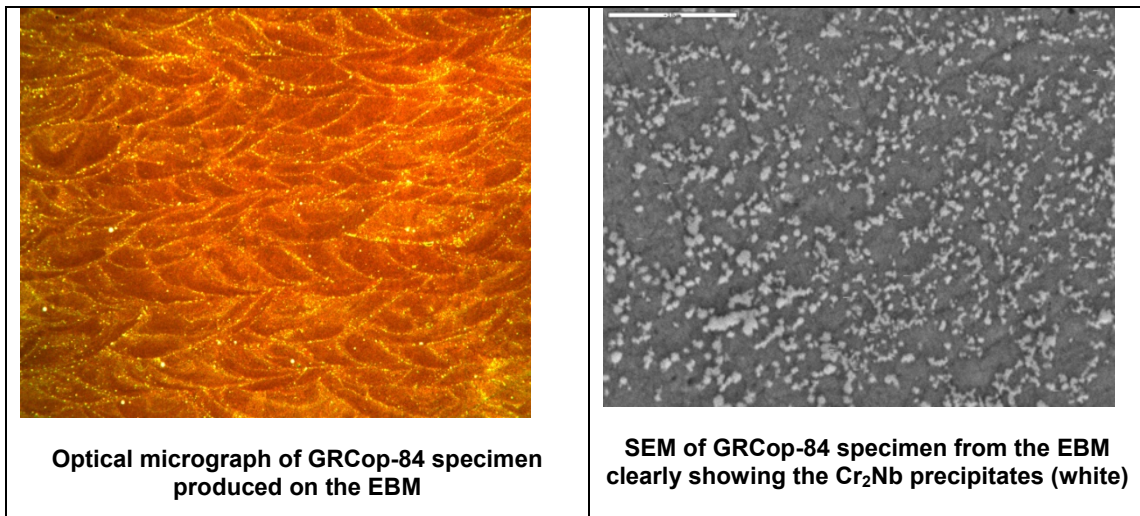


Figure 2-3 Micrographs of EBM-processed GRCop-84

Experiments were carried out to control the microstructure of the part by changing temperature gradients across the build plane (Figure 2-4). In the first experiment, a

smaller region within the melt area of the part was reheated immediately after the melting operation. It was observed that this led to coarser precipitates of Cr_2Nb .

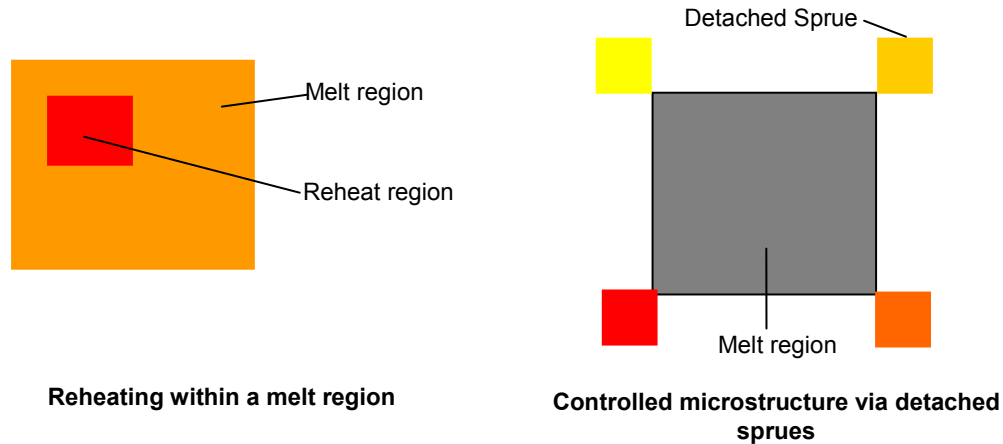


Figure 2-4 Heating strategies for influencing microstructure of GRCop-84

For the second experiment; four disconnected sprues of identical cross-sectional area were constructed around a relatively large cross-sectioned part that was being melted. Each of the sprue was melted prior to the melting of the part. This was carried out for every layer of the part. The amount of heating for each sprue was substantially different. It was expected that directional solidification or grain growth would be observed.

Unfortunately, only a couple of layers could be built before the surface quality of the part degenerated to the point where the part couldn't be salvaged. This was observed on many other builds that involved large cross-sections. For various reasons, the automatic power calculations did not produce satisfactory results with this material. The GRCop-84 powder's particle size distribution was between +325/-100 mesh (45-150 μm) but the

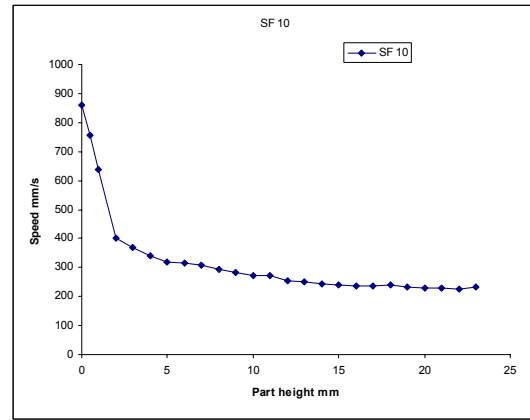
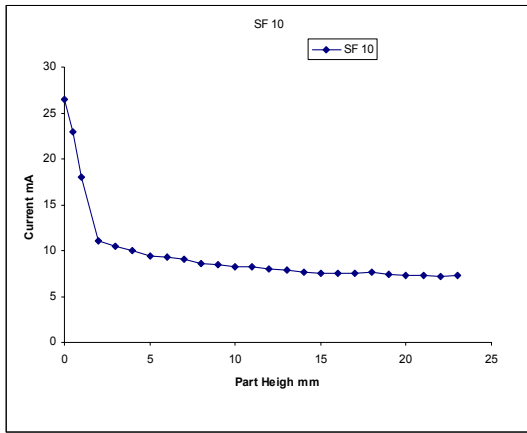
processing of the material lead to the generation of finer particles due to vaporization of the material. These finer particles lead to arc trips during the processing of the alloy and on advice from Arcam AB, the experiments with GRCop-84 were halted.

It was decided to carry out simulations using Arcam's EBM Control software to determine the processing parameters used by the system to melt a uniform cross-sectioned part of 30 mm square. Figure 2-5 shows various plots of current versus speed under different conditions. It was observed that the first few layers of a part are melted with very high currents and speed. This might be due to the fact that the control software uses the history of the previously melted layers while calculating the parameters for the next layer. Since the start plate is modeled into the part file, its mass might be considered to be a sort of a heat sink and hence the reason for high scan speeds and current. The stumbling block here is that key thermophysical properties such as thermal conductivity, melting point, and latent heat of fusion for the material are not considered by the control software.

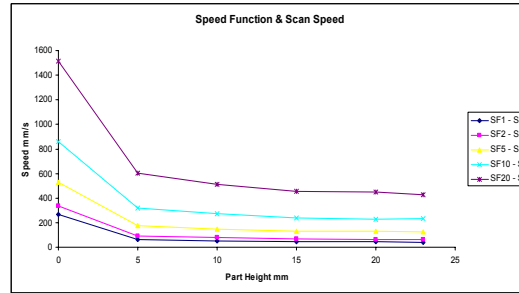
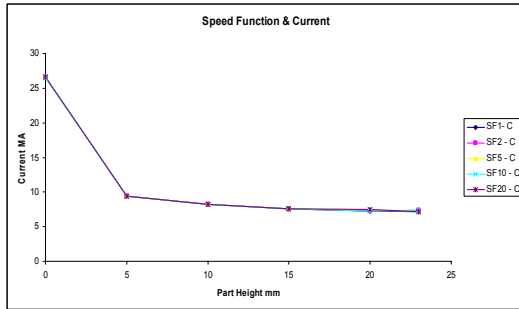
When the speed function was varied while maintaining the layer thickness of 0.1mm, it was observed that the beam current was maintained almost constant for all speed functions. The variation was in the scan speeds, and there seems to be some correlation between relative speed function and scan speed values. It was not possible to establish a distinct relationship between the actual speed function number and the scan speed. As

long as all other variables were equal, the scan speed increased when the speed function was increased.

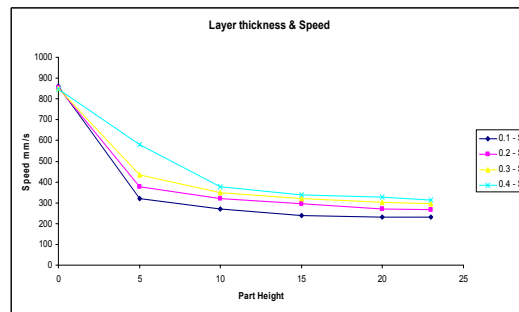
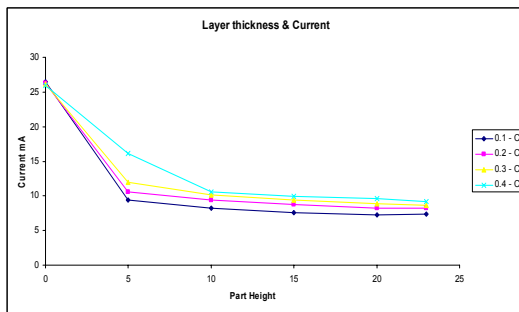
The next simulation involved experimenting with varied layer thicknesses for the same cross-section and speed function. Layer thickness variation of 0.1mm, 0.2mm, 0.3mm and 0.4mm were evaluated. No major variation between the power level and layer thickness was observed from the simulation. This indicates that the simulator does not account for the mass of material that is actually being melted; a serious flaw for any automatic power calculation. The variation that is observed in the processing parameters was due to the lagging effect of the software evaluating the previously melted layers.



(a) Current & Speed Vs. Part Height for constant Speed Function of 10 & layer thickness 0.1mm



(b) Current & Speed Vs. Part Height for Speed Function 1, 2, 5, 10, 20 & layer thickness 0.1mm



(c) Current & Speed Vs. Part Height for constant Speed Function of 10 & layer thickness 0.1, 0.2, 0.3, 0.4 mm

Figure 2-5 Current and Speed Vs. Part Height for Various Speed Functions and Layer Thicknesses

Based on these simulations; it was concluded that there was a need for developing a more robust methods for EBM process parameters that can handle new materials became evident.

2.4 Results

Several specimens produced on the EBM were sent to NASA for testing, and the results of these tests are presented below.

2.4.1 Chemical Composition of EBM GRCop-84 Samples

During the processing on the EBM, some part of the powder is lost due to vaporization and hence the final part might not have the same composition as that of the powder used for fabrication. Table 2-2 shows the results of ICP analysis for both the original Crucible Research powder and the EBM solidified specimens. GRCop-84 nominally contains 6.5 wt.% Cr and 5.8 wt.% Nb. As can be seen from the results, the original powder was slightly higher in Cr and Nb content than the nominal values. Very minimal vaporization of Cr and Nb alloying elements took place, and the resulting material was closer to the nominal values than the original powder. This suggests that solidification of the melt pool for the processing conditions used to make the samples resulted in sufficiently rapid solidification to prevent significant vaporization of alloying elements.

Table 2-2 ICP Elemental Analysis of Alloying Elements for GRCop-84

Weight %	Powder	Processed
Cu	87.23	87.55
Cr	6.78	6.55
Nb	6.00	5.90
Total	100.00	100.00

2.4.2 Mechanical Properties of EBM GRCop-84 Samples

It is known that billets of GRCop-84 can be produced via extrusion, and that billets can be machined to a desired shape. However, this processing route is extremely time consuming and costly due to material waste. The EBM process was studied here due to the fact that it is a relatively fast near net shape process. Experiments were carried out to compare as best as possible the material properties obtained during this EBM feasibility study with properties obtained with more conventional methods.

Figure 2-6 shows a comparison of 0.2% offset yield stress test results from the EBM study with prior experimental results from NASA with extruded GRCop-84. At cryogenic temperatures, the yield stress of EBM'd GRCop-84 is noticeably lower than that of extruded GRCop-84. However, at elevated temperatures, the EBM'd GRCop-84 specimens had comparable performance.

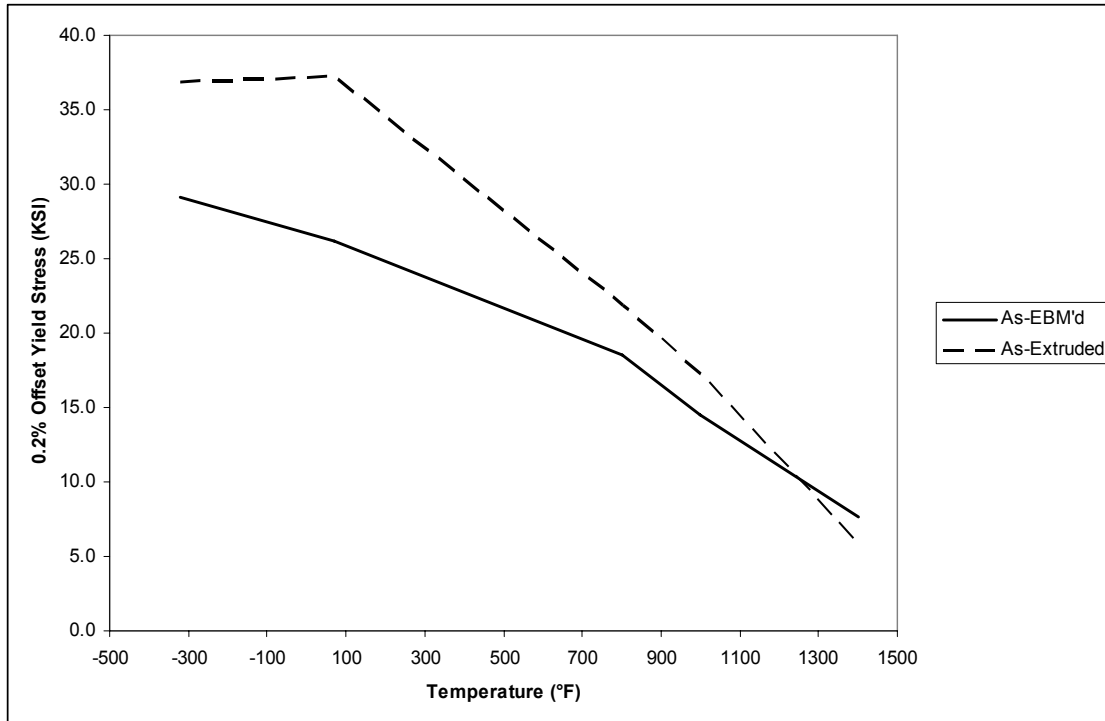


Figure 2-6 Graph of 0.2% offset yield stress for GRCop-84

Figure 2-7 shows a comparison of elongation test results from the present study with prior experimental results from NASA with both extruded and HIP'd GRCop-84. The extruded GRCop-84 showed relatively stable elongation across the full range of temperature values, whereas the HIP'd GRCop-84 showed a tendency to lose some elongation at elevated temperatures. In comparison, the EBM'd GRCop-84 had lower elongation at cryogenic temperatures, but vastly superior elongation at high temperatures.

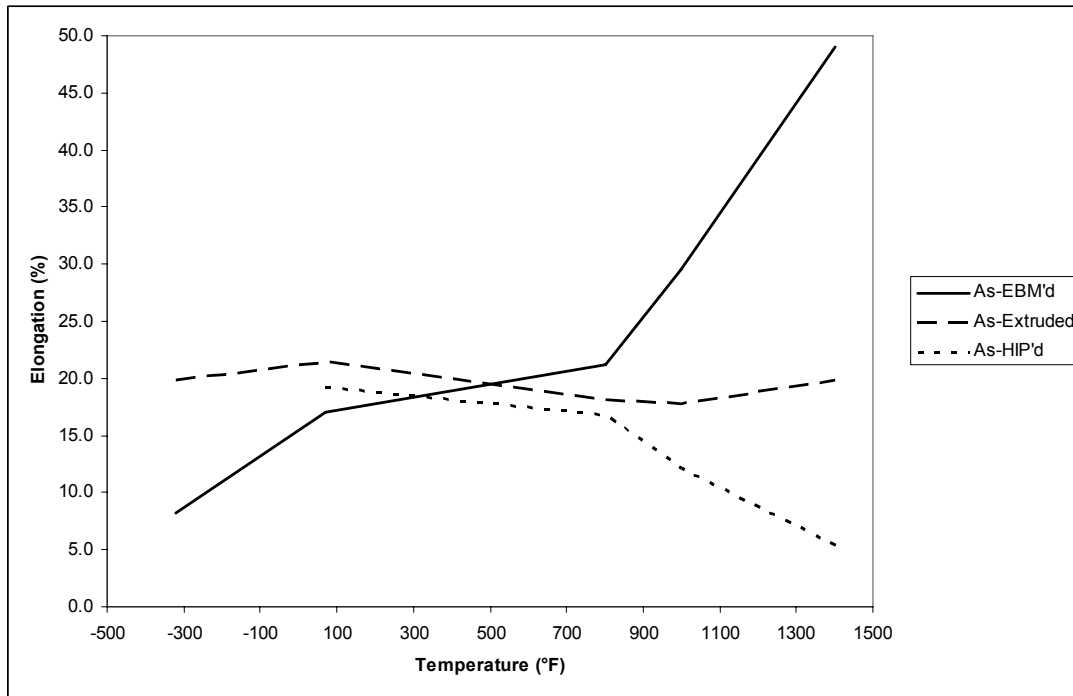


Figure 2-7 Elongation at UTS versus temperature for GRCop-84

Figure 2-8 compares ultimate tensile strength (UTS) of EBM, extruded, and HIP'd GRCop-84 from cryogenic to high temperatures. The UTS values were roughly comparable across the spectrum of temperatures.

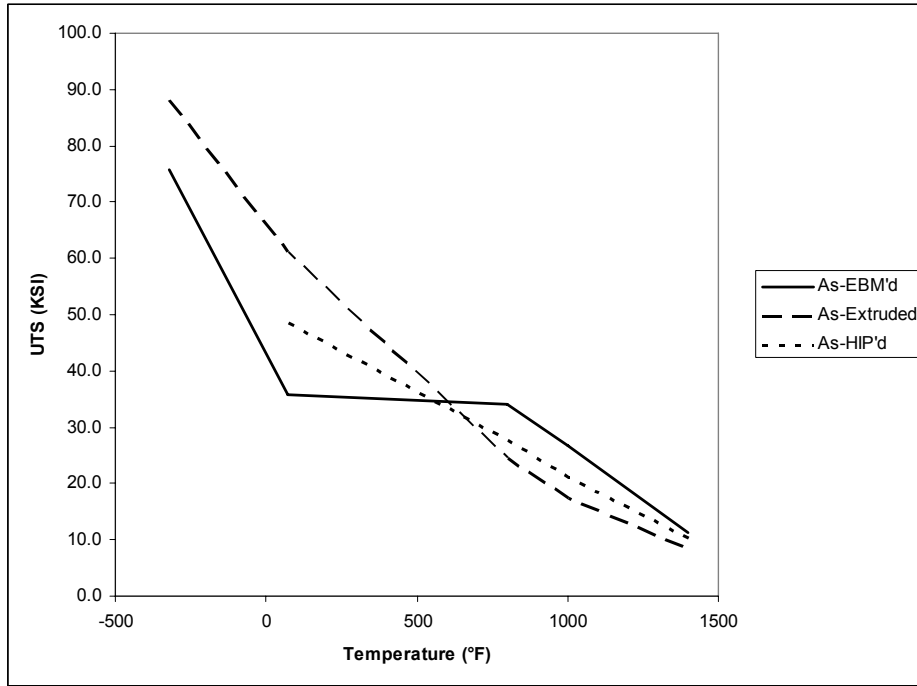


Figure 2-8 UTS as a function of temperature for GRCop-84

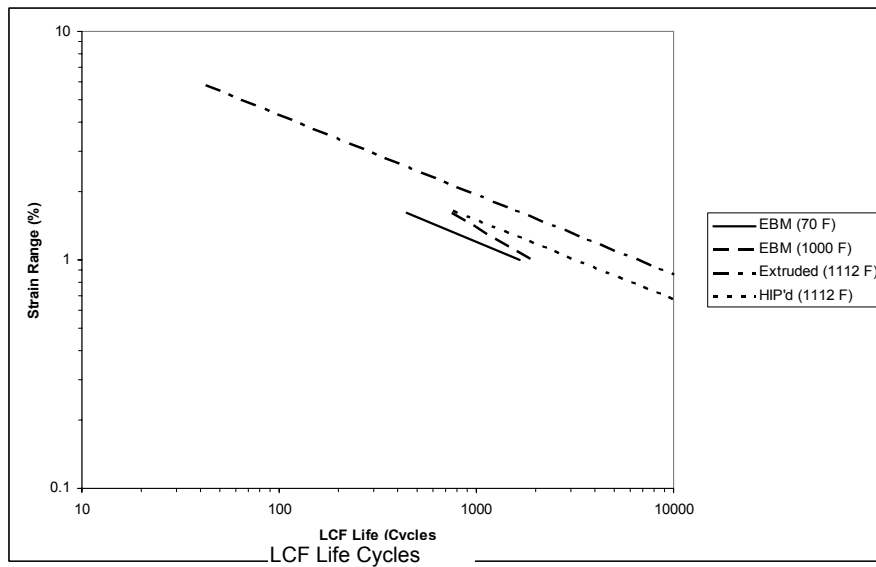


Figure 2-9 Low Cycle Fatigue (LCF) test results for GRCop-84

2.5 GRCop-84 Conclusions

This chapter has presented results from an initial feasibility study designed to assess the suitability of using the EBM process to produce complex near net shape GRCop-84 components. GRCop-84 is a relatively costly material that is difficult to cast into complex shapes, hence successful demonstration of an alternate processing route, like the EBM, would represent an important contribution.

Prior to this study, GRCop-84 had never been fabricated using the EBM process. It was therefore necessary to find a set of process parameters that will result in full densification and interlayer fusion. However, in this feasibility study, no attempt was made to iteratively modify process parameters so as to optimize material properties.

Optical and SEM microscopy confirmed that full densification and interlayer fusion were taking place with the given process settings. Furthermore, Cr₂Nb particulates were generally 1 μm or smaller, thus demonstrating that solidification was sufficiently rapid to prevent unwanted growth of Cr₂Nb particulates. Chemical analysis also confirmed minimal loss of alloying elements due to rapid solidification.

Mechanical test results generally indicated lower strength at cryogenic temperatures for EBM parts versus extruded or HIP'd parts. At elevated temperatures, however, mechanical properties of EBM specimens generally matched or exceeded those of extruded or HIP'd parts. As the GRCop-84 alloy was designed specifically with high

temperature applications in mind, it is therefore conceivable that the current process settings are suitable for high temperature applications without any need for further optimization. For cryogenic or room temperature applications, a formal process parameter optimization study would be recommended as the budget allowed.

In conclusion, this study has demonstrated that the EBM process can produce geometrically complex GRCop-84 components to near net shape. Further process optimization for low temperature applications is recommended. The present process settings produce excellent results at elevated temperatures.

The experiments with GRCop-84 utilized the speed functions based automated speed and velocity parameter generation. This method does not assure part quality when dealing with variation in part cross-sectional area. The exact relationship between a material's physical properties and the speed function is a trade secret of Arcam AB. Based on the data presented in figure 2.5, it can be concluded that a complete user driven control of the electron beam's scanning parameters would better serve new material development experiments. All future experiments in material development have been conducted by manually varying the speed and beam current parameters.

Chapter 3 Electron Beam Melting of γ -Titanium Aluminide

3.1 Introduction

Intermetallic compounds such as γ titanium aluminide and titanium niobide are gaining interest due to their exceptional material and mechanical properties at elevated temperatures. Gamma titanium aluminide has comparable properties to nickel based superalloys currently used in the aerospace industry but at half the density. There are many applications for intermetallic compounds including turbine blades, heat shields for reusable launch vehicles, heat shields for satellites, etc. These intermetallic compounds have low ductility at ambient temperature, which makes them difficult to machine and process using conventional methods. As can be seen in the table 3-1, the ductility for both γ -TiAl and Ni-superalloys are high at elevated temperature. However, processing at elevated temperatures increases the energy consumption, process complexity and the total cost of the parts.

Table 3-1 Selected material properties for TiAl and nickel superalloys [43]

Property	Conventional Ti Alloys	Ti₃Al	TiAl	Ni based superalloys
Density, g/cm ³	4.5	4.1-4.7	3.7-3.9	8.3
Modulus GPa	96-117	100-145	160-176	206
Yield Strength MPa	380-1150	700-990	400-650
Tensile Strength MPa	480-1200	800-1140	450-800
Creep Limit C	600	760	1000	1090
Oxidation Limit C	600	650	900	109
Ductility at RT, %	20	2-10	1-4	3-4
Ductility at HT, %	High	10-20	10-60	10-20

Combustion synthesis of mechanically alloyed elemental powder has been used successfully as an energy efficient method for producing intermetallic compounds of various compositions. Powder is packed in a mold and ignited, and an exothermic self-propagating reaction takes place until all powder has reacted. The complexity of the parts that can be made via this process is limited to the mold shape and packing capability. It is common to produce sheets of intermetallic compounds using combustion synthesis. The sheets can then be processed into the desired shape at high temperature.

3.2 Background

3.2.1 Literature Review

For the proposed study, a freeform fabrication approach to fabricating intermetallics via reaction synthesis will be developed. Intermetallics are ordered alloy phases formed between two metallic elements. The ordered structure results in enhanced strength, stiffness, creep resistance and oxidation resistance at elevated temperature. The intermetallics of titanium have the added benefit of exhibiting low density in comparison to nickel based superalloys, thus making them excellent candidates for aerospace applications [43-49].

The method of self-propagating high temperature combustion synthesis (also called reaction synthesis) was developed in Russia in the mid 1960s [44]. In a simple binary system, the reaction involves the diffusion of atoms of one element (generally in the liquid state) into the lattice of the other element. This leads to a release of energy which contributes to the self-propagation nature of the reaction. This class of reaction can be characterized by measuring the velocity of front propagation, maximum combustion temperature, extent of conversion of reagents, particle shape and size of the reagents and their proportions.

Conventional Processing of Intermetallics

Almost all conventional manufacturing processes for intermetallics minimize their dependence on shape manipulation via plastic deformation. Figure 3-1 briefly describes the methods used.

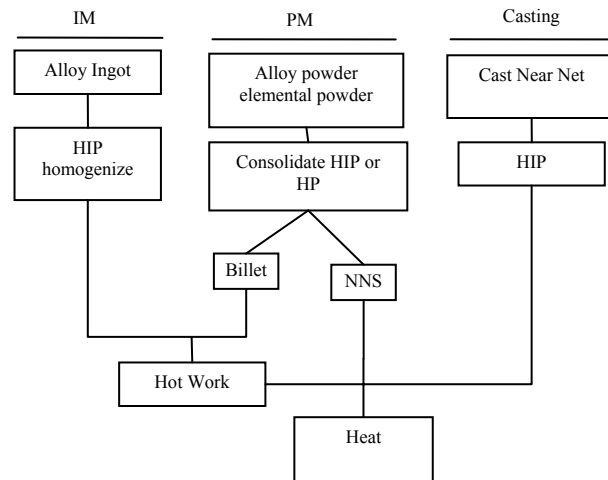


Figure 3-1 Typical γ -TiAl processing methods[43]

Weaver et al [50] have continuously cast thin strips of γ -TiAl. Researchers at Wright-Patterson AFB [51] have processed γ -TiAl through tape casting of γ -TiAl powder mixed with an organic binder. The green casts were later processed by hot isostatic pressing (HIP) to form dense tapes. The green tapes shrunk from 0.9mm thickness to 0.25mm after the HIP process.

Powder Metallurgy (PM) has been widely used for producing titanium aluminides. There are two methods for manufacturing parts via this route. The first involves conventional

powder metallurgy using compaction, sintering and HIP'ing of prealloyed intermetallic powders [52]. The other route involves the reaction synthesis of elemental powders. Rawers et al [53] used the powder metallurgy route to mildly compact (6.5 MPa) equi-atomic elemental powders of Ti & Al using a graphite die. The graphite die was heated to beyond the melting point of Al with simultaneous hot pressing to initiate the reaction synthesis of the TiAl. It was observed that the proportions of the resulting intermetallics (Ti3Al, TiAl) were a function of the hot pressing conditions (temperature, pressure, heating time).

Bertolino et al [54] studied the ignition mechanisms for Ti-Al and Ti-Ni powder systems by igniting compacts of elemental powders using a CO₂ laser. Proportions of the elemental powders were varied, and the phases of the reacted compacts were observed. They defined the ignition energy (E_{ig}) stored up to the ignition of the pellet as

$$E_{ig} = \int_{t=0}^{t_{ig}} \left[\alpha I_o - Q_{conv} - Q_{emiss} - \frac{\Delta H_{melt}}{\Delta t_{melt}} \right] dt$$

where

t_{ig} is the ignition time; I_o is the emitted laser power; Q_{conv} is the heat loss by free convection; Q_{emiss} is the radiant heat loss; ΔH_{melt} is the latent heat of fusion and Δt_{melt} is the melting time.

It was observed that the sample's absorptivity of the laser was very low, varying between 0.038 and 0.17. It was also observed that a reaction of an equi-atomic mixture of the elemental powders (A, B) did not necessarily generate a product of the type AB. The generation of the right type of products requires a fine control over the ignition time and the incident power. Similar laser based reaction initiation techniques have been used for other alloy systems [55].

One of the most common methods of making γ -TiAl components is through casting [56, 57]. In these studies, the casting was carried out using an induction skull melting furnace. All the cast specimens were HIP'd for 4 hrs at 1250°C to remove internal porosity [56]. Some specimens were further HIP'd between 1250°C and 1350°C for 24 hrs. It was observed that the constituent $\alpha_2 + \gamma$ and γ phases (α_2 phase is Ti_3Al) as well as the size and the nature of the microstructure varied based on the HIP cycle. It was also confirmed that there was a direct correlation between the nature of the structure and the fracture crack growth resistance. This is of particular importance for the casting process, as large thermal stresses are caused due to the variation in ductility of the intermetallics as a function of temperature [45]. Other than casting, isothermal forging of γ -TiAl ingots has been widely experimented with but has gained limited acceptance due to low ductility of lamellar TiAl that limits plastic deformation (hence conventional machining is also ruled out) [58].

Freeform Fabrication of Intermetallics

Freeform fabrication approaches to intermetallic production are based on either the melting of prealloyed intermetallic powders or the reaction synthesis of elemental powders.

Srivastava et al [59-62] have developed a laser-based freeform fabrication process called Direct Laser Fabrication (DLF) that uses a variable intensity CO₂ laser (300-450W) to selectively melt layers of Ti-48Al-2Mn-2Nb powders. It was observed that the grain structure varied between equiaxed and lamellar due to the combined effect of instant quenching caused by the localized melting and laser power. Since the lamellar structure is the most preferred of the grain structures, the samples were post-processed using hot isostatic pressing (HIP), and the effect of the length of the treatment and treatment temperature on the sample microstructure was studied. It was observed that a slow heat and a very low cooling rate led to good lamellar $\alpha_2+\gamma$ titanium aluminide.

Moll et al [63] experimented with Ti-47Al-2Cr-2Nb powder acquired from Crucible research that was selectively melted using a 14 kW CO₂ laser. As was the case with Srivastava's results, they observed that the parts made by this process required post-processing via HIP.

Carbide particle reinforced titanium aluminide matrix composites were developed by Liu and DuPont [64, 65]. Gas atomized Ti-48Al-2Cr-2Nb powder was mixed with 20% vol. TiC powder from Crucible Research and processed using a commercial Laser

Engineered Net Shaping (LENS) system by Optomec. It was observed that the components that were made using this system contained needle-like or dendritic formations of Ti_2AlC in addition to the base constituents. The authors observed that the parts were susceptible to cracking due to large thermal gradients that the parts were subjected to. Preheating of the substrate was suggested by the authors to prevent cracking of the parts.

A group of researchers from Japan [24, 25, 66] has developed a method called Reactive Rapid Prototyping (RRP) for freeform fabrication of Ti-Al-Ni based intermetallics via controlled reaction synthesis. The system is based on printing of molten Al onto a bed of Ni or Ti powders using pulsed argon gas. The molten Al reacts with the Ti or Ni powder around it to form an intermetallic bead. The next drop of Al is laid such that it overlaps with the previously formed bead to create a homogenous part via micro joining. It was observed that the phases of the binary constituents varied across the bead based upon the extent of diffusion of molten Al into the Ni or Ti lattice. It was observed that controlling the temperature of the molten aluminum resulted in control over the phases of the reacted products. The diffusion process can also lead to pores called Kerkendall diffusion pores [67].

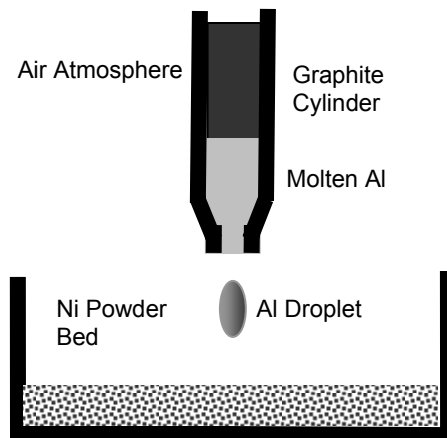


Figure 3-2 Selective reaction synthesis via printing of molten Al droplets [45]

A research group in Russia [68] has developed a selective laser induced sintering process for carrying out selective reaction synthesis of a variety of intermetallics. A YAG:Nd laser with power varying between 0.5 and 24W was used to initiate the reaction. This is orders of magnitudes lower than the power needed to process prealloyed γ -TiAl. It was observed that weakly exothermic reactions initiated locally and did not propagate through the rest of the solid.

3.2.2 Previous Research at North Carolina State University

A maker of heavy duty construction equipment contacted the EBM research group at North Carolina State University and expressed an interest in the use of EBM technology for making titanium aluminide components that would maintain good mechanical properties at elevated temperature.



Figure 3-3 Ti6Al4V turbocharger compressor wheel fabricated via EBM

From 2004-2005, industry sponsored TiAl research took place in the form of a multidisciplinary senior design project between the departments of Industrial Engineering and Materials Science and Engineering. The specific composition of γ -TiAl used in this study was Ti-47Al-2Cr-2Nb acquired from Crucible Research. The prealloyed γ -TiAl powder had a particle distribution of -100/+325 mesh (e.g. 45 – 150 μm), which required a minimum layer thickness of 150 μm . When developing the EBM process parameters for a new material, a large number of experiments are required to find adequate scanning and power parameters. By preheating the powder using high scan speeds and low beam currents, the powder was lightly sintered and the conductivity increased, thus reducing the risk of accumulated surface charge on the powder. Other process parameters such as the number of preheating scans, beam current and beam offset can dramatically affect how the powder behaves. Excess beam power can lead to vaporization of alloying elements, and it can lead to surface charging of the particles that causes them to repel one another. During initial tests, balling of the melt pool in the first few layers was a considerable problem. Figures 3-4 illustrate the phenomenon of balling

that took place for a wide range of process parameters. Figure 3-5 shows a successfully fabricated TiAl test specimens.

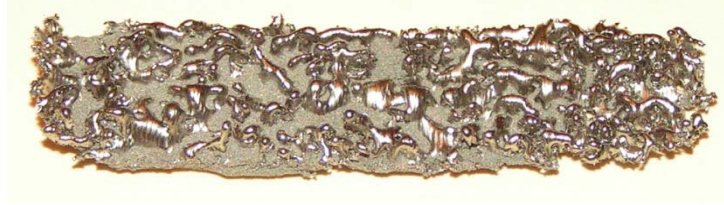


Figure 3-4 Illustration of balling in TiAl sample

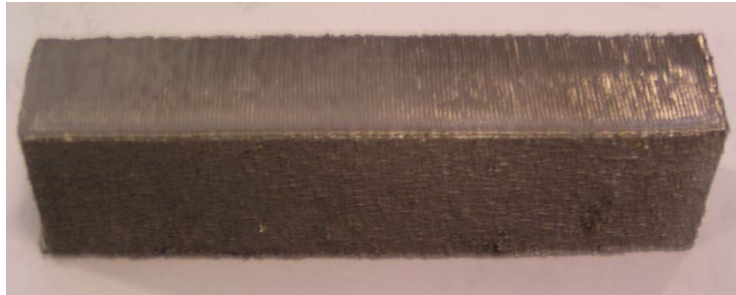


Figure 3-5 Successful EBM TiAl test specimen

Inductively coupled plasma (ICP) was used to determine elements present in both the initial TiAl powder and completed TiAl test bars. The raw powder supplied by Crucible Research was evaluated by NSL Analytical Services, Inc. Nine samples were also analyzed at NC State University using ICP. These consisted of three EBM processed TiAl specimens, three samples of a chamber-deposited film that was left on the Arcam EBM machine chamber wall and three samples of the raw powder that was processed in the EBM.

Table 3-2 summarizes the results of all ICP analyses' done. The data indicates that approximately 7.5% of the aluminum vaporized during processing for the processing conditions used to make these bars. The loss of 7.5% Al on the Ti-Al binary phase diagram would lead to a decrease in the amount of γ -TiAl. It is further noted that approximately 0.5% Cr was lost.

Table 3-2 ICP elemental analysis results (NSL and NCSU Combined Results)

Element	Initial Powder		EBM Part	
	Weight%	Atomic%	Weight%	Atomic%
Ti	62.50	49.99	65.68	57.03
Al	32.70	46.43	25.18	38.83
Nb	5.01	2.06	5.08	2.27
Cr	2.73	2.00	2.28	1.82
Fe	0.03	0.02	0.05	0.04

During EBM processing, a metal shroud is located above the build area to protect mechanical elements inside the chamber. The bulk of any vaporized metals deposit on the inner surface of this shroud. A piece of deposited film was peeled away from the shroud and submitted for ICP analysis. Results of that test are shown in table 3-3 below. As expected, the vapor deposits consisted of relatively large amounts of aluminum and

chromium – the elements whose concentrations were shown to have been decreased the most in the EBM bars.

Table 3-3 ICP results of chamber-deposited metallic film

Element	Weight%	Atomic%
Ti	8.98	5.51
Al	83.80	91.28
Cr	5.68	3.21

It was concluded that the low electrical conductivity of the pre-alloyed γ -TiAl caused most of the problems [69]. The long preheating cycle required to prevent charging of the particles and the high melting temperature caused significant vaporization of the Al leading to less than optimal material properties. It was observed that the conductivity of the γ -TiAl powder decreased over time as well, making it even harder to process. This could possibly be due to oxidation of the powder. Electron beam scanning patterns that could assist dielectric breakdown is one approach to overcoming this problem. Similar methods had been tried for spark sintering of titanium aluminides [70].

3.3 EBM Based Combustion Synthesis of Titanium Aluminide

In 2005, the research group at NC State University was introduced to a research group at SIMTech in Singapore that has been working on combustion synthesis of mechanically

alloyed elemental powders. The SIMTech group has produced γ -TiAl by compacting mechanically alloyed titanium and aluminum powders in molds and heating to 660°C. The reaction is initiated as the aluminum reaches its melting point [67, 71]. The group at SIMTech was looking for ways of processing the γ -TiAl in a more controlled fashion with greater geometric flexibility. It was suggested that an electron beam could be used to induce the reaction synthesis, and SIMTech supplied two types of powders to the research group at NC State University for evaluation. The energy required for carrying out such reaction would be orders of magnitude lower than that used for melting prealloyed powders as shown by Shishkovsky [68].

The two SIMTech powders consisted of equiatomic mixtures of elemental titanium and aluminum powders. The first powder was ball milled to mechanically alloy the two powders. The second powder was merely mixed. Initial feasibility experiments were conducted to test the hypothesis that it was possible to use the energy from the electron beam to induce a contained reaction synthesis.

During electron beam processing, the build chamber and the electron beam gun are under vacuum. The gun is normally at 1×10^{-6} mbars, and the build chamber is at 1×10^{-4} mbars. A pocket measuring approx. 20 mm x 50 mm and 0.5 mm deep was created in a 100 x 100 x 15 mm stainless steel plate using an Electrical Discharge Machine (EDM). The ball milled powder was spread in the pocket without compaction, the steel plate was placed in the build chamber, and the system was evacuated. The first experiments were

intended to investigate whether or not the uncompacted powder would ignite if the steel plate was heated to 660°C. The electron beam was scanned over the half of the plate that was not covered with powder in order to slowly raise the temperature of the plate and powder. The beam current was successively increased until a thermocouple attached to the underside of the steel plate read 800°C. No visible reaction of the powder took place at this temperature. In the next experiment, the pocket in the steel plate was filled with powder, and the powder was directly preheated using high scan speeds and a slowly increasing beam power. This was carried out until the reaction was visually identified by a sudden bright glow. A thin layer of titanium-aluminide had formed through reaction synthesis, but there was unreacted powder under the layer of reacted powder (see Figures 3-6c and 3-6d).

The beam diameter is typically focused to approximately 100 μm , and the melt pool created during normal operation is approximately 1.2 mm. The beam offset (space between two scan lines) is normally set to 1.2 mm. The electron beam has a Gaussian power distribution, and from the first successful experiment it could be seen that the powder had reacted along the scan lines with very lightly sintered powder between the strands (Figure 3-6a). This discovery indicated that there was in fact a controlled reaction synthesis taking place with minimal self propagation. By decreasing the beam offset in the next experiment, a more uniform sheet of titanium-aluminide could be fabricated.



(a) Reaction synthesis of titanium aluminide with scan lines 1 mm apart (notice lightly sintered powder between strands)



(b) Reaction synthesis selectively induced in the top-center portion of the start plate



(c) Distinct edge formation at the boundary of reacted and unreacted powder confirming controlled reaction synthesis



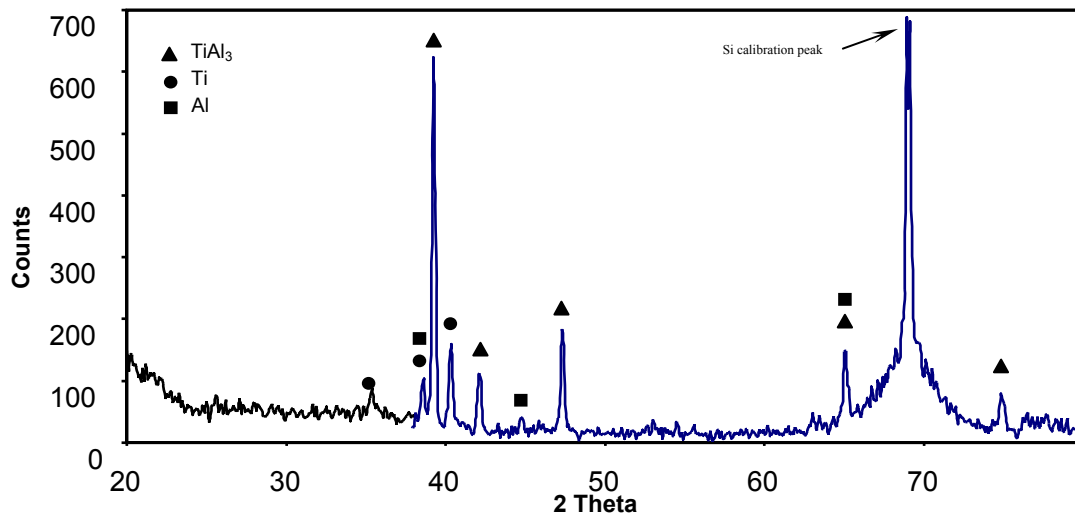
(d) Reaction propagation perpendicular to the surface of the powder

Figure 3-6 Initial results of reaction synthesis of TiAl via EBM

To further investigate the nature of the controlled reaction, an experiment was conducted where only a small region of the powder was scanned with the electron beam. A thin sheet of titanium-aluminide was created again, but only where the beam had scanned. The blended powder reacted as well, but the reaction was less complete. A new experiment was conducted where the ball milled powder was compacted in the pocket

using a 5 ton hydraulic press and a die matching the pocket. This time the reaction was still controlled but propagated throughout the thickness of the powder.

X-Ray Diffraction (XRD) was used to establish the phases of the uncompacted titanium-aluminide obtained from the reaction synthesis. As can be seen from the XRD plot below, there are still small traces of unreacted titanium and aluminum most likely due to loose powder from the bottom of the sample or due to unreacted powder between beam scan lines.



(Sincere thanks to Prof.J.Kasichainula for help with generating XRD plots)

Figure 3-7 XRD plot for selectively reaction synthesized titanium aluminide

There is a clear peak of $TiAl_3$ at 39.4, but other than that, there is no conclusive evidence of predominantly γ - $TiAl$ or other phases of titanium-aluminide. This happens for two reasons. First, there is an abundance of liquid Al when the reaction occurs thus making it

easier for the formation of TiAl_3 . Second, the free energy for the formation of TiAl_3 is lower than that required for the formation of TiAl or Ti_3Al [72, 73]. It is apparent that more detailed research is required to fully understand the controlled reaction synthesis and what needs to be done to achieve the desired $\gamma\text{-TiAl}$.

Chapter 4 Electron Beam Melting of Aluminum 2024

In the past few decades, there is a steady trend of replacing ferrous alloys with aluminum alloys. The main advantages of aluminum alloys are their reasonable strength to weight ratios and their low melting points, which makes them more energy efficient to process. This material also possesses other desirable qualities such as high conductivity, ductility, machinability and toughness. Aluminum alloys also easy to recycle due to their low melting points. Their recycling also requires far less energy than that required for extraction of aluminum from ore. The development of better aluminum casting alloys has resulted in almost a complete migration to aluminum engine blocks in the passenger car markets.

The research related to layered manufacturing of aluminum has largely been supported by the aerospace industry. The components used in this industry can be classified as low volume-high reliability, many a times the demand being as low as a single unit. The other, more futuristic project pursued by the aerospace industry is the deployment of LM systems during space missions for on demand fabrication.

Table 4-1 Properties of aluminum alloy 2024

ALLOY COMPOSITION		PHYSICAL & MECHANICAL PROPERTIES (T-6 tempering)	
<u>Component</u>	<u>Wt. %</u>		
		Density	2.78g/cc
		Tensile Strength, Ultimate	427MPa
Al	90.7-94.7	Tensile Strength, Yield	345MPa
Cr	Max. 0.1	Elongation at break	5%
Cu	3.8-4.9	Modulus of elasticity	72.4GPa
Fe	Max. 0.5	Electrical resistivity	4.49e-006 ohm-cm
Mg	1.2-1.8	CTE, linear 250°C	24.7µm/m-°C
Mn	0.3-0.9	Specific heat capacity	0.875 J/g-°C
Si	Max. 0.5	Thermal Conductivity	151W/m-K
Ti	Max. 0.15	Melting Point	502-638°C
Zn	Max. 0.25	Solidus	502°C
Other	Max. 0.05	Liquidus	638°C

Most of the metal processing LM systems should be capable of building aluminum parts. The literature that is being covered here specifically looks into literature dealing with freeform fabrication of aluminum parts.

Orme et al [27-29] have developed a process called “Precision droplet based net form manufacturing” and have worked extensively with using this technology for the manufacture of pure aluminum and Al-2024 components. The process uses piezocrystals

and electric fields to achieve depositions rates of approximately 0.83 Kg/hr. Fine grain sizes were observed in the parts produced via this process. This was due to rapid cooling of the droplet on the substrate. It was also observed that the grain size varied as the build progressed due to the accumulation of heat in the part. Strong correlation between substrate, orifice temperature and the grain size has also been observed. The authors have not reported the exact composition of the parts made via this process but it is assumed that the 14.9 psi inert gas pressure used for operating the system would reduce the vaporization of any alloying elements. The parts produced via this process had ultimate tensile strength (UTS) up to 30% higher than that of components produced by conventional processes.

The research group of Y. Miyamoto at Osaka University has reported a reaction synthesis-based RP process [24, 25, 66] using an approach they called Reactive Rapid Prototyping (RRR). An adaptation of the process called Net Droplet-based Manufacturing (NDM) has been used for the direct freeform fabrication of aluminum components [74]. This process uses pulsed high-pressure gas for the generation of droplets. This system generates fairly large droplets (200-500 μ m dia.) at a low frequency (1-5Hz). The authors observed that the solidified droplets were not completely joined together. This could be due to the semi-solid state of the droplets when they splat onto the substrate. Details of the effects of process parameters on microstructure and part strength have not been provided.

Kong et al [4] have demonstrated the use of a process called ultrasonic consolidation (UC) for freeform fabrication of parts made from 6061 aluminum alloy. Their system consisted of a modified 3.3KW seam welding apparatus operating at 20KHz. 100 μ m foils of aluminum 6061-T0 alloy were used for this study. These sheets were either “prepared” to remove any contaminants from their surface or they were used as is (unprepared). The effect of oscillating amplitude, contact pressure and welding speed on the quality of the welds was studied. The strength of the part was measured as a function of the resistance of the laminates to be peeled apart. It was observed in the welded unprepared sheets that the metal oxides tend to migrate near the weld joint, resulting in an oxide layer about 0.5 μ m thick. Though the amount of oxide at the weld interface was reduced when prepared, distinct unbonded regions could be observed at the weld interface.

The feasibility of a tungsten gas welding based process for the freeform fabrication of 5356-aluminum has been demonstrated by Ouyang et al [75]. The group has explored the idea of preheating the substrate to reduce the surface distortions in the part caused due to the high coefficient of thermal expansion. Surface preheating is also used to increase the wet ability of the welded layer. Since this process is based on melting a feed wire, the width of the weld pool is between 3.5-6.5mm and the height is between 0.25-0.55mm. The grain morphology is defined by the size of the weld pool and the location on the inspected region on the part. Defects in the form of hydrogen porosity and solidification cracks were observed. These can be due to rapid solidification across a relatively large volume.

Many researchers have also experimented with an electron beam based melting for the production of dense aluminum parts. JE Matz [76], KMB Taminger et al [77] and JK Watson et al [78] fed a raw material wire into the melt pool generated by an electron beam. JE Matz's work does not make any specific reference to his group having worked on the development of the system for processing aluminum alloys. Taminger and Watson, both engineers at NASA, have developed a low energy (15KV) electron beam system, aimed at in-orbit fabrication. Their proposed system would have 4-axis capability once it is completed (current system has 3-axis capability). In a recent paper, they demonstrated their system's capability at manufacturing components out of aluminum 2219 alloy. Due to the limitations set by wire based melting systems, the weld pools were large; 5-10mm wide. The parts produced were subsequently heat treated to a T-62 temper. The deposition speed for this system varied between 400 mm/min to 800 mm/min while maintaining a constant wire feed rates. As expected, higher translation rate led to faster cooling and finer grain structure. Another experiment was carried out where the beam traverse speed was kept constant and the wire feed was varied between 3000 mm/min and 1500 mm/min. Similar to translation speed; higher wire feed rates lead to faster cooling as the energy is distributed into melting a larger amount of material, thus producing small equiaxed grain structure. The strength of parts built on this system seems to be comparable to 2219-O alloy but the surface finish of the part is dictated by the high weld pool width and height.

Ackelid [79] from Arcam AB has conducted preliminary experiments with processing Aluminum-6061 using the S12 EBM system. Swelling of the top surface and long vertical cracks were observed in the parts built on the EBM system. A large loss in the magnesium content was observed in the finished part due to high vacuum and melting temperature. Columnar grain structures oriented along the z-axis were observed and there is a possibility that vertical cracks might have propagated along the grain boundaries.

Many of the commercial metal LM based systems suggest sintering of polymer coated metal powder to form a green part (~50% density), followed by a polymer binder burnout operation to form a denser part. After this, the part can be further sintered to form a dense part. However, this can give rise to very unpredictable surface distortions in the part. An alternative to this is infiltration of the sintered skeleton formed after the polymer binder burnout and metal powder sintering. This method helps retain the dimensional stability of the part. Sercombe et al [80, 81] suggests improvements to the process chain for sintering and infiltration based manufacturing techniques. A resin bonded Al-6061 part was first formed using a selective laser sintering setup. The infiltration was carried out by covering the part with alumina and magnesium powder and heating it to 540°C in the presence of nitrogen. The magnesium prevents the formation of an oxide inside the porous part and the nitrogen reacts with the aluminum to form AlN. The temperature of the furnace is raised to 570°C. The rigidity of the AlN skin permits it to be infiltrated by an aluminum alloy with a narrow melting range (Al-Si binary system is preferred due to its low viscosity when molten). At 570°C, the infiltrant melts and is absorbed into the

porous part. The parts produced by this process can be considered to be comparable to investment cast parts of the same material. Souvignier et al [10] has experimented with developing a fused deposition modeling like process to make aluminum metal matrix composites. A PMMA based slurry loaded with aluminum alloy in combination with silicon carbide, carbon fiber and alumina powder is extruded through a syringe to form the base. A process similar to that described above was used to generate a dense part.

4.1 Fabricating Al-2024 on the EBM S12

The reaction synthesis of titanium aluminide is initiated only after the melting of the aluminum. The parameters developed during the EBM reaction synthesis of titanium aluminide served as a good starting point for developing parameters for the melting of Aluminum 2024.

The feasibility tests for the processing of aluminum were carried out by placing a layer of aluminum powder inside a cavity approximately 0.75mm deep in a steel plate (Figure 4-1). The experiments were cold started by directly scanning the cavity region at 10,000mm/s 100 times as the current was ramped from 0.5-3.5 mA that was covered through 100 repeats. The first experiment itself showed evidence of sintering with light balling occurring at the surface of the powder.

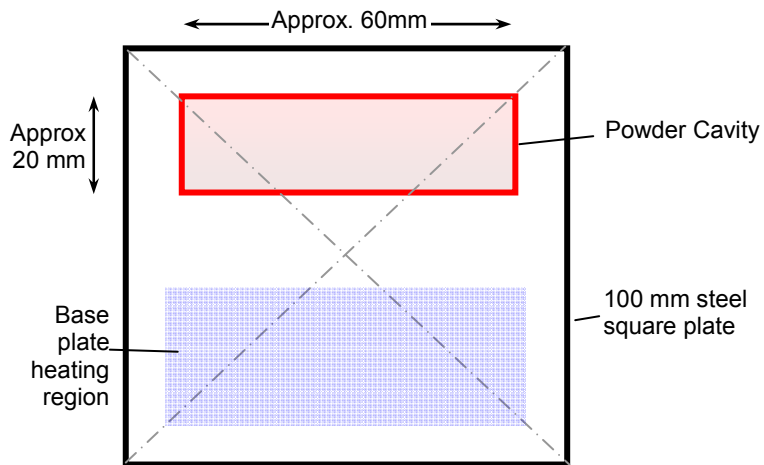


Figure 4-1 Configuration for initial feasibility testing of Al2024

Details of the initial feasibility tests are listed in Table 4-2. These tests were conducted to provide a starting point for the parameters prior to conducting experiments for producing a freeform part (particularly the powder preheating parameters).

Table 4-2 Initial Al-2024 EBM test observations

INITIAL FESIBILITY TESTS FOR AL 2024			
PlateTemp. in °C	Melt cycle	Pre/Postheat	Observations
Cold Start	100 reps 10,000mm/s 0.5-3.5mA 0.5mm offset	None	Sintering and minor Balling
Cold Start	100 reps 10,000mm/s 0.5-7mA 0.5mm offset	None	Cracking of sintered part followed by balling
Cold start	100 reps 10,000mm/s 0.5-4.0mA 0.5mm offset	pod 100 reps 10,000mm/s 4.0-0.5mA 0.5mm offset	Objective: slowly decrease the heat as it would permit the material to flow after it has been melted to prevent balling. This did not help and balling was still observed
Cold start	100mm/s 3.2mA 0.3mm offset	phd 100 reps 10,000mm/s 0.5-5mA	Objective: Uniformly melt the balled powder. Powder segregated into two layers. Top layer balled and bottom layer sintered
300°C	100mm/s 3.2mA 0.3mm Offset	phd 100 reps 10,000mm/s 0.5-5mA 0.5mm offset	Objective: study the effect of a hot start. Observed that hot start did not have any significant effect on the quality of the melt
300°C	100mm/s 1.8mA 0.3mm offset	Phd1 100 reps 10,000mm/s 0.5-5mA phd2 100 reps 10,000mm/s 2-5mA	Objective: higher sintering of powder bed to provide a more stable wettable surface to prevent baling. It was observed that the balling occurred due to sputtering during the melt process.

The next set of experiments were meant to develop parameters for freeform fabrication of aluminum parts. A standard 100mm square, steel start plate and a slice thickness of 0.07 mm was used for manufacturing aluminum 2024 samples (referred to as small samples).

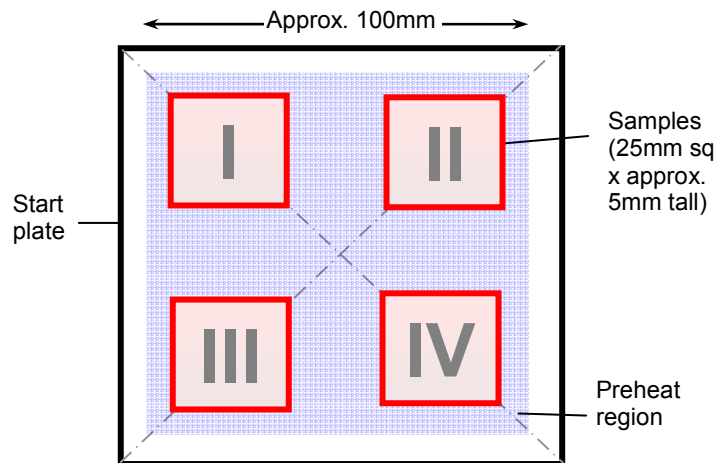


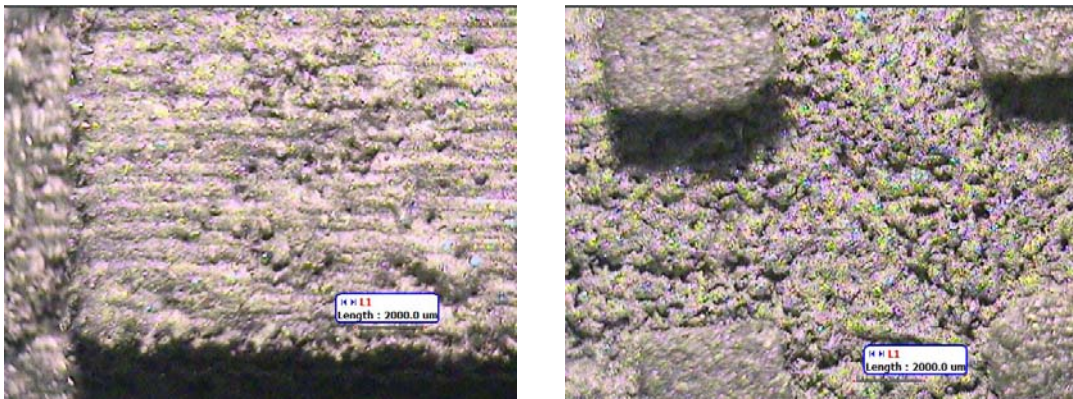
Figure 4-2 Configuration for small sample tests of Al 2024

As shown in the Figure 4-2, four samples with different melt parameters were produced. The objective was to establish parameters that would produce parts that looked visually most acceptable. The details of each of the experiments are listed in Table 4-3.

Table 4-3 Small Sample Build Observations for Al-2024

SMALL SAMPLE BUILDS IN AL-2024					
Plate Temp	Preheat	Sample I	Sample II	Sample III	Sample IV
480°C	50 reps 10,000 mm/s 0.5-6mA	1.8mA, 100mm/s	2.5mA, 100mm/s	1.8mA, 250mm/s	2.5mA, 250mm/s
Observation: Over melting observed in all samples					
550°C	50 reps 10,000mm/s 0.5-6mA, 0.5mm	9mA, 500mm/s	12.5mA, 500mm/s	9mA, 800mm/s	12.5mA, 800mm/s
<p>Observation: Kinetic energy developed by the melt pool pushes excess melt pool off the build region. This material is very loosely sintered powder and is not damaging to the rake. The higher plate heating temperature also seems to be helping in holding the part more firmly to the plate. High scan rates (sample III & IV) prove to be more effective at reduce balling. Low scanning speeds (sample I & II) also seem to permit the beam to melt deeper into the part. Swelling of the surface was also observed in these samples</p> <p>Sample III had the cleanest finish; though overmelting seemed to be occurring in all the samples.</p>					
550°C	30 reps 10,000mm/s 0.5-6mA, 1mm	9mA, 1000mm/s	12.5mA, 1000mm/s	9mA, 1300mm/s	12.5mA, 1300mm/s
Observation: The objective of this experiment was to minimize the time spent preheating (also increases powder recovery) and improve the surface finish of the part by speeding up the melting and reducing overmelting. It was observed that the sintering during preheating can further be reduced. The parts obtained during this experiment also showed strong evidence of overmelting.					
550°C	30 reps 10,000mm/s 0.5-5mA, 1.2mm	9mA, 2000mm/s	12.5mA, 2000mm/s	9mA, 3000mm/s	12.5mA, 3000mm/s
Observation: Samples I & II exhibit swelling of the top surface and this is more prominent in sample II. Sample II & IV have a relatively flat top surface but they might have a small amount of porosity as small pinholes were observed in the top surface.					
550°C	30 reps 10,000mm/s 0.5-5mA, 1.2mm	9mA, 2000mm/s	12.5mA, 2000mm/s	9mA, 3000mm/s	12.5mA, 3000mm/s
Observation: THIS EXPERIMENT WAS CONDUCTED WITH A SLICE THICKNESS OF 0.1MM IN ORDER TO SPEED UP THE PROCESS. It was observed that the surface of the samples was not as flat as those obtained in the previous experiment. The excess melt pool build up was higher. It was decided that for the current set of experiment it would be more appropriate to use a slice thickness of 0.07mm.					

Since the objective of the study was to develop parameters for freeform fabrication of aluminum parts, a set of experiments was carried out to develop parameters for building overhanging structures. Experiments conducted thus far have not produced a concrete set of parameters for overhanging structures, therefore details of the experiments are not provided. Figure 4-3 clearly shows a more porous surface finish obtained for an overhanging surface.



Top surface of an Al-2024 part made on the Arcam EBM S12 system

Overhanging surface of an Al-2024 part made on the Arcam EBM S12 system

Figure 4-3 Surface roughness of initial Al-2024 specimens

The next set of experiments was to make comparisons between the ultimate tensile strength of Al-2024 parts produced via the EBM system and values expected from parts produced by conventional manufacturing. Tensile test specimens as dictated by ASTM-E8 standards with suitable machining allowance were fabricated via the EBM system (Figure 4-4).

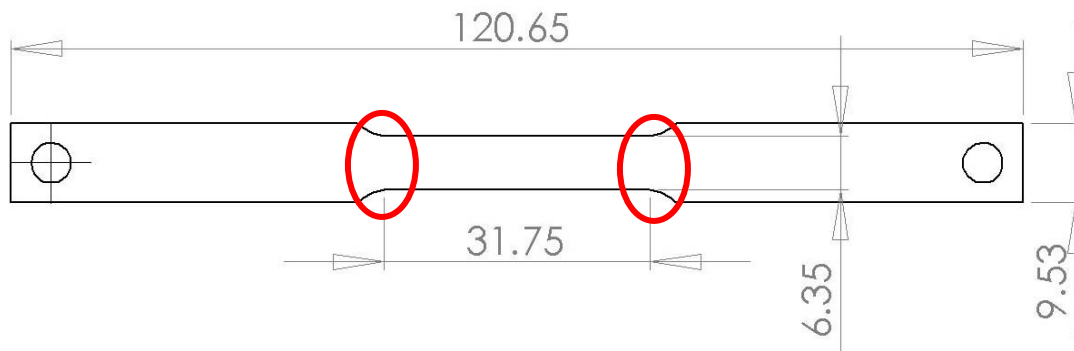


Figure 4-4 ASTM E-8 tensile test specimen dimensions in millimeters

The cross section of the melt region of these tensile specimens was considerably larger than that for the small samples described previously. Two observations were made in this case:

- The parts very frequently cracked during the removal from the steel build plate in the regions showed in the above diagram. The reasons are not entirely clear. It could be due to a combination of the following factors
 - The regions become areas where the shear forces are maximum during the part removal
 - Residual stress build up due to differences in the thermal expansion of steel and aluminum
 - Molten aluminum dissolves steel.
- Due to the larger surface area of the specimens, a larger weld pool was formed as the beam traversed over the scan area. The weld pool behaved very similar to an

ocean wave, where the pool would build up to an extent where it would spill back onto the melted part causing either waviness or balling on the surface (see Figure 4-5). This problem was solved by sub dividing the scan area into smaller regions that are randomly selected for scanning by the beam. This decreased the size of the weld pool, and the top surface of the part had a fairly reasonable surface finish.

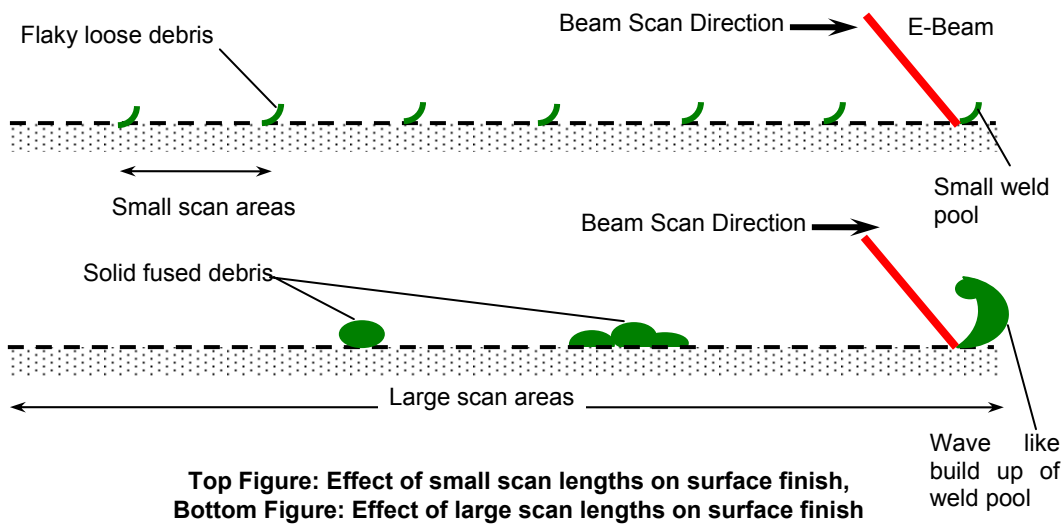


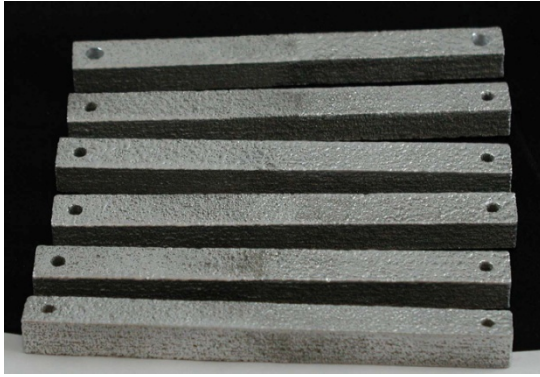
Figure 4-5 Effect of scan length on Al-alloy 2024's surface finish

Simple rectangular bars were made on the EBM as an alternative to the near net shape ASTM E-8 specimens. Subdivision of the melt area was also incorporated into these builds. Six specimens each were built for each of the four combinations of process parameters.

Table 4-4 Processing conditions for Al-2024 test specimens

TENSIL TEST SPECIMENS IN AL-2024					
Start Plate Temp	Preheat	Sample I-I	Sample I-II	Sample II-I	Sample II-II
550°C	30reps 10,000mm/s 0.5-6mA	9mA, 3000mm/s	12.5mA, 3000mm/s	9mA, 2000mm/s	12.5mA, 2000mm/s

Figure 4-6 shows photographs of the top and side surfaces of the specimens after wire brushing.



SAMPLE I-I



Sample I-I side



Sample I-I top



SAMPLE I-II



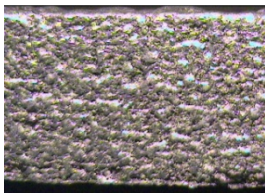
Sample I-II side



Sample I-II top



SAMPLE II-I



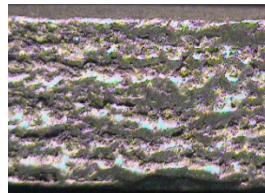
Sample II-I side



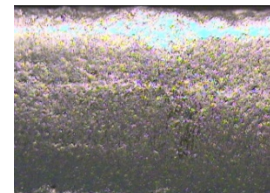
Sample II-I top



SAMPLE II-II



Sample II-II side



Sample II-II top

Figure 4-6 Photographs of Al-2024 Test Specimens

The specimens shown in Figure 4-6 were made with different processing parameters. The top and side views were of the top and side surfaces of the sample taken at 1X magnification.

An approximate calculation of the densities of the parts was carried out under the assumption that the cavities were made from perfect cylinders and the faces were perfectly square with reference to one another with mirror finish.

Table 4-5 Density and porosity in Al-2024 specimens

	SAMPLE I-I	SAMPLE I-II	SAMPLE II-I	SAMPLE II-II
DENSITY	2.273g/cc	2.512g/cc	2.425g/cc	2.519g/cc
POROSITY	18.25%	9.635%	12.787%	9.383%

Hardness of the samples was also measured across the various surfaces using the Rockwell tester, however there was a large variance in the readings. This could be either due to sub surface porosity, unevenness of the surface or inaccuracy of the testing machine.

The dimensional accuracy of the parts based on the processing parameters has not been measured, as the shrinkage and the weld pool diameter for these samples has not been established. This is a topic for future consideration.

The samples were machined on a Cincinnati Millacron vertical machining center to form the ASTM E-8 specimens. Some of the samples broke or developed cracks during the machining process. The specimens were then tested using an ATS computerized Universal Testing Machine (UTM) at a crosshead feed rate of 0.58 mm/min.

The graphs in Figure 4-7 through 4-10 show load vs. displacement in these samples.

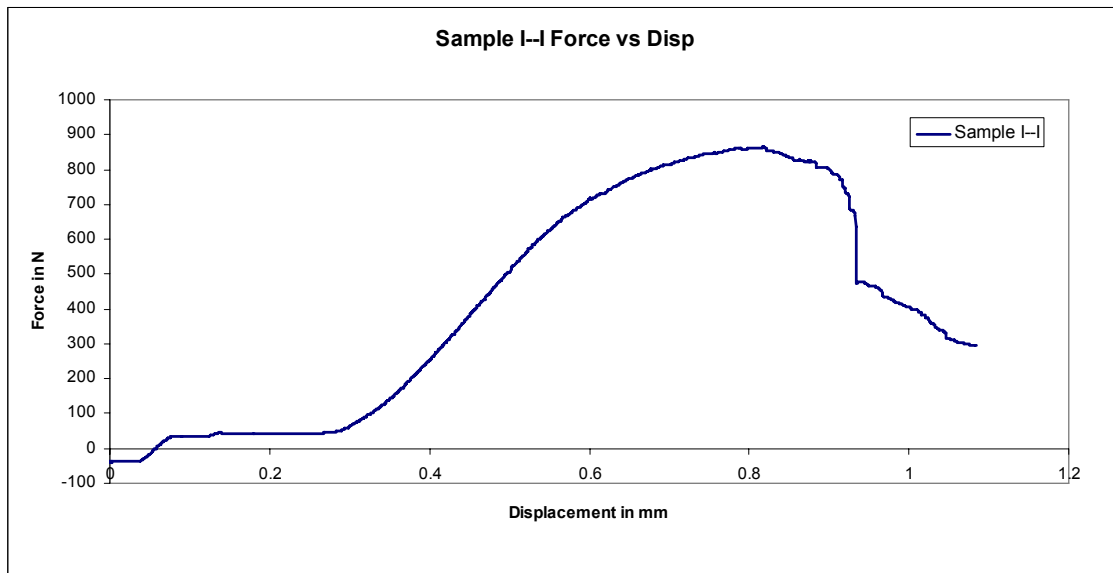


Figure 4-7 Sample I-I with UTS of approximately 21.25 MPa

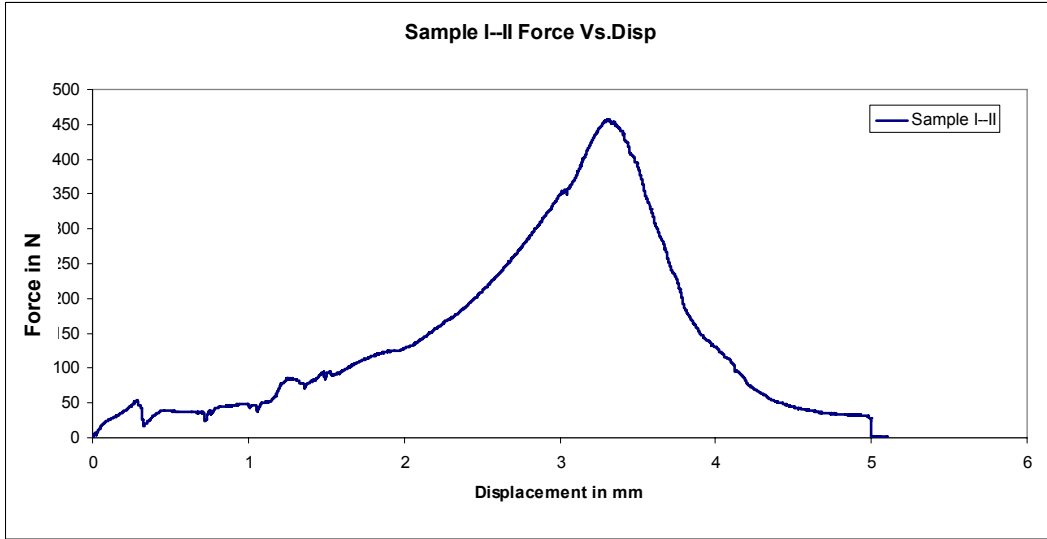


Figure 4-8 Sample I-II with UTS of approximately 11.25 MPa

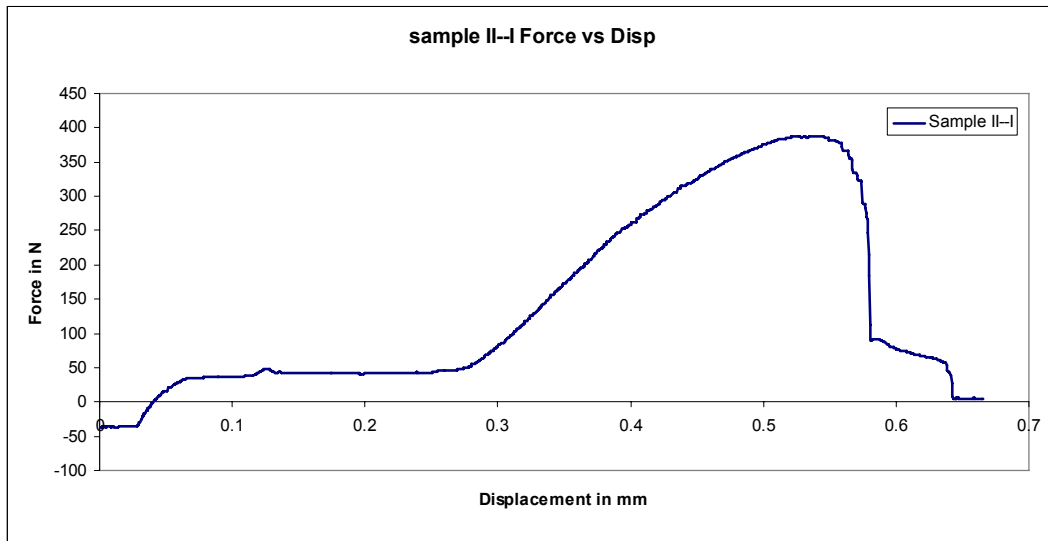


Figure 4-9 Sample II-I with UTS of approximately 10MPa

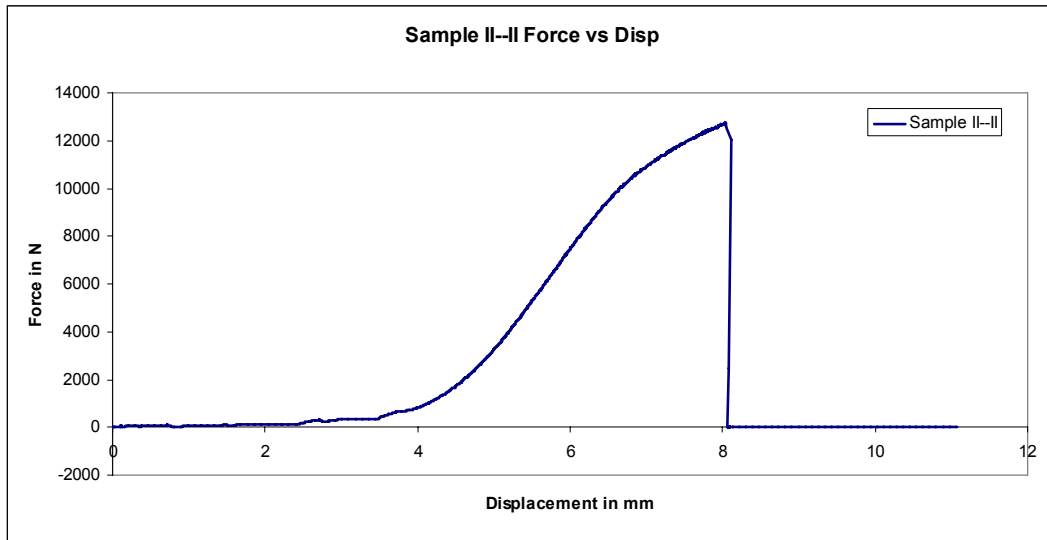


Figure 4-10 Sample II-II with UTS of approximately 325MPa and elongation of 1.57%

Based on the force vs. displacement plots, no specific trend could be established between the part strength and the part finish, density and the process parameters. The only perceivable trend is that the gradual failure of samples I-I, I-II, II-I indicate a porous but sintered structure on the inside. This is not evident from polished sections of the samples, as aluminum in the samples has a tendency to smear during the polishing process. Etching of the samples was carried out using Keller's reagent to reveal the nature of the samples microstructure.

It was suggested that T-6 tempering might increase the ultimate tensile strength of the specimen due to solution treatment (precipitation of CuAl_2) and aging [82]. The heat treatment cycle involved the following

- Annealing: The sample was heated from room temperature to 800°F at 1.3°F/min and held there for three hours. The sample was then cooled to 123°F at 1°F/min. The sample was then cooled in the furnace to room temperature
- Solution treatment: The sample was held at 920°F for 1.5 hr. and water quenched within 10 seconds of removal from the furnace
- Ageing: The samples were aged at 375°F for 11 hrs. and the samples were cooled to 123°F at the rate of 1°F/min.

The dimensions of each of the samples were monitored during every stage of the heat treatment and no significant change in the dimension or distortion of the surface was observed. The heat-treated samples were tensile tested again to inspect the effect of treatment cycles on the part strength. Results of these tests are shown in Figure 4-11 through 4-14.

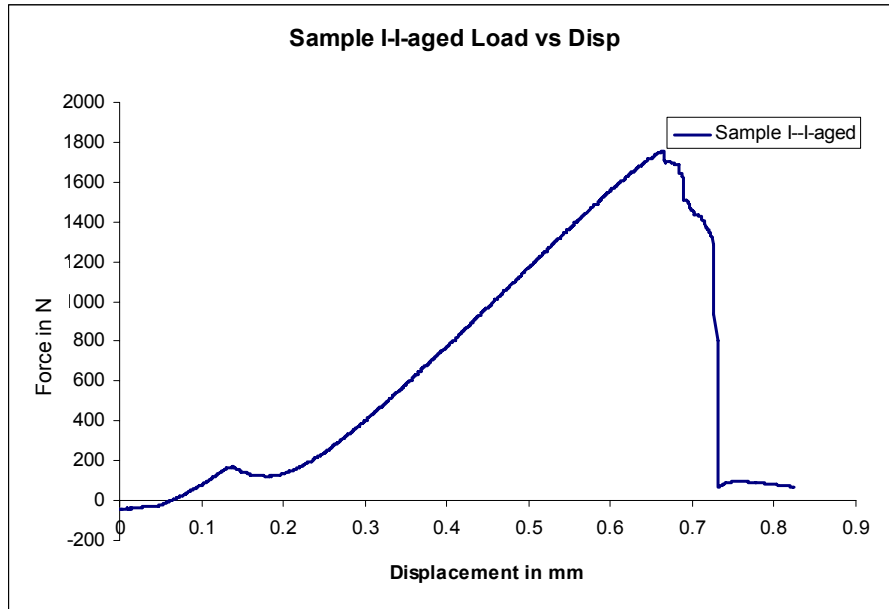


Figure 4-11 Sample I-I Aged, UTS approximately 42.5MPa

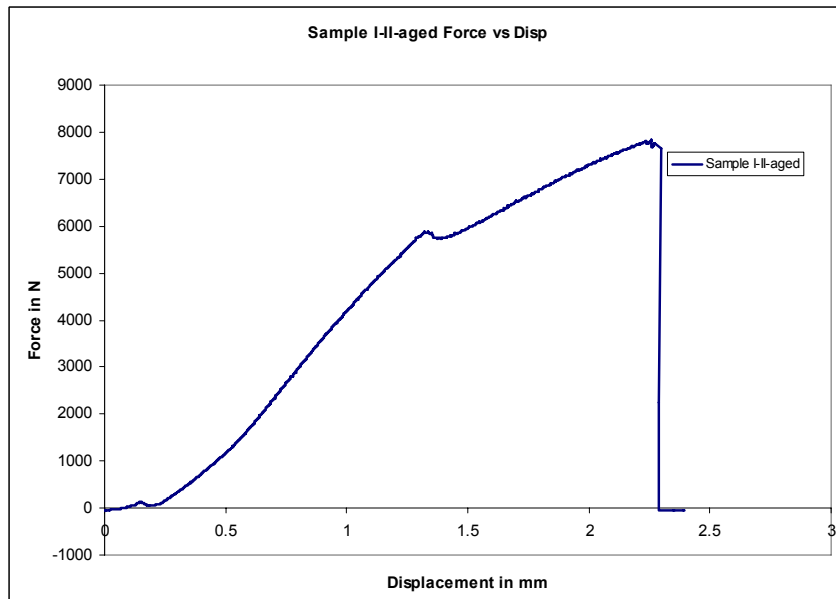


Figure 4-12 Sample I-II aged, UTS of approximately 187.5MPa

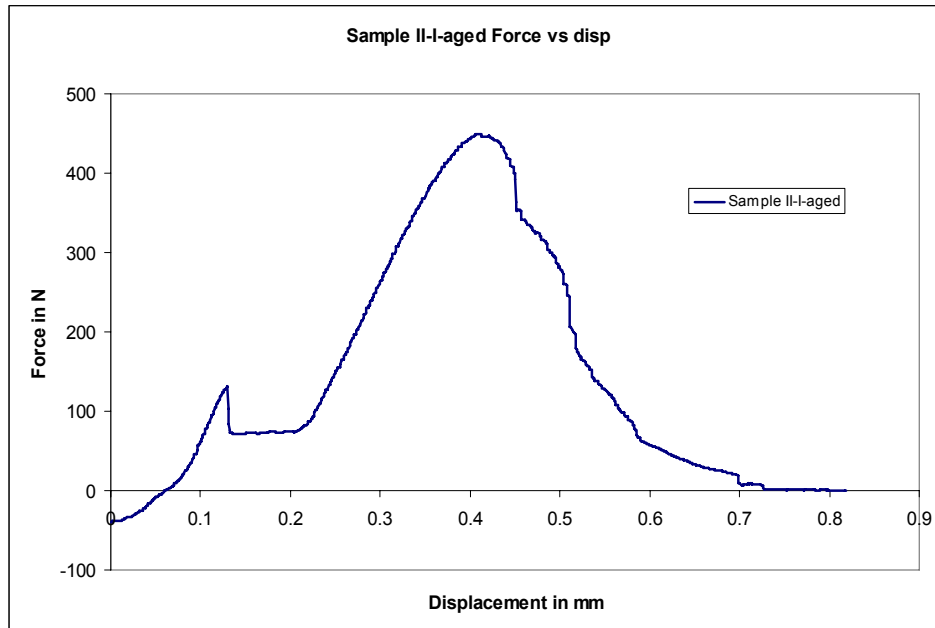


Figure 4-13 Sample II-I aged, UTS of 11.5MPa

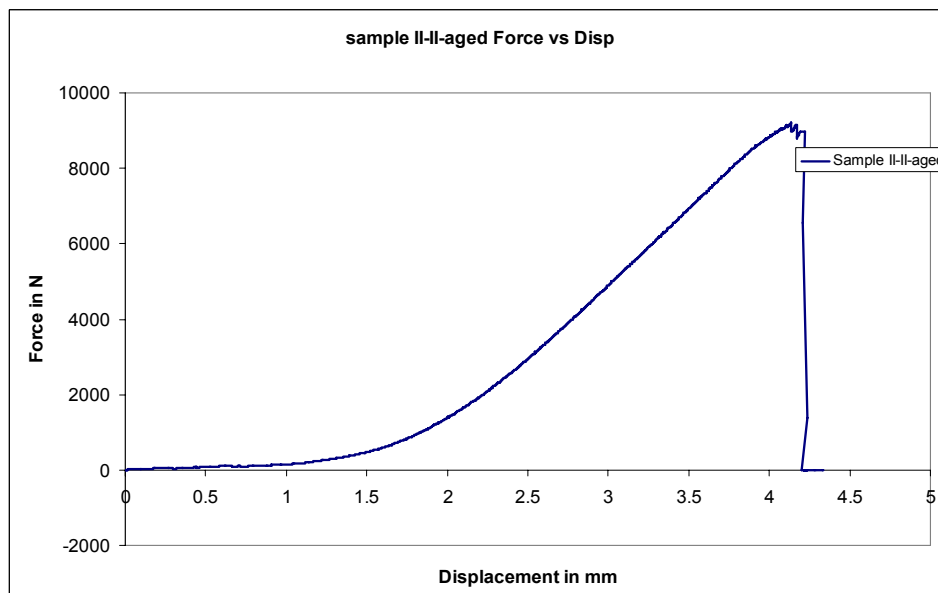


Figure 4-14 Sampled II-II aged, UTS of 225MPa

A comparison between the Ultimate Tensile Strength of the samples before and after heat treatments is shown in Table 4-7.

Table 4-6 UTS comparison of as-processed and aged Al-2024 specimens

	Sample I-I	Sample I-II	Sample II-I	Sample II-II
UTS- raw	21.25MPa	11.25MPa	10MPa	325MPa
UTS-aged	42.5MPa	187.5MPa	11.5MPa	225MPa

The samples had numerous cracks and composition of the processed parts was never determined. Heavy evaporation of the alloying elements during the processing of the part could have caused the inconsistencies in the strengths of the raw and aged parts. More experiments are necessary to mitigate cracking and evaporation in these parts. A larger sample size is also necessary to statistically validate the results.

As stated earlier, a substantial loss of magnesium is expected in the fabricated sample based on the current processing parameters. Monitoring of the composition of the samples via inductively coupled mass spectroscopy might reveal the effect of the processing parameters on alloying materials. Another phenomenon that occurs in these samples is the dissolution of steel from the steel start plate into aluminum. Alternative start plate materials or isolation of the sample from the start plate need to be studied.

An alternative to reducing the cycle time and cost for producing forged quality Al-2024 parts would be to convert the process steps multi-stage forging operation to a two or three stage operation.

- Stage I Produce a slightly oversized Al-2024 component on the EBM system with minimal alloying element loss.
- Stage II Heat treat the part to give it necessary strength and ductility
- Stage III single step forging of the part to produce the final part conforming to dimension and strength requirements

This would reduce the cost of tooling for a low volume production part to a single tool.

The feasibility of processing Al-2024 components via the EBM process was demonstrated by fabricating a fairly complex turbocharger with lightly overhanging surfaces (Figure 4-15). The processing parameters used were same as those for “Sample I-I”.

The material composition of EBM processed Aluminum alloy 2024 was not verified. The ineffectiveness of solution treatment could be explained by a possible depletion of the alloying elements like Magnesium and Zinc.



Figure 4-15 Turbochargers fabricated in Al-2024 via the EBM process

4.2 Non-Stochastic Al-2024 Foams

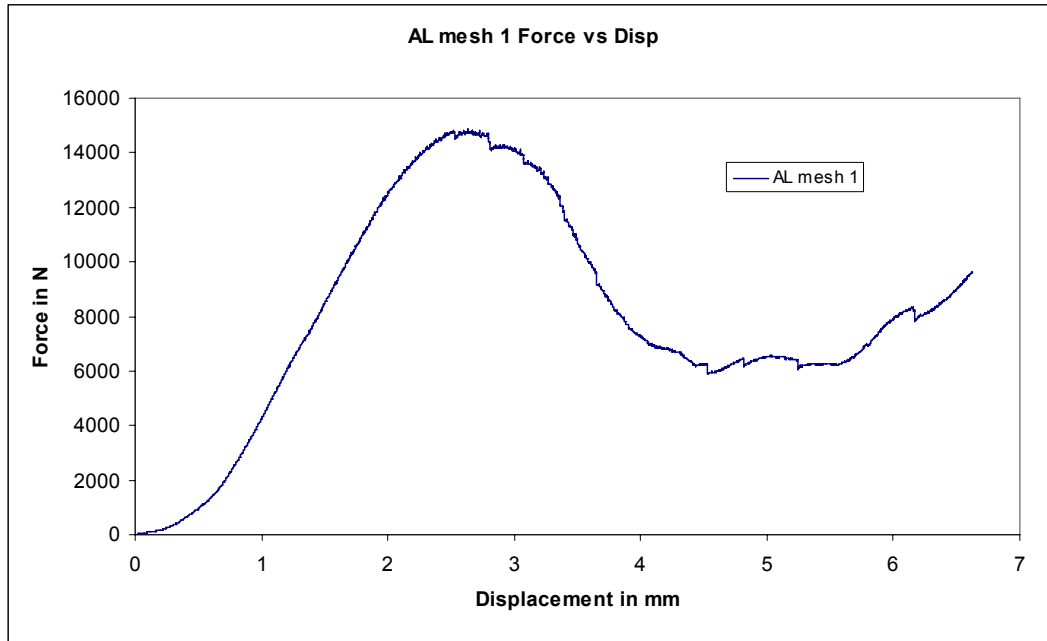
The light weight, high rigidity, impact absorption and high conductivity of aluminum makes it a good candidate for manufacturing foams serving as either heat exchangers or structural components [83]. The processing parameters for manufacturing foam structures on the EBM system greatly vary from those used for making bulk components.

Open cellular Al-2024 foams were produced having pore sizes of 4 mm. The samples were approximately 25 mm square and about 12 mm tall. In the first experiments, the scan speed was varied between 1000 mm/s and 650 mm/s and the current was varied between 3 mA and 4 mA. A considerable amount of sputtering was observed during the

experiment, and the meshes produced were so weak that they ruptured during the raking operations.

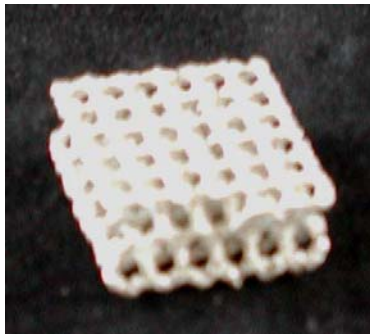
The next set of experiments were carried with scan speeds varying between 300 & 500 mm/s and the current varying between 3-4 mA. Testing revealed that specimens produced with a scan speed of 300mm/s were stronger than those produced at 500 mm/s. The surface texture of these meshes held a resemblance to those produce with Ti-6Al-4V, but the Al-2024 meshes were fragile enough to crack under touch.

Combinations of process parameters were tried until a scan speed of 100 mm/s and a current of 3 mA was finalized for mesh structures. The surface of the meshes produced with these parameters was drastically different from the previous experiments. The parts had a very smooth, mirror like finish. The high amount of energy led to slight overmelting that was evident from the thickening of the beams to almost 1.5 mm in diameter (traditional mesh structures have a beam diameter ranging between 0.7-1.0 mm). Since the height of the structure was small, the mass and density was not tracked as a lot of variations are caused in the first few layers of a build. The smallest cross section of this test sample was approximated to be roughly 64 mm². This specimen was loaded under compression at a rate of 0.58 mm/min. Figure 4-16 shows the plot of load vs. displacement.



a)

Load Vs. Displacement plot for Al2024 mesh structure



b)

Aluminum 2024 mesh before compression



c)

Aluminum 2024 mesh after failure

Figure 4-16 Aluminum Mesh Load Vs. Displacement Test Results

Unlike titanium meshes, the Al-2024 mesh exhibits plasticity, wherein the mesh gradually gives in to the point where it is compressed flat and further compression of the

specimen is mostly in the form of compression of the bulk material rather than the mesh structure. This is evidenced by the increase in the applied force for the second time in order to generate a strain in the sample.

4.3 Conclusion

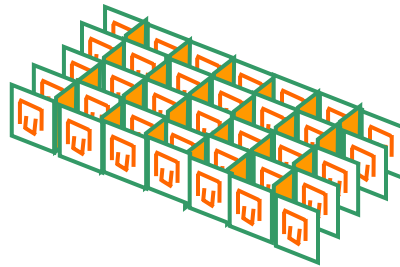
This study has proven the feasibility of manufacturing aluminum components via the EBM process. A parallel study of the effects of process parameters on part strength, porosity, alloy composition and grain structure is required to produce commercially acceptable freeform components. As previously mentioned, heat treatments and secondary processing methods also need to be explored to produce feasible parts. The first few experiments on the feasibility of processing aluminum alloy 2024 were conducted using aluminum start plates, but this was halted because of the ability of the electron beam to cut through aluminum plates. The use of the aluminum start plate must be reinvestigated in order to reduce differences between the coefficient of thermal expansions between the start plate and the part being built over it. The alloying elements are critical for the strength of aluminum alloy 2024. The relationship between the processing parameters, the vacuum chamber conditions and vaporization of the alloying elements should be investigated further.

Chapter 5 Electron Beam Melting of Metamaterials

5.1 Introduction

In 2006, researcher at Duke University and Imperial College announced that they had developed a man-made class of materials called metamaterials. Conventional “solid” materials respond to external stimuli such as, mechanical load, electromagnetic radiation and sound, due to the periodic arrangement of the atoms and molecules that make them up. Metamaterials are made up of tailored periodic micro or meso-structures that manifest themselves to produce bulk properties that are different from the material they are made of.

The unit structures of the negative refractive index materials in superlenses and “invisibility cloaks” demonstrated by researchers out of Duke University and Imperial college consisted of periodically arranged C rings (Figure 5-1). These structures behave like LC circuits when light passes through them. The induced current gives the structure an artificial negative permeability and permittivity; both direct contributors to the refractive index of a material.



(Source: [84] [85])

Figure 5-1 Negative refractive index materials developed using a C-ring resonator

Photonic crystals operate based on the Bragg's principle, in which the topology of the structure selectively filters light of a particular wavelength [86]. These structures can also be used to make light bend at perfect right angles without having any loss of energy or information.

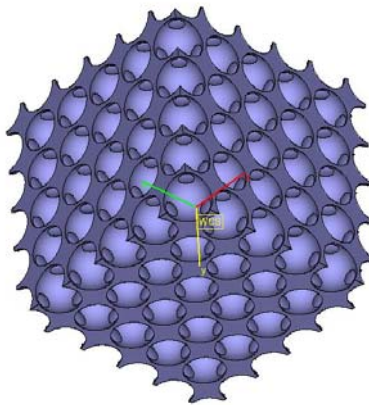


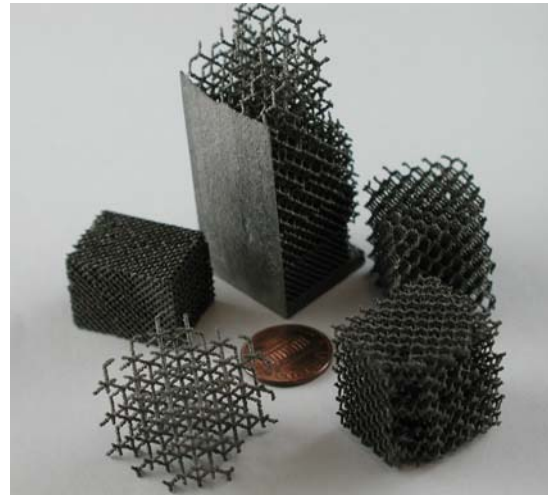
Figure 5-2 An ordered structure similar to a 3D photonic crystal

The simplest and most common form of meta-materials would be any kind of solid foam. Foams have been used in many day to day applications, but their properties are primarily

governed by random ordering in the structure (Figure 5-3). A more controlled tailoring of mechanical foams would have strong implications in the aerospace and bio-medical industry.



Scouring pad is as example of stochastic foams



Non-stochastic foams produced on the Arcam EBM system

Figure 5-3 Examples of stochastic and non-stochastic foams

Acoustic crystals, or objects for redirecting, focusing and filtering sound waves (mechanical elastic waves) are also being investigated by researchers. Structures as simple as face centered cubic arrays of tungsten carbide balls in epoxy are known to exhibit 3D phononic crystal properties[87].

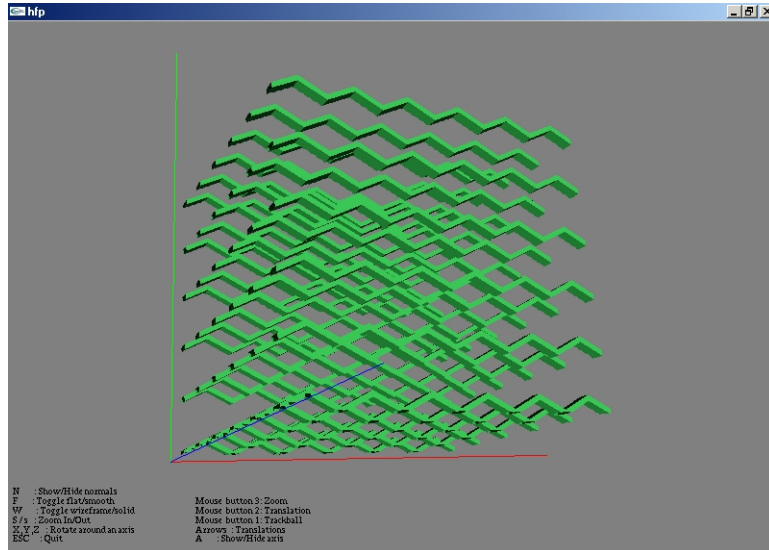
Most metamaterials are fabricated using metallic or dielectric materials. The electron beam melting process gives the user the capability of directly or indirectly developing controlled heterogeneous behavior in this complex new class of materials.

5.2 CAD Issues

In order to manufacture non-stochastic foams using additive manufacturing techniques, it becomes imperative to develop a means of defining parts geometries for foam lattices. The simplest route to achieve this is to use commercially available solid modeling systems. That is the route first taken in this research effort. Commercial CAD software were stable when working with simple unit structure geometries and a very small number of unit elements. At the early stage of this work, two methods were experimented with for developing the CAD models; manipulating the geometry to satisfy the CAD modeler, or, developing alternate modeling methods to accommodate complex geometries.

In order to use a commercial CAD modeler it was necessary to limit unit cell geometries to a collection of beams with rectangular cross sections. This minimized the number of triangles in the STL file. An experimental geometry scripting language called Hyperfun (Figure 5-4), based on functional representations was also tried [88, 89]. This software permits one to model the object using a single function to define the entire object. The properties of the object are extracted by solving the function over a multidimensional grid. The main advantage of this method is the reliability with which the geometry is

extracted. It is also possible to bypass the process of extracting an STL file and directly generating a file in the SLC format. The main disadvantage is its poor user interface.



(Courtesy Prof. Alexander Pasko, Hosei University, Japan)

Figure 5-4 Grid generated using Hyperfun

In order to accommodate more complex lattice structures, a tool was developed to test the concept for seeding a constrained stochastic grid into a discretized 3D space. The constraints were the manufacturing limitations set by the EBM process and methods for achieving uniform distribution of the grid. The mesh structure was modeled as a set of vectors at different angles to the XY plane. A cross-section was assigned to them. This permitted the user to bypass the generation of an STL file. The other advantage is that the modeling process ends up looking like a graph. It might be possible for researchers to

develop a heuristic to generate engineered stochastic structures where a structure's graph could be modified so as to meet specific engineering needs.

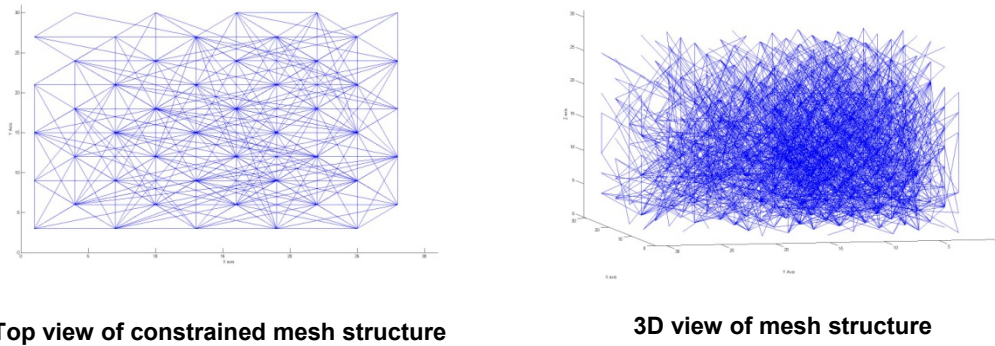


Figure 5-5 Discrete constrained stochastic mesh structure

5.3 Metal Foams

Cellular metal structures can be divided as stochastic foams with open or closed cell structures and non-stochastic structures with repeating lattice structures. Numerous methods have been used for making stochastic metal foams [90, 91]. Closed cell stochastic foams are typically produced by adding gas directly to the melt, adding gas releasing blowing agents or causing precipitation of gas bubbles [92]. The process is controlled to achieve the desired pore size, shape, and pore distributions, which in turn influence the material properties [93]. Closed cell structures are also made using entrapped gas expansion, or with hollow spheres entrapped in a matrix [90]. Closed cell foams have great potential for energy absorption and acoustic damping [94, 95]. Open cell stochastic foams are generally made using melt processing, powder processing and

deposition methods. The commercially available open cell metal foam, Duocel (ERG, Oakland, California), uses investment casting of polymer foam for aluminum and copper. Metal deposition on cellular polymer foam has been used for different materials as well. In the INCO process, nickel carbonyl decomposed and deposited over the polymer foams at low temperature. Nickel foams made this way are available commercially as INCOFOAM®. In the Trabecular Metal®, carbon skeletons are first obtained by pyrolyzing thermosetting polymer foams with repeating dodecahedron structure. Tantalum film is then deposited onto the carbon skeleton via chemical vapor deposition (CVD). Pore size and density of the original polyurethane foam affects the pore size and mechanical properties of the Trabecular Metal®. This process results in a favorable microstructure resulting from proper orientation during deposition and crystallographic growth. Trabecular Metal® has been reported to have superior mechanical properties with elastic modulus of Trabecular Metal®, (3GPa) similar to cancellous (0.1-1.5 GPa) and cortical bone (12-18 GPa) [96]. Combustion synthesis has also been used to produce metallic foams. Reactants are mixed, cold pressed and placed in an inert atmosphere and ignited to start the thermal explosion mode or self-propagating high thermal synthesis. Zhang et al. [97] used combustion synthesis to produce porous surfaces having bone ingrowths without immune response. Stochastic cellular structures can be built with different cell sizes, cell wall thicknesses and imperfections as shown in Figure 5-6. Those imperfections cause local deformations in all stress states as shown in studies [98, 99].

Load supporting applications of these materials are limited by their low elastic moduli and strengths [100].



Figure 5-6 Stochastic copper foam

Open cell structures have been used for cross flow heat exchangers and impact loading. Better properties have been observed with repeating open cell structures than with stochastic foams [101]. Various processes are available to make repeating cellular structures and some are reviewed here. Li et al. [102] plotted a slurry consisting of Ti-6Al-4V powder suspended in an organic binder using an experimental rapid prototyping method called 3D Fiber Deposition (3DF) to form a 3D part. The part was post-processed in order to burn off the binder and sinter the titanium alloy powder. The resulting porous titanium structure exhibited a porosity of 88% and a compressive strength of 10 MPa. Wadley et al. [103] discussed manufacturing methods of periodic cellular metals such as deformation forming, metal wire approaches, and investment casting. Metallic sandwich panels with periodic open cell cores were found to possess

better load sustaining capabilities than stochastic foams. Chemical etching to make 2d titanium mesh layers for 3D pattern assembly to use in bone ingrowths surfaces has also been demonstrated [104]. In this research, 10 layers of 100 μ m thick titanium 2D meshes were bonded by heat processing at 900°C. Porosity of the structure was around 80%. Solid free form fabrication methods have advantages when it comes to processing complex parts with slicing geometries at predefined layer thicknesses. Three dimensional printing has been used to make textured patterns for bone ingrowth application [105]. Direct manufacturing of metal lattice structures are possible with laser based and electron beam based systems. For instance, three dimensional mesh structures in stainless steel and cobalt-chrome were built with Selective Laser Melting (SLM) technology. The meshes resulted in nearly 90% reduction in weight at the MCP group (www.mcp-group.com). However, properties of the laser based lattice structures have not yet been reported in the literature.

5.4 Manufacture of Non-Stochastic Metal Meshes on the EBM

The idea for experimenting with non-stochastic mesh structures was born out of the need for developing customized implants in Ti6Al4V. Several objectives were set for the preliminary research. The first was to experiment with process settings needed to fabricate these mesh structures. The second was to determine limits on the achievable feature sizes and cell densities. A third objective was to select one cell geometry and gather preliminary material properties.

As described earlier, mesh structures built on the EBM system were defined as beams. The cross section of the beams was maintained as low as possible; typically 0.1-0.2mm beam thickness in the CAD model. The structure build on the machine had a beam thickness of about 0.7mm (Ti-6Al-4V meshes).

The small cross-sectional area meant that the melting was going to occur as a single contour scan without a need for hatched scans. In other words, the system will not attempt to melt the area inside the contour due to the fact that the area is less than or equal to the melt pool size and is automatically created when the contour is melted. The Arcam EBM build themes for scanning Ti-6Al-4V involved high scan speeds and current. If such a theme is used, the beam would scan a contour and return to starting point before the powder had sufficient time to discharge the electrons. This led to serious particle charging and repelling. A theme was developed for scanning the powder at speeds of around 180 mm/s at low currents to lessen the likelihood of excessive particle charging.

All mesh structures produced on the EBM include overhanging surfaces. This requires the preheating parameters to be developed with extra care. Insufficient sintering of the powder bed would lead to imperfections in the part geometry and/or particle charging. However, excess sintering of the powder leads to inefficiency in powder retrieval, thus making it crucial to get the preheat parameters right. It is also to be noted that minor modifications are required to the preheat parameters for mesh structures in order to accommodate for part and mesh geometry.

5.4.1 Mechanical Testing of Non-Stochastic Foams

The lattice structures tested as part of this study were as shown in figure 5-7.

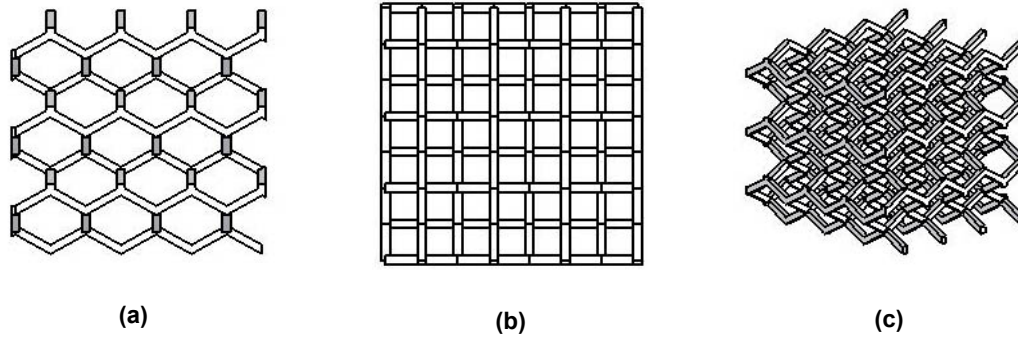


Figure 5-7 Top, front, and dimetric views of hexagonal lattice structures

During initial experimentation, it was observed that lattices whose beams are oriented at an angle of less than roughly $35\text{-}40^\circ$ with respect to the build plane had little or no structural integrity. Figure 5-8 illustrates the problem. The default layer thickness with the Arcam EBM process is 0.1 mm. At this layer thickness, it is clear that discontinuity between the layers starts setting in as the strut angle relative to the built plate decreases for small cross sections. The overlapping distance between adjacent 0.1 mm thick layers can be expressed as $L_1 - L_2$, where $L_1 = T/\sin(\alpha)$, $L_2 = 0.1\text{mm}/\tan(\alpha)$, T is the strut thickness, and α is the angle of the strut with the build plane.

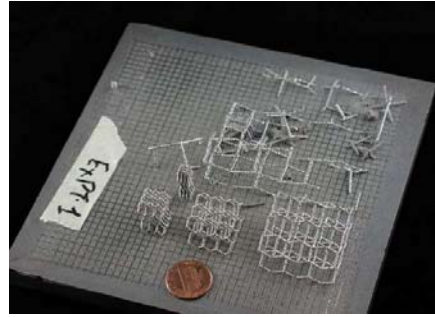
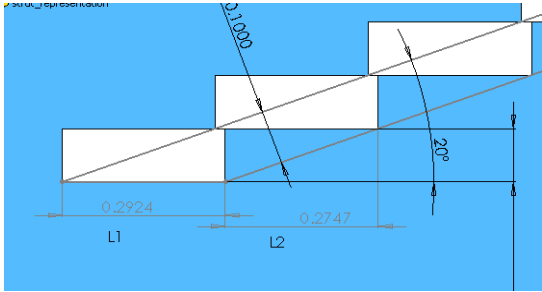


Figure 5-8 Influence of beam angle, beam thickness, and layer thickness on bonding between layers

Figure 5-9 distinctly shows the difference in the quality of interlayer bonding due to variation in the build angles. These micrographs help to illustrate that the research presented here is very much a starting point, and that further process optimization aimed at improving strut quality is expected to yield improved material properties.

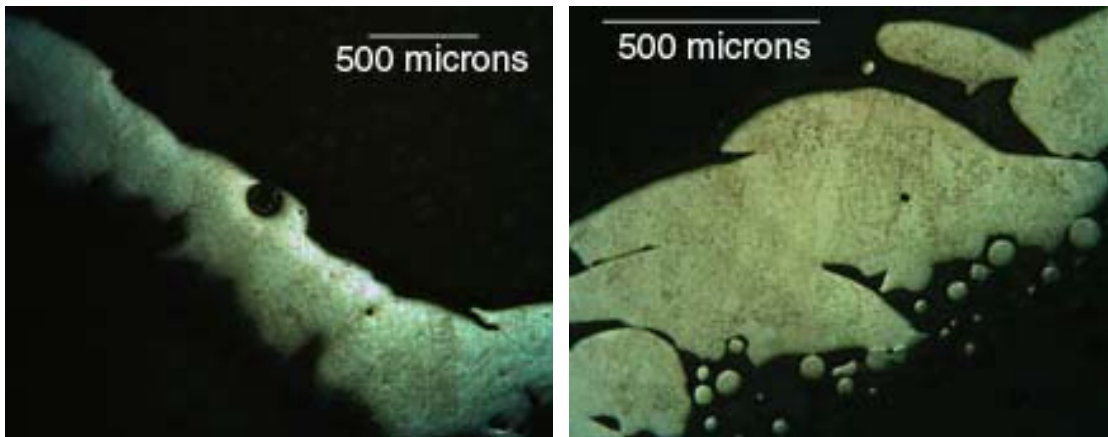


Figure 5-9 Range of strut qualities

Although different cell geometries have been built, the material properties presented in the remainder of this paper pertain to a hexagonal unit cell that was modeled in Solidworks[®]. Unit cells with different overall cell sizes were designed, with each cell

having connecting struts of the same 0.7 mm thickness. By maintaining constant beam thickness while increasing or decreasing the cell size, it was possible to compare lattice material properties as a function of overall density. Magics (Materialise) was used to prepare the build files for fabrication on an Arcam EBM S12 (Arcam, Sweden). Slicing of the files was done at 0.1mm layer thickness. The steel start plate was heated up to 750°C before the first layer of powder was melted using the process conditions previously described. All specimens describe in this paper were built from Ti-6Al-4V powder. Material testing was conducted using an ATS 1605C universal tester. Batches of compression specimens were approximately 25 mm x 25 mm x 25 mm using unit cell dimension of 4 mm, 5 mm, and 6 mm respectively. The specimens were compressed between steel plates at the rate of 5 mm/min. Some samples were also crushed to observe the failure mode. Three-point bending tests were also conducted with the same equipment using a 50.8 mm span. The overall length of the bending specimens was approximately 60 mm. The length : thickness ratio was approximately 4 for all bending specimens. The modulus and compressive strengths for each structure were calculated according to the head-displacement reading from compression tests. Specimens were tested in the directions parallel and perpendicular to build direction. These testing directions are referred to as the XY and Z orientations respectively.

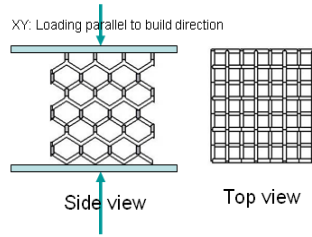


Figure 5-10 Lattice compression test orientation convention

Figures 5-11 through 5-13 show the compression test results for five specimens with 4-mm unit cell dimensions. The XY1, XY2, and XY3 specimens were compressed in a direction parallel to the build direction. The Z1 and Z2 specimens were compressed perpendicular to the build direction. As can be seen from the data, parts loaded parallel to the build direction were stiffer and stronger, but required less work to failure. This trend was also observed for the 5-mm and 6-mm unit cell structures.

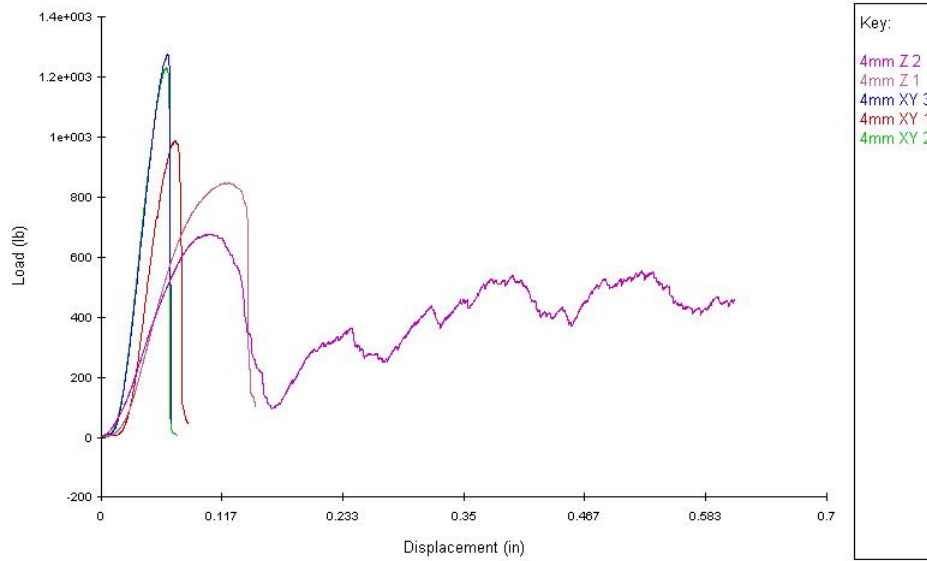


Figure 5-11 Compression test results for 4mm structures with maximum loading up to 1300 lbs

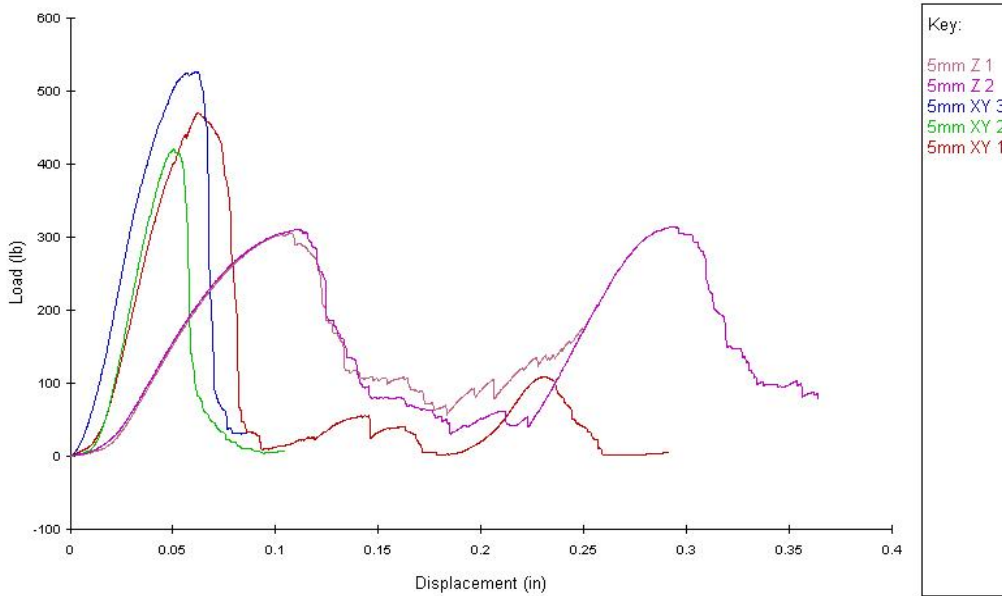


Figure 5-12 Compression test results for 5mm structures with maximum loading of up to 550 lbs

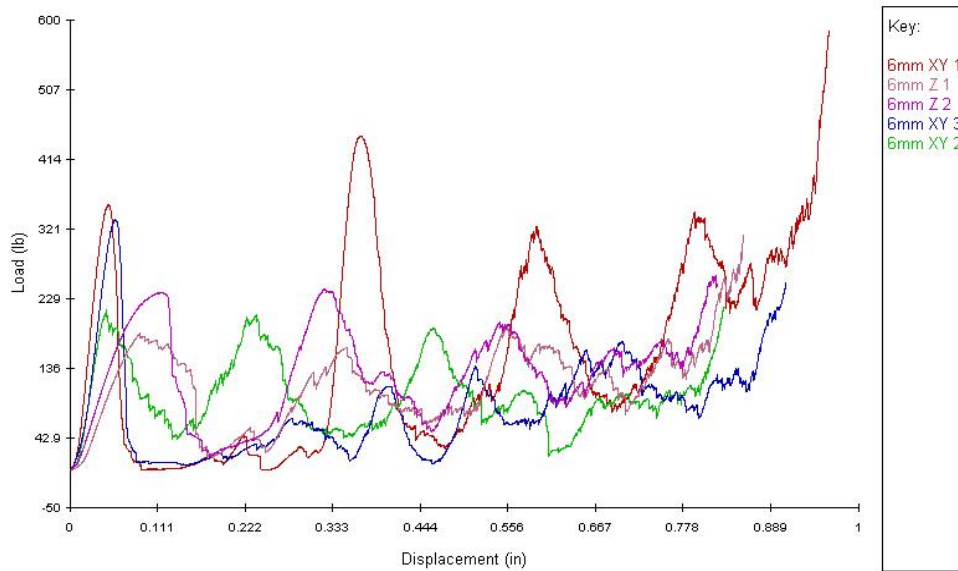


Figure 5-13 Lattice compression test results for 6mm structures

Table 5-1 Summary of lattice compression test results

Specimen	Peak Load (N)	Compressive Strength (MPa)	Strength/Density	E (Mpa)
4mm XY 1	4388.08	7.341	14.780	202.403
4mm XY 2	5472.28	9.344	18.813	211.131
4mm XY 3	5658.57	9.662	19.454	220.283
4mm Z 1.	3754.5	6.684	13.457	79.072
4mm Z 2	2995.16	5.332	10.736	79.072
5mm XY 1	2090.03	4.056	12.203	92.990
5mm XY 2	1868.39	3.626	10.909	114.282
5mm XY 3	2338.1	4.537	13.651	111.523
5mm Z 1	1356.29	2.415	7.265	30.809
5mm Z 2	1394.26	2.482	7.468	29.615
6mm XY 1	2605.46	3.522	14.972	62.730
6mm XY 2	972.51	1.314	5.588	42.050
6mm XY 3	1481.25	2.002	8.512	55.120
6mm Z 1	1398.91	2.429	10.325	22.940
6mm Z 2	1151.79	2.000	8.501	28.376

Table 5-1 shows a summary compression test results for 4mm, 5mm and 6mm structures.

Relative densities were 11.2%, 7.5%, and 5.3% for 4mm, 5mm, and 6mm respectively.

The average measured compressive modulus for specimens loaded parallel to the build direction was 211 MPa for 4mm structures.

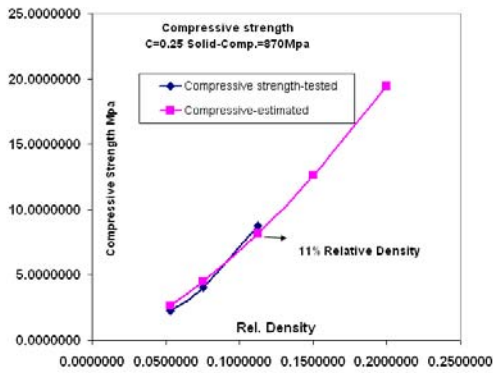
As a means of estimating compressive strength and modulus of non-stochastic foams, structures were built with different cell densities and the appropriate formulas from Gibson and Ashby [100] were consulted. The compressive strength scaling constant was calculated according to the formula

$$\sigma_c = C_1 * \sigma_{c,s} \left(\frac{\rho}{\rho_s}\right)^{1.5}$$

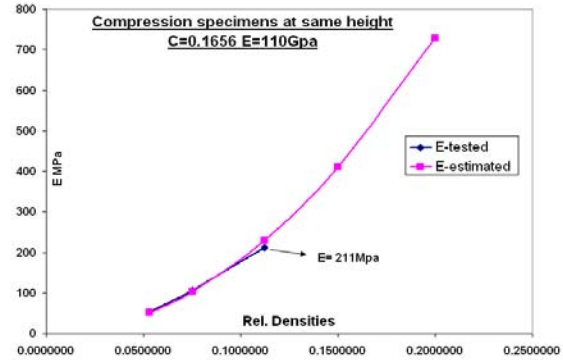
using a solid compressive yield strength of 870 MPa for Ti-6Al-4V. The constant C_1 was set to 0.25 to estimate compressive strength for compression specimens. Density of the solid material is represented by ρ_s , and density of the foam is represented by ρ . The standard modulus scaling formula

$$E = C_2 * E_s \left(\frac{\rho}{\rho_s}\right)^2$$

was used with $E_s=110$ GPa. The constant C_2 (geometric constants of proportionality) was found to be 0.1656. The modulus and compressive strength results are shown in figures below with estimations up to 0.2 (i.e. 20%) relative density.



a) Compressive Strength As a Function of Relative Structure Density



b) Elastic Modulus as a Function of Relative Structure Density

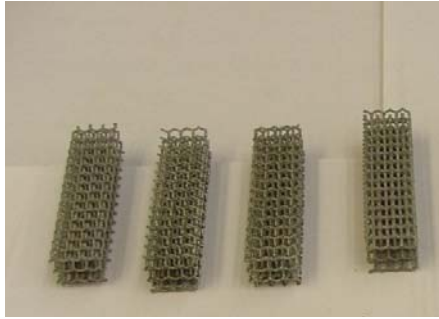
Figure 5-14 Compressive strength and elastic modulus versus relative structure density

Following completion of initial compression tests, a set of bars were fabricated for use in 3-point bending tests. A 50.8 mm span was used for all the tests. Loading was done at 0.5 mm/min for all bending specimens. As shown in the figure below, a subset of the specimens had solid 0.7 mm thick skins built on the top and bottom surfaces. The aim was to increase stiffness and "pin" the ends of the cell struts thus preventing early failure of the meshes.

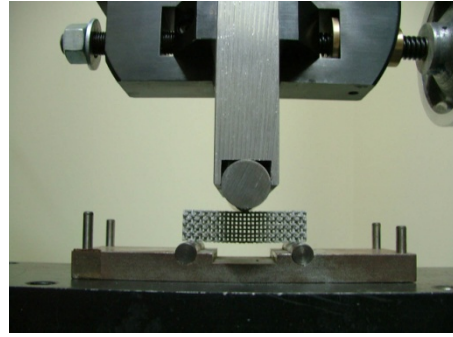
Head displacements were used to calculate the flexural modulus (Figure 5-15) based on the equation

$$E = \frac{(P/y)L^3}{48I}$$

where, E is modulus (MPa), P is load (N), y is deflection (mm), L is loading span (mm), and I is the overall cross sectional moment of inertia (mm⁴).



a) 4mm flexural test specimens



b) Experimental setup for flexural tests

Figure 5-15 Lattice structure flex test setup

Figure 5-16 shows bending test results for the 4-mm structures. The plots with "skin" in the label had the 0.7 mm thick top/bottom skins, whereas the others did not. It is abundantly clear from the plots that adding a thin skin to the specimens significantly increased stiffness and strength, and extended the plastic region.

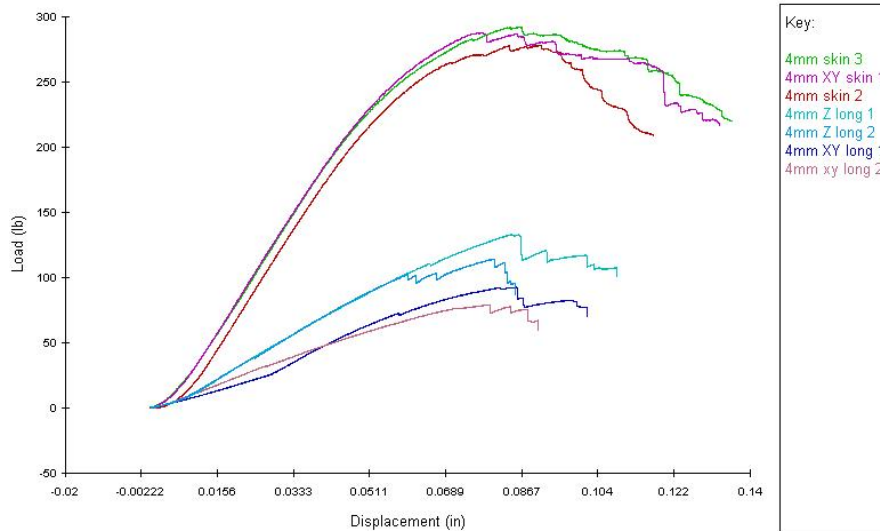


Figure 5-16 Load displacement plots for 4-mm structures

5.4.2 Cryogenic Testing of EBM Manufactured Non-stochastic Foams

The Ultracold Neutron (UCN) Source under construction at the PULSTAR reactor facility at NC State is a solid deuterium source, which will provide densities of 20-30 UCN/cc for fundamental and condensed matter physics. One key element in the system is the DLC (Diamond Like Carbon) coated guide tube which will transport the neutrons several meters from the source to the experimental area. The temperature of the guide will vary from 10 Kelvin near the source to room temperature at the experiment end. In order to minimize the amount of cooling power needed to maintain this temperature gradient, low conductivity titanium structures have been fabricated to support the neutron guide tube. In addition to being a strong [106], low conductivity material, titanium based alloys have very low neutron absorption cross sections, making them ideal for this application. These supports were produced by electron beam melting (EBM) of Ti6Al4V powder. They have complex geometries which make calculating important quantities such as the area to length ratio, also known as the geometrical factor, very difficult. Therefore, a two-step approach was taken that includes physical measurements at cryogenic temperatures and Finite Element Analysis (FEA) to model the thermal behavior of the supports.

Thermal conductivity of a material is defined by,

$$\vec{Q} = -\kappa \vec{\nabla} T$$

where \bar{Q} is the heat flux across a unit area, $\bar{\nabla}T$ is the temperature gradient, and κ is the proportionality between the two, the thermal conductivity [107]. As conductivities often depend on temperature and normally isotropic properties in bulk materials, it is more conducive to describe conductivity in the integrated form,

$$P_{therm} = -\frac{A}{L} \int_{T_{cold}}^{T_{hot}} \kappa(T) dT$$

Where, P is the total heat power conducted across the sample, A is the cross sectional area, and L is the length of the sample. The area to length ratio is often referred to as the geometrical factor, g, especially for complex structures in which an accurate cross section may be difficult to determine.

A material's ability to conduct heat depends on a number of quantities including bonding structure, impurity content, microstructure, and many other factors. Combining these can lead to conductivities which may exhibit strong temperature dependencies, remain more or less constant, or anywhere in between. In the case of metals, the thermal conductivity can be described by a combination of the movement of electrons and phonons within the material:

$$\kappa = \kappa_e + \kappa_p$$

For pure metals, the thermal conductivity is dominated by the electron contribution, κ_e ; however, when high concentrations of alloying elements are present, the contribution from phonons can make up a significant portion of the overall conductivity[108]. Any of these entities can be scattered by one another, as well as impurity atoms, all of which reduces the overall conductivity. At very low temperatures, impurities become the main scattering mechanism, typically leading to constant κ . At high temperatures large numbers of high energy phonons, which elastically scatter electrons, and cause the conductivity to converge to the empirically derived Wiedemann-Franz Law,

$$\kappa^*\rho = L_0 T$$

where ρ is the electrical resistivity, and L_0 is the Lorentz constant, roughly equal to $2.45 \times 10^{-8} \text{ W}\cdot\Omega/\text{K}^2$. However, in between these temperature limits, the relation between conductivity and temperature can be quite complicated as many factors begin to affect the conductivity. Rather than attempting to create a fit for every possible conduction mode, this issue shall be treated by using basic polynomials of sufficient power to account for the general behavior over this intermediate temperature range.

Titanium alloys, notably Ti6Al4V, (6% Wt Al, 4% Wt V), have long been a staple of the aerospace and other industries and are prized for their high strength-to-weight ratios and refractory capabilities. This alloy is an $\alpha+\beta$ alloy, with Al stabilizing the lower temperature α phase, and V the higher temperature β phase. Under equilibrium cooling or thorough annealing, this alloy forms a lamellar, Widmanstätten like microstructure [109].

However, when heated above the β transus at 1340 K and then rapidly cooled at rates of 410 K/s or higher, the body centered cubic β phase undergoes martensitic transformation to hexagonal closed packed α' phase [110]. This leads to a stronger yet brittle material whose properties are especially pronounced at cryogenic temperatures [109]. However, it has also been shown in several materials that martensitic structures have lower thermal and electrical conductivities than their heat treated forms [111, 112]. This occurs because of high densities of dislocations, high angle grain boundaries, and stressed lattice structures in martensitic materials which act as scattering centers for both phonons and electrons.

For this study, the non-stochastic mesh structures were designed using Solidworks and built on Arcam AB's EBM S12 system in Ti6Al4V. Metallographic analysis was conducted on several test specimens to examine the overall microstructure of the material. Standard polishing and etching principles were followed, using a solution of 4mL HNO₃, 3mL HF and 85mL water as the etchant. Optical microscopy was used to examine the samples at varying magnifications, as seen in Figure 5-17. From these images, there appears to exist a mix of a martensitic phase along with lamellar $\alpha+\beta$ [113]. This complex structure is expected due to the incredible anisotropic thermal cycling during the manufacturing process. A more quantitative ratio of these phases could be found by using of x-ray diffraction to compare several characteristic indices.

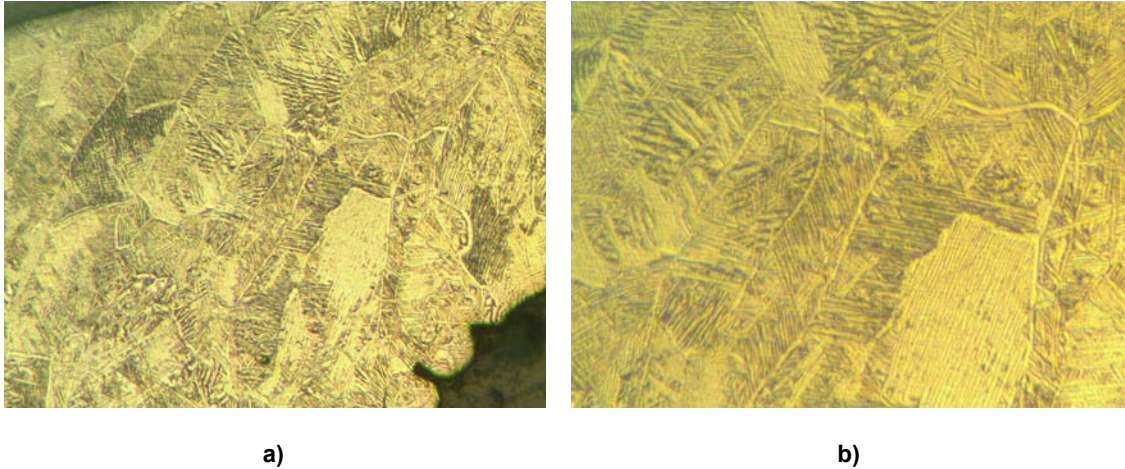


Figure 5-17 Micrographs of EBM fabricated lattice beams (a) 100x, (b) 200x

Three different samples of varying dimensions were fabricated specifically for thermal conductivity measurements. The dimensions of each can be seen in Table 5-2 where one cell is defined to be a hexagonal ring of struts, each measuring 7.6 mm wide and 15.2 mm tall. These cells are interlinked to form a three dimensional scaffold structure, which has a very small area to length ratio and low overall mass.

Table 5-2 Dimensions of samples for conductivity tests

Sample	LxWxH (Cells)	Strut Diameter (mm)
1	4x6x4	1.0
2	4x4x4	1.0
3	4x6x4	0.7
4	4x4x4	0.7



(a)



(b)



(c)

Figure 5-18 Test samples (a) Sample 1 (b) Sample 2 (c) Sample 4

To measure the thermal behavior of the samples, a cryogenic mount was constructed to provide temperatures similar to that of the source. Samples were mounted between two aluminum A1100 alloy blocks, roughly 750g each, by means of steel screws and spring washers through pre-made mounting holes in each sample. Indium wire was crushed between the blocks and sample to decrease contact resistance. The top block was then mounted to the cold head of a Sumitomo RDK 415D cryocooler using similar screws, washers and indium. This two stage modified Gifford-McMahon cryocooler provided up to 45W of cooling power at 50K to the first state, and 1.5W at 4.2K on the second stage. A 25G cartridge heater was placed inside a pre-drilled hole in the bottom block and was connected to four sets of phosphor-bronze wires; two for the external DC power supply and two were used to independently monitor the power delivered to the heater.

To make the temperature measurements, silicon diode temperature sensors were mounted on the blocks next to the sample and were connected by phosphor bronze wires using a four-lead type connection. The cold head, sample, and mount were kept in a high vacuum of 10^{-7} mbar or better by means of an oil-free Varian turbo and scroll pump. A Mylar wrapped aluminum radiation shield was cooled by the 1st stage of the cryocooler, and maintained a temperature of 265K at the warmest point. While this caused significant radiation at lower temperatures, the shield helped to reduce the effects when higher thermal gradients were measured. Once the system was at sufficiently low pressure and the cryocooler started, the system was allowed to cool until a change of less than 0.002 K/min was observed in the bottom block. The heat capacity for this A1100 is 897 J/kg-K at 300K, and 790 at 200K. This means that at most the block absorbed less than 0.02W due to change in enthalpy.



Figure 5-19 Setup of the experiment with sample 1 mounted to aluminum blocks and cryocooler

This cool down process took on the order of several days due to the large heat capacity of the Aluminum blocks, the low conductivity of the samples, and the resistance of the indium contacts.

After the system reached its apparent minimum temperature, power was applied to the heater set in the bottom block to increase the temperature gradient across the sample. The system was allowed to reach the same steady state conditions noted earlier, which generally occurred on the order of 24 hours. This process was repeated several times for increasing applied power from 0.15 to 2.0W for each sample.

The temperatures of the bottom block for each sample have been plotted against the applied power, seen in Figure 5-20. For each sample, the temperature of the top, or cold, side increased by less than 3K between the minimum and maximum applied powers. The data can be seen in Table 5-3. Because the conductivity remains practically the same over these small variations, this can be differentiated out as a constant when comparing the applied power to the conductivity.

Table 5-3 Top Temperature for each sample

Sample	Top Temperature (K)
Sample 1	4.8-5.9
Sample 2	13.0-15.5

Sample 3	5.1-7.7
Sample 4	8.9-10.1

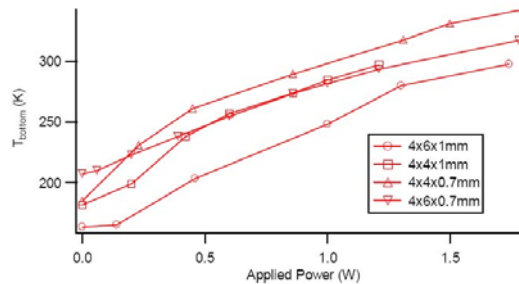


Figure 5-20 Bottom block temperature vs. applied power

To incorporate the supports into the design of the entire UCN source, it is important that the CAD models of the supports closely match their actual thermal and mechanical behavior. Finite element analysis (FEA) simulations were performed on models of the supports to calculate the heat flux across each sample when the steady state temperatures measured earlier were applied as boundary conditions. The heat fluxes could then be related to the conductivity and geometrical factors by means appropriate curve fitting and coefficient analysis. The SolidWorks[®] models used to fabricate the samples were the basis for the computational models, slightly modified to reduce the overall computation time. These modifications included minor changes such as removing mounting holes and thinning base plates, which would not affect the overall conductance of the sample. The SolidWorks[®] CosmosWorks[®] FEA package was used to perform these calculations, as it provided a seamless interface between the model design and calculation. The temperature

dependent thermal conductivity data for this alloy was taken from the NIST Database [58] and can be seen in Figure 5-20. This data was best fit by a third order polynomial shown in the equation below. This data was supplied to CosmosWorks[®] to calculate the necessary heat fluxes and temperature gradients.

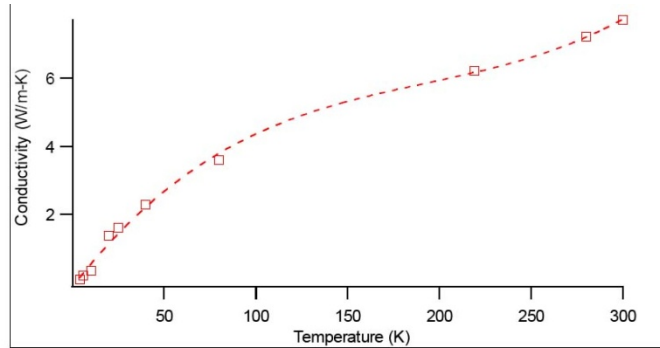


Figure 5-21 Conductivity Vs. Temperature for Ti6Al4V alloy
 $\kappa(T) = 5 \times 10^{-07} T^3 - 0.0003 T^2 + 0.065 T$

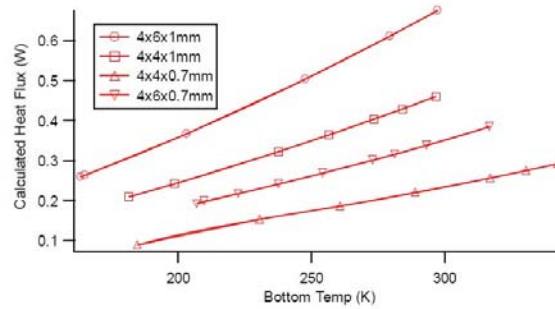


Figure 5-23 Heat flux results from CosmosWork

In an ideal setting, the system should reach a minimum in which no temperature gradient exists between the top and bottom of the sample. As apparent from the data, this was not the case, meaning that the system experienced some unexpected heat load or resistance to heat flow from the bottom block. A conservation equation to account for all heat entering and leaving the bottom block has been described below.

$$P_{\text{applied}} + P_{\text{radiation}} + P_{\text{wires}} = \frac{dH_{\text{block}}}{dt} + P_{\text{sample}} + P_{\text{resistance}}$$

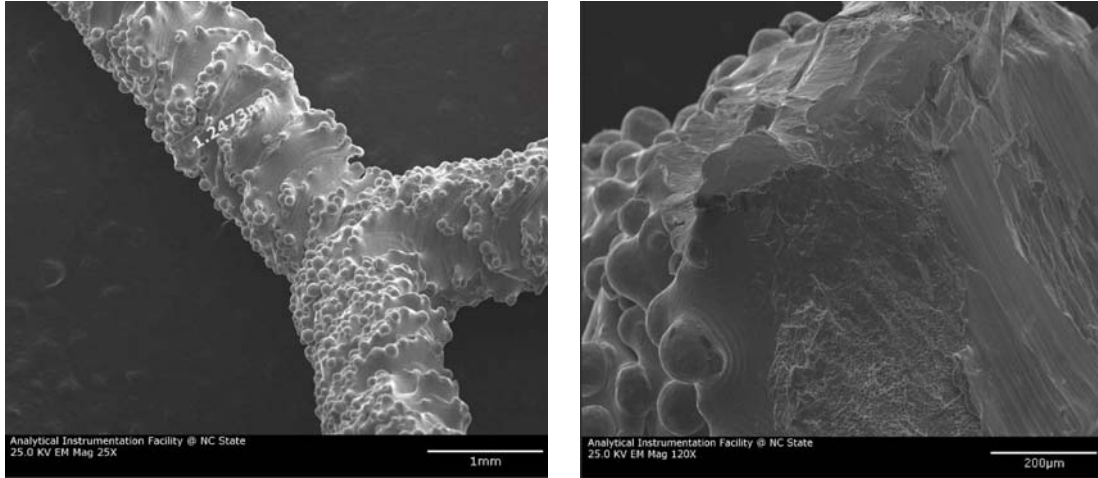
P_{applied} is the heat controlled by applied current to the heater in the block; $P_{\text{radiation}}$ is the absorbed (or emitted) black-body heat from the surrounding; P_{wires} is the heat conducted through the phosphor bronze leads connecting the temperature sensors and heater; dH/dt is the change in enthalpy of the aluminum in the block mentioned earlier. P_{sample} is the heat flux through the sample. $P_{\text{resistance}}$ is the resistance to heat flow at the interfaces of the sample, blocks, and cold head.

The low conductivity of phosphor bronze wires, combined with their small diameter and anchoring to the cold head means that P_{wires} is on the order of 1mW for all the wires combined; a relatively negligible amount. As described earlier, the maximum absorbed power by the block was 0.03W, and while small this would have an effect especially at low applied powers.

Accounting for $P_{radiation}$ proved to be much more difficult; because of the amount of oxidation on the blocks. An exact value for the emissivity of this unpolished aluminum alloy was not available. After data had been taken for all of the samples, an attempt was made to determine the emissivity by covering the blocks in thin Mylar tape of known emissivity, noted ϵ , of 0.01. Using Sample 4, the tape-covered bottom block reached a minimum temperature of 147K with no applied power, compared to 207K without the tape. From the Stefan-Boltzmann law, where the area of the block is $0.02m^2$ and σ is the Stefan-Boltzmann constant, it was found that 0.06W is absorbed by the blocks under steady state conditions.

$$P_{emis} = A\sigma\epsilon(T_{shield}^4 - T_{block}^4)$$

A heat load of 0.5W was then applied to the block, yielding a temperature of 191.8K. The amount of power needed to induce 207K in the bottom block was extrapolated using these two measurements and found to be 0.65W. For the block without tape, this temperature is induced by thermal radiation alone. Therefore we can again use Stefan-Boltzmann law to determine that the emissivity of the untapped block is 0.144.



a)

b)

Figure 5-24 Scanning Electron Micrographs of lattice structure reveal particles sintered to the lattice structures; this increases the effective surface area of the part.

Using this value for the emissivity, the relation between the total input power and temperature can be determined. Figure 5-25 shows the results of adding the input power, the radiation, and change in enthalpy of the block versus the bottom block temperature. A similar approach will be applied to determining the thermal conductivity and geometrical factor for the actual supports.

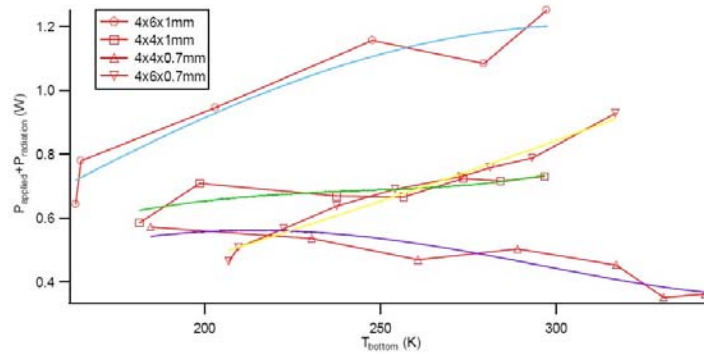


Figure 5-25 Total power Vs. Temperature with approximate curve fitting

The fact that Sample 1 has a calculated geometrical factor of less than half of Sample 2 shows that the contact resistance plays an important role in this experiment. This varies for each sample due to differences in contact pressure, exact coverage of the indium wire, sample contraction and other factors. To better quantify this, a second heat shield was made and attached to the cold head to vary the effect of radiation and to isolate the resistive effects.

Table 5-4 Observations on the effect of radiant heat

	Top(K)	Bottom (K)
No Mylar	9	207
Mylar Only	8.1	147
2nd Shield	25	168

Radiative Heating Only

	Top(K)	Bottom (K)
No Mylar	9	237
Mylar Only	8.1	191
2nd Shield	26	244

0.5W Applied Power

As can be seen from Table 5-4 the addition of a heat shield and mylar foil substantially reduced the heat absorbed due to radiant heat incident onto the test structure from the surface of the vacuum chamber.

5.5 Conclusion

It was determined that the smallest beam dimensions that can be fabricated without process optimization is approximately 0.7 mm in diameter. It is furthermore recommended that the strut angle relative to the horizontal build plane not be less than approximately 35° when using 0.7 mm diameter struts. At angles shallower than this, the connectivity between layers is low, and material properties are unacceptable.

A variety of cellular structures have been built in a variety of cell densities ranging from 5% to 11% that of solid Ti-6Al-4V. It was determined that adding solid skins to the tops and bottoms of these structures perpendicular to the expected loading direction dramatically improves material properties.

An interesting research area would be to develop an automated mesh design method to tune the properties of a mesh to a specific design problem. This would involve the exploring of different styles of unit cell structures and reconfiguring them to meet the application need. On the manufacturing side, parameters need to be developed to come up with more reliable mesh structures with complete melting while minimizing surface

roughness. Heat treatment and secondary surface finishing procedures can be explored to produce more reliable results.

Research in electronic and acoustic metamaterials was briefly discussed earlier. The current materials are limited to constant periodic structures. The three dimensional control offered by layered manufacturing can contribute to enhancing the properties that could be programmed into such materials.

The EBM process was used to demonstrate its ability to produce a structure with a negative Poisson's ratio (Figure 5-26). Conventional materials, when compressed in a direction tend to expand in other directions. These materials are said to have a positive Poisson's ratio. A mesh structure exhibiting a negative Poisson's ratio would compress in all directions upon compressive loading. The negative Poisson's structures were built to test their feasibility to provide support to the guide tubes used on the ultra cold neutron source being developed at the Nuclear engineering dept at NCSU. The part exhibited reduced strength based on the orientation of the beams with respect to the build plane and the beam's thin cross-section. Since the initial feasibility experiments, other researchers at NCSU have successfully built 3D negative Poisson's structures with a thicker beams.

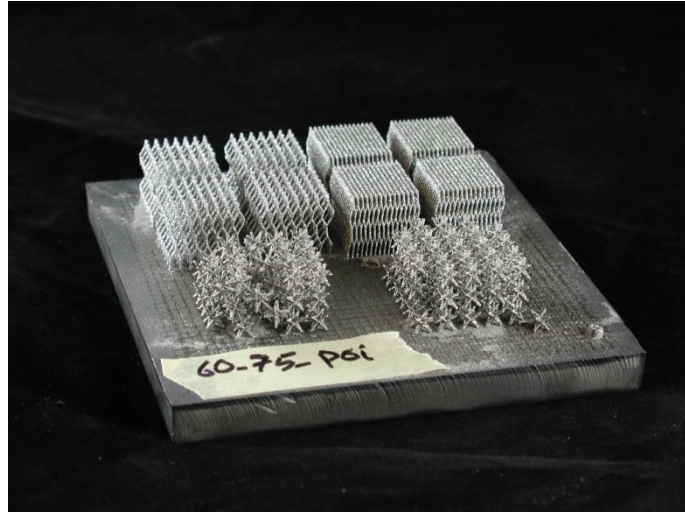
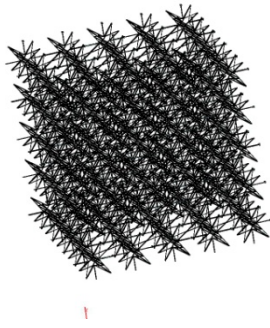


Figure 5-26 Negative Poisson's Ratio Materials Built On the EBM

The experimental setup for measuring thermal conductivity of the mesh samples under cryogenic conditions are currently being fine-tuned to reduce the effect of external radiant heat, thermal contraction of samples and more consistent contact between samples and the aluminum blocks.

Chapter 6 Other Materials Developed using the Arcam

EBM System

In addition to the material published as part of the thesis, there have been numerous material development efforts conducted as part of this research, including with aluminum alloys (7075 and 6061), high purity copper, lunar regolith simulant, copper-silicon carbide composite. This section will briefly discuss the issues related to the development of these alloys and their relationship with the development of a finite difference model for simulating the processing of such alloys.

New material development involves multiple issues such as internal stresses due to thermal gradients in the solidified material, grain structure and size within the processed part.

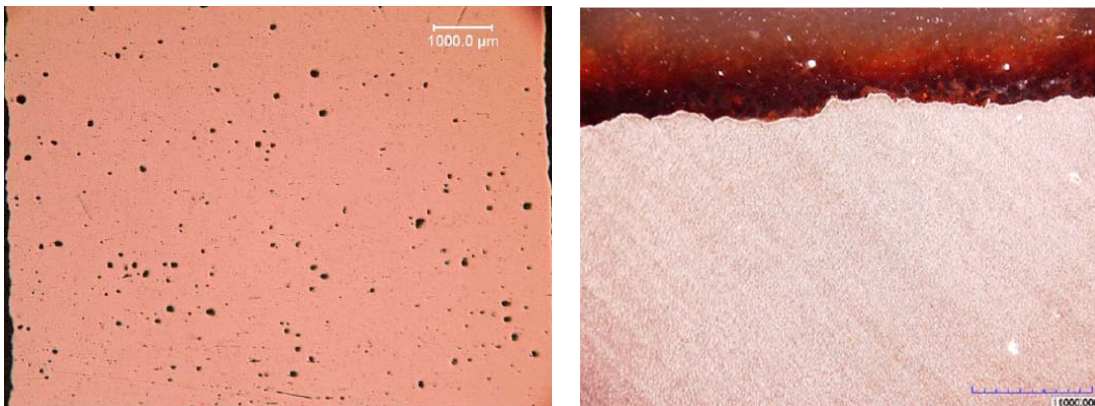
Large cracks in the EBM processed parts were sometimes observed when processing aluminum alloys such as 2024, 7075 and 6061 due large thermal expansion coefficients associated with Aluminum. Thermal cycling experienced by a part during fabrication can lead to cracking. This effect is even greater in parts involving high aspect ratios as the thermal gradients tend to be more non-uniform than those with a constant thermal gradient. The temperature and density maps plotted over time from a simulation model can be used to compute the stress-cycles within a part.

Table 6-1 Key physical properties of pure titanium, aluminum & copper

	Aluminum	Copper	Titanium
Coefficient of Thermal Expansion	23.1 $\mu\text{m}/\text{m}\cdot\text{K}$	16.5 $\mu\text{m}/\text{m}\cdot\text{K}$	8.6 $\mu\text{m}/\text{m}\cdot\text{K}$
Specific Heat	24.2 J/mol-K	24.44 J/mol-K	25.06 J/mol-K
Bulk Thermal Conductivity	237 W/m-K	401 W/m-K	21.9 W/m-K
Bulk Electrical Resistivity	28.2 n Ω .m	16.78 n Ω .m	420 n Ω .m
Density	2.7 gm/cm ³	8.94 gm/cm ³	4.56 gm/cm ³
Standard Atomic Weight	23.98 gm/mol	63.546gm/mol	47.867/mol

6.1.1 Copper

High purity copper was processed on the EBM with the purpose of making custom photoinjectors to be used in particle accelerators [114, 115]. One of the issues faced during processing was the presence of spherical pores/bubbles within a part. Based on the spherical pores, it was hypothesized that the pores occur not due to under melting but due to over melting (refer Fig. 6-1 (a)).



a)

b)

Figure 6-1 EBM processed pure copper

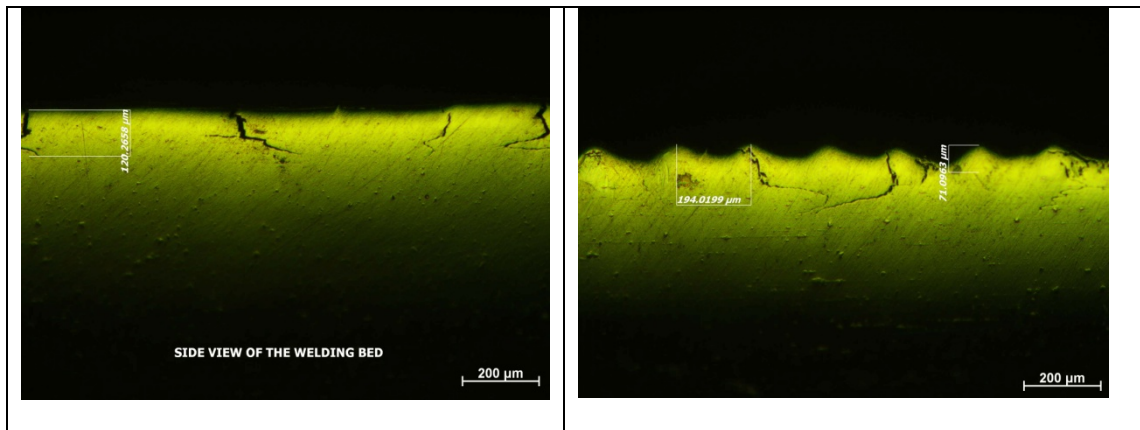
The copper melt pool needs to be elevated to a higher temperature in order to achieve a lower viscosity in the melt pool and to avoid cooling of melt pool due to high thermal conductivity of the material. However, adding excess energy to achieve lower viscosity can locally transform the material from a liquid to a vapor phase. It is hypothesized that the bubbles formed due to solidification of the melt before vapor could escape in vacuum (refer Figure 6-1(a)). The full density of EBM processed parts is critical to the functioning of the photoinjectors. Fine-tuning of the process parameters resulted in higher density parts as seen in Figure 6-1 (b). It needs to be understood that the processing parameters for these parts is specific to the geometry of the parts. Variations in the geometry could lead to higher porosity or incomplete fusion. Outputs from the finite difference model discussed in chapter seven can be integrated with operating pressures within a build chamber to suggest regions of higher presence of porosity within a copper part processed on the EBM.

Initial attempts have also been made to develop a silicon carbide copper matrix based composite for the development of a new electric discharge machining process. Copper and Silicon Carbide powders were mixed and added to the EBM hoppers. There is a substantial difference in the density, thermal conductivity, electrical conductivity and particle size between the copper and silicon carbide powders that were used. This led to

segregation of powder during powder spreading. The fabricated parts had bands or striations of copper and silicon carbide, rather than the uniform dispersion of silicon carbide that was desired. The distance between these bands was larger than the slice thickness defined during the generation of the SLC file.

6.1.2 7075 and 6061 Aluminum Alloys

Large cracks in the EBM processed parts were observed when processing aluminum alloys such as 2024, 7075 and 6061 due to large thermal expansion coefficients associated with aluminum. Thermal cycling experienced by a part being built leads to cracking. This effect is even greater in parts involving high aspect ratios as the thermal gradients tend to be less uniform than those with a constant thermal gradient. The temperature and density maps plotted over time from a simulation model could be used to compute the stress-cycles within a part.



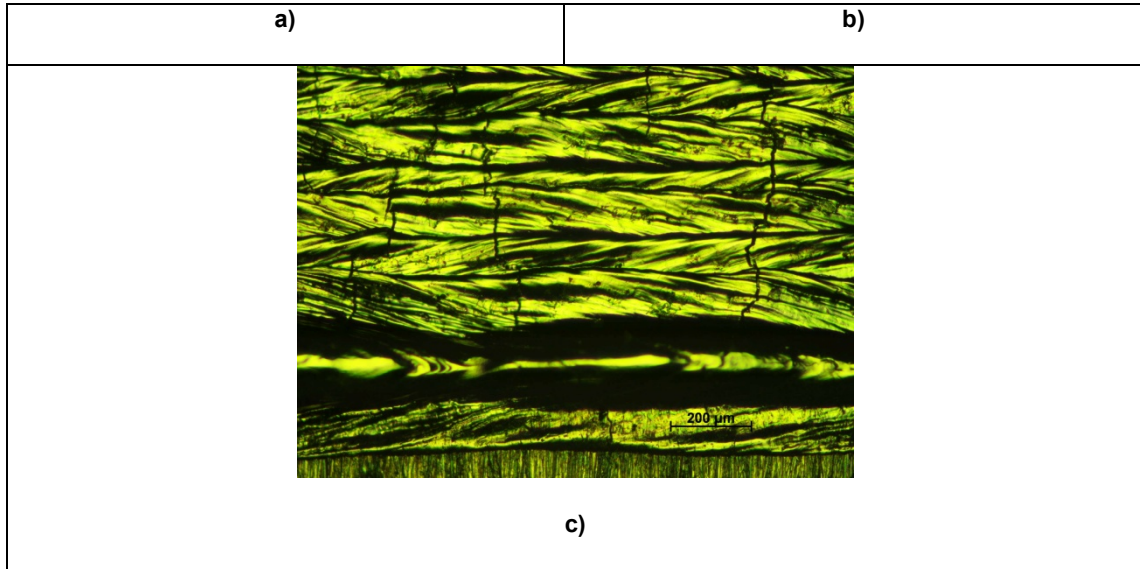


Figure 6-2 Cracks in EBM processed 7075 a) Micrograph taken parallel to the E-beam scan direction b) Micrograph taken perpendicular to the E-beam scan direction c) top-view of the sample

Alloys such as 7075 aluminum are widely used in the aerospace industry for high strength structural components. Of these, aluminum alloy 7075 generates the highest interest in the commercial sector. Magnesium and zinc play the role of the key alloying elements in this alloy. Magnesium is typically 2.1-2.9% and zinc is 5.1-6.1% of the overall composition, and they $MgZn_2$ precipitate in the alloy.

The challenges in processing of this alloy are twofold. The first issue is the development of parts with minimal porosity. The second issue relates to maintaining the composition of the finished part within the limits of the 7075 alloy. Maintaining composition is a concern as both zinc and magnesium vaporize in a range between 200-300°C, whereas the base aluminum metal melts around 660°C. To make things more challenging, the use of higher energy during melting helps in achieving high density. However, this is also the

cause of higher evaporation. Some of the samples processed on the EBM were analyzed in their bulk form using Inductively Coupled Argon Plasma Optical Emission Spectroscopy. The results are summarized in the table below.

Table 6-2 ICP analysis of EBM processed samples of Aluminum alloy 7075

Sample	Mg (%)	Zn(%)
1	1.04	1.22
2	1.17	1.23
3	0.93	0.90
4	0.77	0.85
5	1.12	1.27
6	0.77	0.85
7	1.13	0.97
8	1.06	0.87
9	1.18	0.80
10	0.49	0.33
11	0.57	0.57
12	0.59	0.55
13	0.89	0.92
14	0.98	0.99
15	1.17	1.22
16	0.98	1.23
17	0.78	0.88
18	1.03	1.42
19	1.60	2.22
20	1.81	2.46
21	1.37	1.58
22	1.08	1.15

As is obvious from this data, all melted samples exhibit heavy evaporation. The processing of 7075 revealed that the metal powder behaved in differently based on whether the powder was being scanned for preheating or melting.

There were some unique behaviors of the both the sintered and melted powder that was observed during the processing of 7075 powder. Excessive heating during the preheating

cycle leads to rapid but localized swelling of the powder particles. This has an appearance of the particles popping. Upon repeated processing, the powder seemed to further breaking apart from its generally homogenous grey form into segregated particles that were darker shades of grey (closer to black). The popping behavior was accelerated around the regions that were being melted. It was hypothesized that the popping occurred due to magnesium and zinc evaporating from the material. It was further hypothesized that the black powder that was getting segregated during the preheating operation was due to the slow movement of magnesium and zinc to the surface of the powder. A possible cause for this behavior is the solution treatment like behavior that the powder might be getting subjected to during preheating. This would lead to particle nucleation and grain growth of the $MgZn_2$ with the precipitate. In order to verify this hypothesis, batches of “Black” powder, “reused” powder, “Blobs” powder and depositions from the hood were evaluated using Energy Dispersive X-Ray Spectroscopy (EDS). A Hitachi S-3200 Scanning Electron Microscope was used to conduct this analysis (SEM). Please note that the interaction volume of SEM is limited to about 5 microns below the sample surface

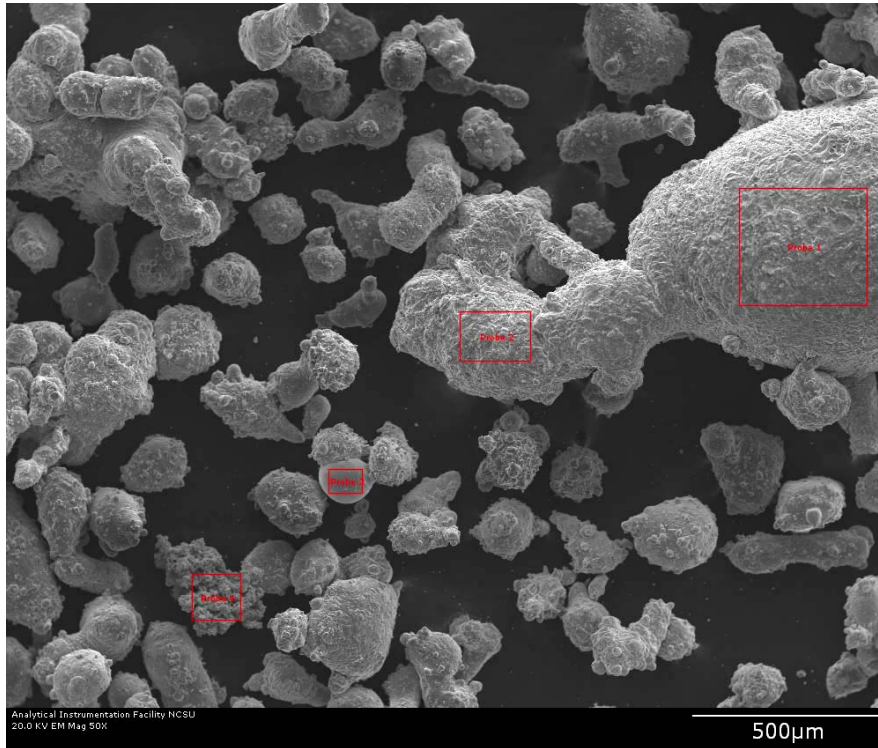


Figure 6-3 SEM image of “Black” 7075 aluminum alloy powder

Table 6-3 Summary of EDS results for “Black” 7075 aluminum alloy powder

Element	Probe 1 [wt%]	Probe 2 [wt%]	Probe 3 [wt%]	Probe 4 [wt%]
Mg	21.83	25.94	15.98	7.57
Zn	34.23	41.31	31.81	84.45
Al	32.60	20.00	42.29	7.79
O	11.34	11.07	9.92	0.18 ?
“?” Indicates elements for which proportion of total counts is statistically insignificant.				

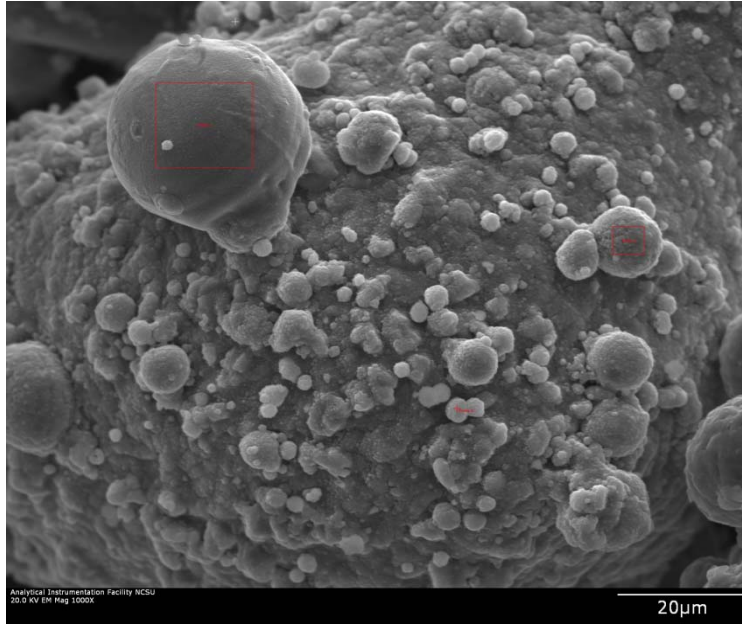


Figure 6-4 A closer look at a “Black” 7075 powder particle

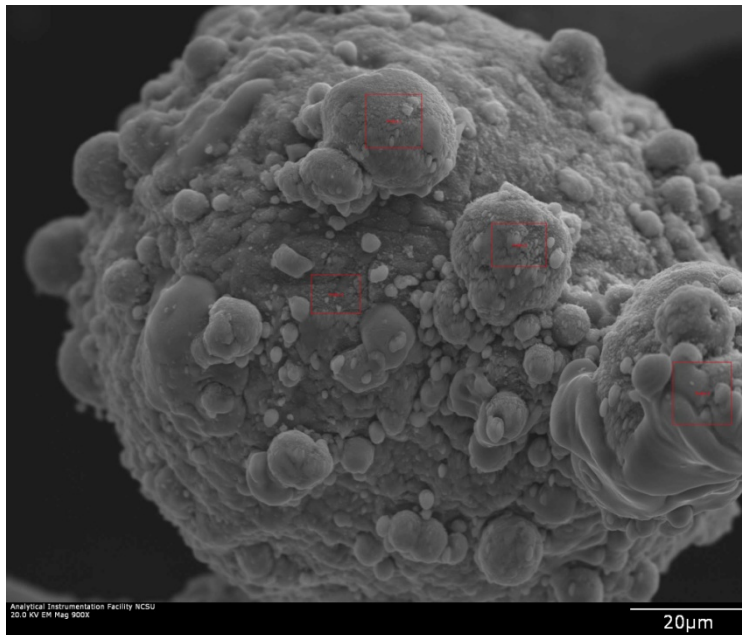


Figure 6-5 Aluminum alloy 7075 vapors deposited on the system hood

Table 6-4 EDS Analysis of sample from the hood

Element	Probe 1 [wt %]	Probe 2 [wt %]	Probe 3 [wt %]	Probe 4 [wt %]
Mg	10.8	15.25	11.96	9.01
Zn	15.05	24.48	25.99	10.15
Al	69.89	57.77	60.78	75.87
O	4.26	2.50	1.27	4.96
"?" Indicates elements for which proportion of total counts is statistically insignificant.				

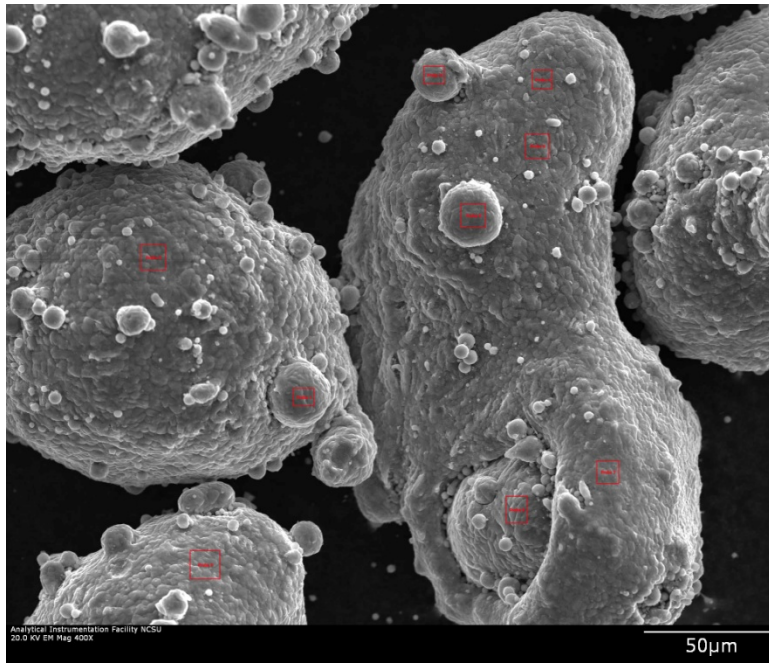
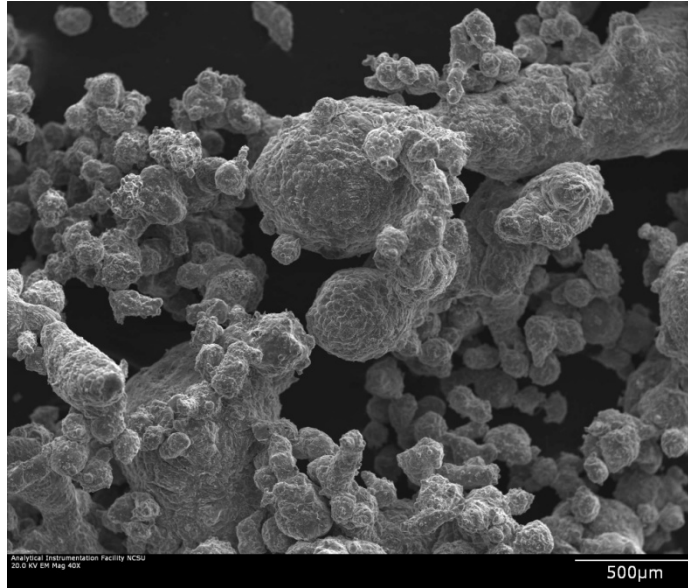


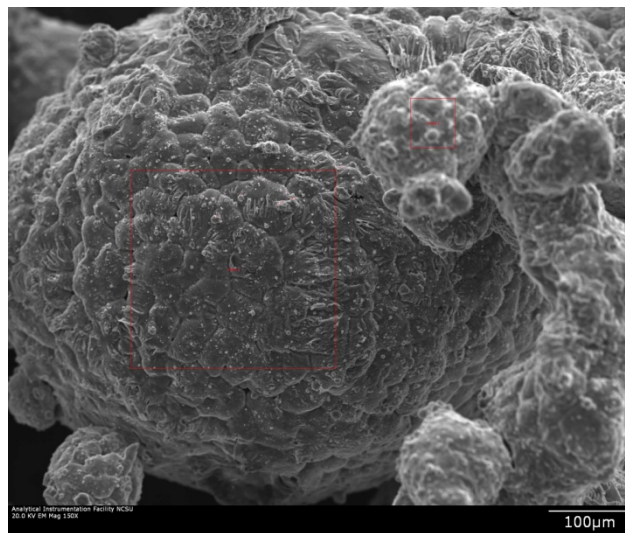
Figure 6-6 Reused 7075 alloy powder

Table 6-5 EDS results of reused 7075 alloy powder

Element	Probe 5 [wt %]	Probe 6 [wt %]	Probe 7 [wt %]	Probe 8 [wt %]	Probe 9 [wt %]
Mg	5.33	3.82	3.20	3.23	2.38
Zn	10.88	7.97	4.99	4.87	2.75
Al	79.27	84.07	89.71	89.56	94.24
O	5.32	4.15	2.11	2.35	0.63
"?" Indicates elements for which proportion of total counts is statistically insignificant.					



a)



b)

Figure 6-7 “Blobs” formed during the melting of 7075 alloy powder

Table 6-6 EDS analysis on the “Blobs” formed during the melting of 7075 alloy

Element	Probe 1 [wt%]	Probe 2 [wt%]
Mg	0.47?	1.63
Zn	0.14 ?	0.18 ?
Al	96.06	97.84
O	3.33	3.35
“?” Indicates elements for which proportion of total counts is statistically insignificant.		

As one can see from the figures and tables listed above. The black powder and vapor deposits on the hood have a higher concentration of magnesium and zinc, whereas the samples of powder from the blob region are almost completely depleted of magnesium and zinc. An unexpected result is the conservation of composition in the reused powder (figure 6-6 & table 6-5). Though the powder seems to be visibly changed in terms of shape and color in comparison to virgin powder, its composition seems to have remained unchanged. The degradation in the part quality when using reused powder has also been observed. It can only be concluded that the reuse of powder leads to migration of the alloying elements towards the surface of the powder. Upon heating, the alloying elements might then be evaporating and rapidly condensing, back onto the surface of the powder. It is also possible that the alloying elements are agglomerating within the powder as large sized precipitates. Repeated heating would make it easier for such large precipitates to evaporate the next time the beam is scanned over it.

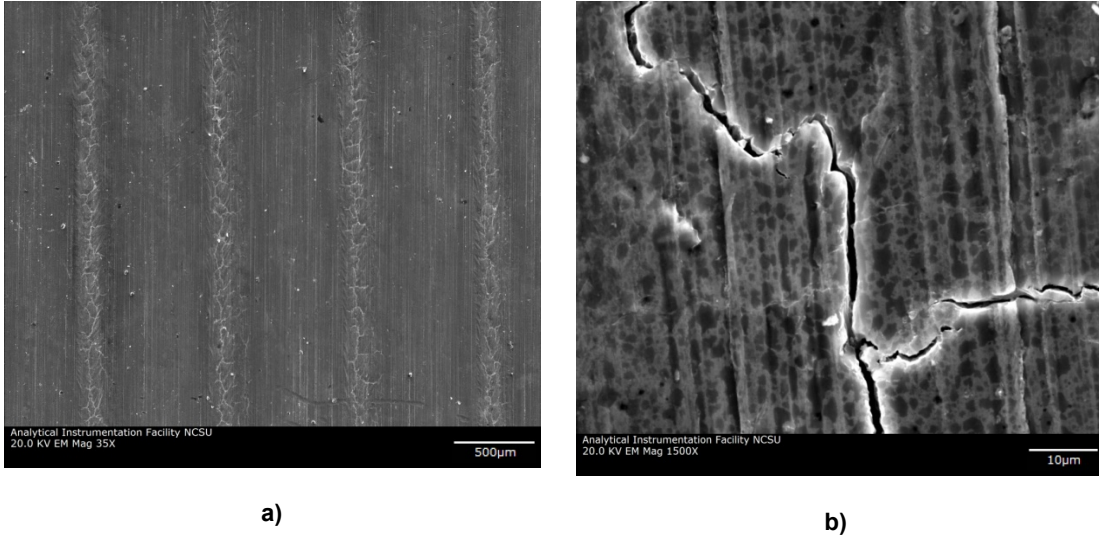


Figure 6-8 SEM images of E-Beam scans on a 7075 aluminum plate

Physical simulated scans were run over a purchased of wrought 7075 aluminum in order to evaluate evaporation without wasting any more virgin 7075 powder. Though the same parameters were used to scan over the powder, the evaporation was minimal. The difference between the two scenarios could be the higher thermal conductivity in aluminum due to its bulk form and absence of the cumulative effect of heating and melting layer upon layer of aluminum powder. A finite difference model similar to the one discussed later in chapter seven, would not only provide the capability to read such cumulative thermal effects, but it would also make it possible to couple the temperature data with the readings of the chamber pressure to estimate the local evaporation within the powder.

Multiple options are being evaluated to reduce evaporation while maintaining low porosity. It is possible to use metal powders in the EBM in either the mechanically alloyed form or pre-alloyed form. In the mechanically alloyed form, the elemental powders that make up the alloy are mixed using a high energy mechanical mixing set up (previously discussed in the chapter on titanium aluminide). This method for mixing alloying powder is feasible for alloys made up of metals of almost similar densities and equi-atomic composition as this maintains a uniform composition in cases where the powders are simply mixed. Pre-alloyed powders are formed by either creating an ingot in the alloy or melt in the alloy composition, which is later atomized to create the powder.

As can be seen from the figure 6-9, a mechanically alloyed powder can be non-uniform in composition and this could affect the properties of the end component. There is a higher chance of achieving uniform properties when using a prealloyed material due to uniform dispersion of $MgZn_2$ precipitate. Another option that was tried to retain the alloy composition was doubling the weight percentage of the alloying materials by either adding more alloying elements to the native 7075 powder by mechanical alloying or by using specially formulated high magnesium, high zinc pre-alloyed powder. In both cases, it was observed that processing of these high Mg, high Zn materials lead to more violent evaporation in the melt, thus resulting in a part that was non-compliant both in terms of porosity and composition.

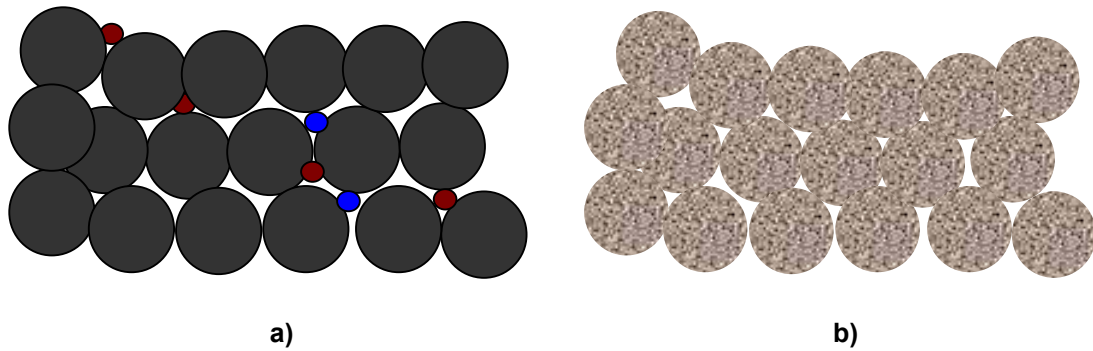


Figure 6-9 Comparison's between Mechanically Alloyed Powder & Pre-alloyed Powder of 7075 a) Mechanically Alloyed b) Prealloyed

Aluminum alloy 7075 is of high interest due to its application in the aerospace industry. Plans are to move a step away from the conventional methods used for processing materials with in the EBM system. Methods include

- Experimenting with powders with larger particle size. It is expected that the larger particle sizes might limit the evaporation to the surface of the particles.
- Operating the EBM at a higher pressure by bleeding helium into the vacuum chamber. The vaporization temperatures for metals are directly dependent on the pressures. The lower the pressure, the lower would be the evaporation temperature. Higher operating pressure also leads to more frequent arc trips within the electron beam gun. Operating pressures would need to be recommended under which the compositional integrity is maintained without excessive arc tripping

- Acceleration voltage applied on an electron beam defines the kinetic energy and hence the depth of penetration of an electron. Decreasing the acceleration voltage would also decrease the interaction volume between the electron beam and the 7075 particles, bringing the process closer to being a surface phenomenon. Heat transfer would thus be more reliant on conduction and convection than the violent elastic collisions of electrons with the atoms in the material.
- Defocusing of the electron beam will help in decreasing the energy density. Defocused beams are regularly used during electron beam melting to prevent smoking during the sintering cycles. This style of scanning redistribute the heat as well as the charge over a slightly larger area.

Basic feasibility tests have been performed on aluminum alloy 6061. The primary alloying elements in this alloy are silicon (0.4-0.8%) and magnesium (0.8-1.2%) but the percentage composition of these materials are relatively low. Initial trials resulted in parts that appeared dense. Fig.6-10 shows one such figure of a test part built in aluminum alloy 6061. A secondary phase was observed in the micrographs, which was assumed to be Si, Mg precipitate. Upon inspection with SEM, it was revealed that the secondary phase was actually an iron-aluminide intermetallic. These occurred due to the diffusion of iron from the steel start plate into the part. The iron aluminide precipitates were observed up to 15-20mm above the bottom of the test part. Repeated use of the same powder seemed to degrade the quality of the parts. EDS analysis was also conducted on the 6061 samples

produced via EBM melting but the composition of the alloys was too low to generate results that were statistically significant. Bulk material analysis techniques like ICP might be able to reveal the nature of the powder.

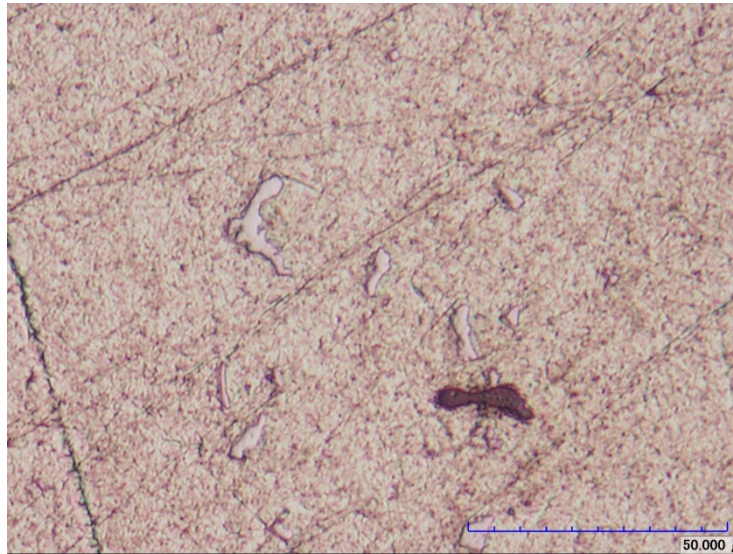


Figure 6-10 Optical micrograph of EBM processed 6061 with Fe-Al intermetallic.

6.1.3 Lunar Regolith Simulant

The vacuum based operating conditions and relatively low number of moving parts in the EBM process has made it an attractive material processing method to NASA for future missions. Lunar Regolith Simulant (JSC-1) was evaluated for its processing capability with the objective of evaluating it for NASA's (National Aeronautics and Space Administration) goal of establishing a lunar outpost. Lunar regolith primarily consists of metal oxides (refer table 6-7).

Table 6-7 Composition of JSC-1 lunar regolith simulant

Description	Composition	Weight %
Silicon DiOxide	SiO ₂	46.70
Aluminum Oxide	Al ₂ O ₃	24.40
Calcium Oxide	CaO	13.60
Magnesium Oxide	MgO	7.90
Iron Oxide	Fe ₂ O ₃	4.16
Sodium DiOxide	Na ₂ O	1.26
Potassium DiOxide	K ₂ O	0.08
Manganese DiOxide	MnO	0.07
Phosphorous Pentoxide	P ₂ O ₅	0.15
Titanium DiOxide	TiO ₂	0.41

Actual lunar soil consists of nanophases Fe⁰ particles embedded within silicates due to micro meteor collisions on the lunar surface. The presence of nanophase Fe makes it possible to sinter actual lunar soil in the mare region of the moon using microwave sintering [116]. The same feat cannot be achieved using any of the commercial stimulant materials due to the lack of pure nanophase iron. Microwave sintering of lunar soil is being investigated for the in-situ resources utilization for extraction of oxygen and hydrogen as well as construction of lunar roads.

There has been limited work in the field of freeform fabrication with lunar soil. Direct processing of lunar regolith to form large parts using EBM processing is difficult due to

low electrical conductivity of this material. As an alternative, lunar regolith was suspended in an aluminum matrix. Aluminum was selected as the matrix material due to its low density and high electrical conductivity.

The objective of the research was to maximize the utilization of the JSC-1 simulant in the metal-ceramic composite to be processed on the EBM. The feasibility tests were carried out by spreading a single layer of the regolith-aluminum mixtures on top of a start plate. The mixtures were first mixed using high-energy ball milling (figure 6-11). The ball milling of the powder helped in the dissipation of electrical charge accumulated by the simulant in during EBM processing.

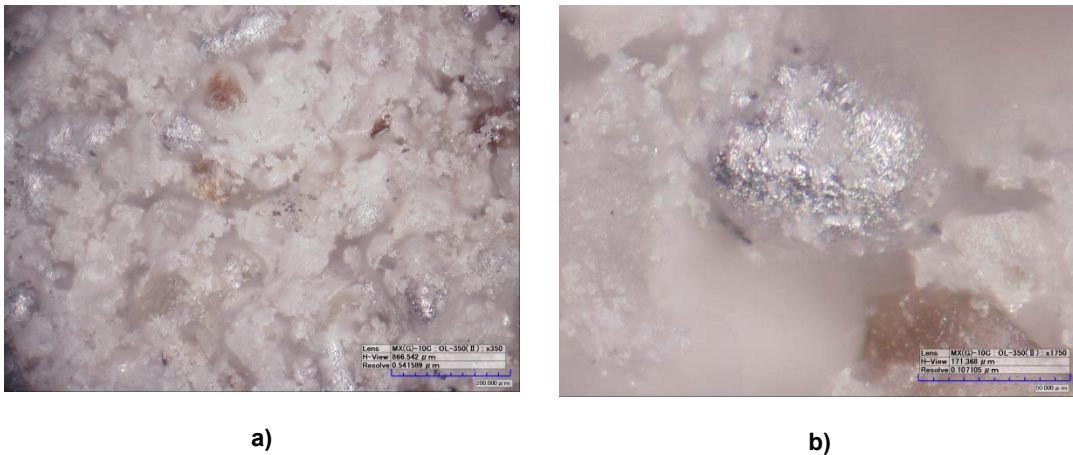


Figure 6-11 Ball milled aluminum regolith mixture with 20% aluminum loading.

The single layer of regolith was gradually heated with sub-milliamp current at 60KV acceleration voltage. The regions that were being heated by the electron beam were considered thermally isolated from the surrounding, that is, there were no conductive or

radiant heat losses. The amount of energy necessary for heating and sintering the samples was calculated by evaluating the weight of pure aluminum within a layer of the evaluated the sample. The incident energy was set such that the pure aluminum would be heated to the point of sintering. It was assumed that the pure regolith stimulant did not absorb any of the incident energy. This idea was tested by calculating the necessary incident energy to sinter a pure aluminum sample and testing those settings on the EBM. As can be seen from Figure 6-12, sintering was observed..

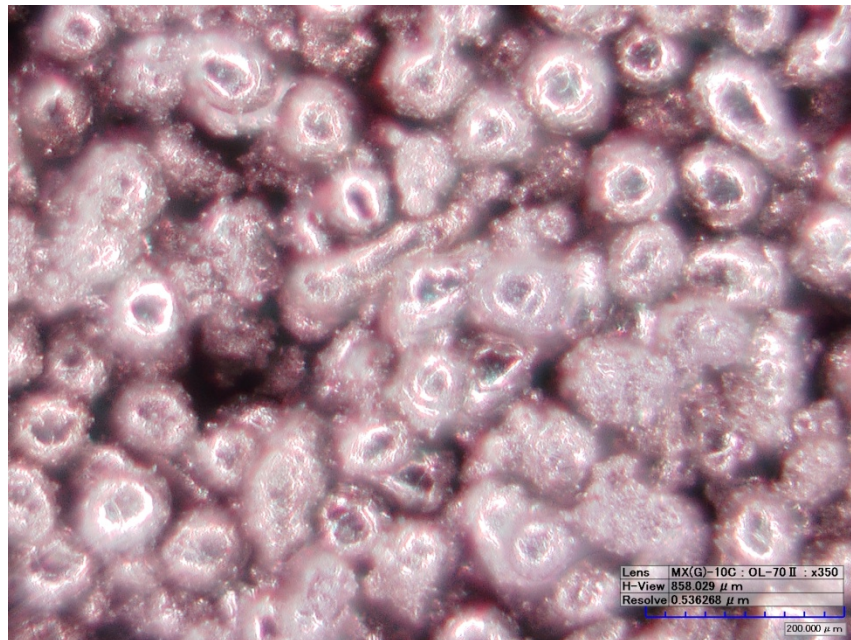


Figure 6-12 Sintering of a single layer of pure aluminum via low current heating

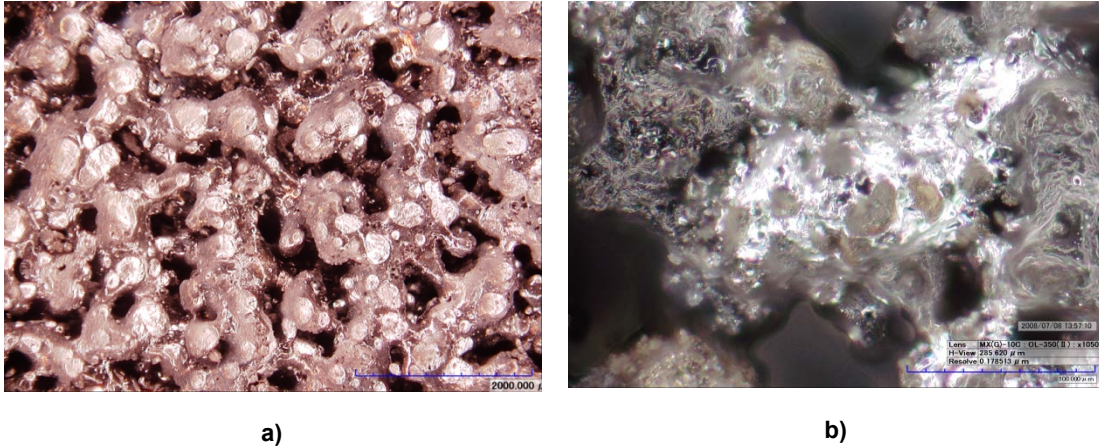


Figure 6-13 EBM processed JSC-1 lunar regolith simulant with 50% aluminum melted at 60KV acceleration voltage a) Top surface of EBM processed part b) Close up revealing regolith embedded in aluminum matrix

Heating was carried out on the mixed regolith aluminum samples using a highly defocused beam and a sintering based scanning method in order to reduce the effect of particle charging leading to smoking. The weight composition of aluminum was varied between 5-50%. The processing of the samples was stable at 60KV acceleration voltage when the composition of aluminum was more than 20% in the stimulant mixture. Fig.6-13 shows regolith samples with 50% aluminum composition processed at 60KV acceleration voltage. It was difficult to process the mechanically alloyed regolith beyond about 30 layers due to its inability to flow freely. The behavior of the simple ball milled sample seems highly hygroscopic whereas high energy mechanical alloying has resulted in regolith with better flow properties. It needs to be studied if the hygroscopic behavior is due to water absorption or due the interaction between the iron oxide particles.

Lower acceleration voltages of 15KV, 30KV, 50KV were tried for samples with lower aluminum loading. The lower acceleration voltage decreased the velocity and penetration depth of the incident electrons. This decreased the chances of the charging and smoking during the processing.

An attempt was made to process pure regolith by operating the electron beam gun with a 15KV acceleration voltage. It was possible to sinter the pure regolith using such low acceleration voltage but the samples eventually smoked within 10 layers of processing. Figure 6-14 shows a sintered sample consisting 100% of lunar regolith stimulant.



Figure 6-14 100% JSC-1 Lunar regolith stimulant fixture sintered using the EBM process.

The EBM processing of the regolith may generate a caustic byproduct based purely on the smell emitted by the vacuum system. Oxygen and water extraction from lunar regolith has been demonstrated by heating the regolith with carbon or in the presence of hydrogen. Liberation of hydrogen or oxygen during EBM processing would definitely be

of interest to NASA and this study would be part of any future studies along with the evaluation of any changes in the composition of the processed samples.

The current model for evaluating melting does not account for the complex metal matrix-ceramic nature of the system. The metal matrix has higher thermal and electrical conductivity but the regolith component of the system has higher specific heat and lower conductivity. There is a definite need to develop a simulation model of particle charging within for this material in order to develop methods to reduce smoking. The generalization of the regolith-aluminum powder as a homogeneous entity might not be effective for the thermal simulation model. A more effective model might need to approximate the packing of aluminum and regolith within the voxels.

Chapter 7 Modeling the Electron Beam Melting Process

In order to understand the working of the electron beam system, it is necessary to understand the interaction between the electron beam and the substrate (in this case metal powder).

The electron beam gun accelerates the electrons liberated by the cathode by applying an accelerating voltage, V_{acc} . This voltage defines the velocity, v_e , of an electron with mass m_e and charge e ; where

$$\frac{1}{2}m_e v_e^2 = V_{acc} \times e$$

$$m_e = 9.109 \times 10^{-31} \text{ Kg}$$

$$e = -1.602 \times 10^{-19} \text{ C}$$

$$V_{acc} = 60,000\text{V (most commonly used accelerating voltage on the EBM)}$$

The expected velocity of the electrons for this system would therefore be approximately 1.453×10^8 m/s (approximately, half the speed of light).

Once these electrons hit the specimen, they either bounce back (elastic interactions) like a rubber ball with no loss of energy, or, they begin to lose energy (inelastic interactions) as they penetrate deeper into the specimen (see Figure 7-1). The electrons that bounce

back without loss of any energy are called backscattered electrons. The electrons that penetrate into the specimen collide with other atoms, and some electrons from the outer orbitals of these atoms are liberated. These electrons are called secondary electrons. Similar to the secondary electrons, the liberation of electrons from the inner orbitals gives rise to X-rays, but those interactions are not considered here. The electrostatic interactions between the outer orbit electrons and the accelerated electrons, also lead to the changes in the trajectory of the secondary electron. This leads to the spread of energy over a region larger than the beam diameter. What is of importance for this analysis is the component of energy that is backscattered by the specimen ξ_{back} . The component that is absorbed by the system can be called γ_{abs} ; where ($\gamma_{\text{abs}} = 1 - \xi_{\text{back}}$).

The Bethe equation [117] defines the energy loss per unit distance traveled by the electron and is given by

$$dE/dx = [(-2\pi e^4 N_o Z \rho) / (A E_M)] * \ln(1.166 E_M / J) \text{ (KeV/cm)}$$

where,

ρ = density of the substrate (g/cm³)

E_M = Mean electron energy (KeV)

N_o = Avogadro's number = 6.022x10²³

J = mean ionization potential (KeV)

Z = Atomic number of the substrate

E = charge on a single electron (C)

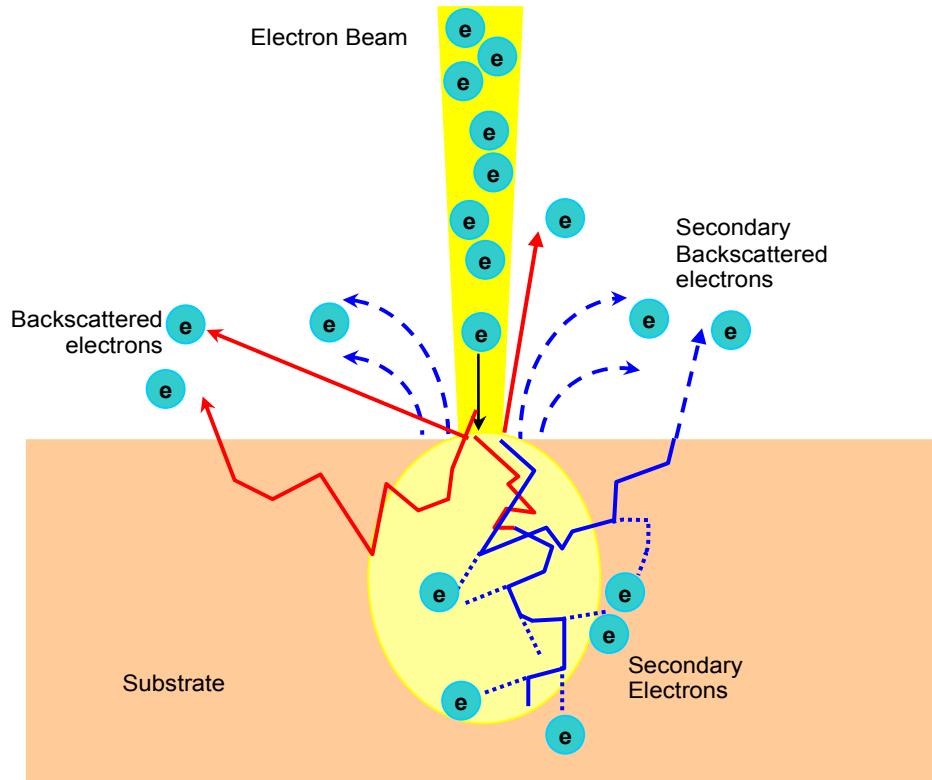


Figure 7-1 Electron beam interaction with substrate

The mean ionization potential is the average energy loss per interaction considering all possible energy loss processes and is given by

$$J = (9.76 * Z + 58.5 * Z^{-0.19}) \times 10^{-3} \text{ KeV}$$

It is also approximated as $J \approx 0.115 * Z$ and we can approximate E_M as

$$E_M = e * V_{acc}$$

The Bethe range is calculated from the above formula as the distance traveled by an average electron before it loses its energy.

$$R = \int_{E=E_0}^{E=0} \frac{1}{dE/dx} dE$$

The Kanaya-Okayama range approximates the depth of scattering over a flat surface as

$$R_{KO} = \frac{0.0276 A E_0^{1.67}}{Z^{0.889} \rho} \text{ (microns)}$$

7.1 Understanding Electron Beam Layered Manufacturing

One of the aims of this body of work is to develop tools that will aid in developing new materials using the Arcam EBM system. Based on the experience gained so far from operating the electron beam melting system, the problem can be narrowed down to two separate endeavors:

- Developing threshold parameters for preventing particle charging (i.e., “smoke”) from occurring during the processing of a part
- Assure a sufficient degree of melting or sintering required to process a specific layer

It would thus be necessary to sequentially develop these process parameters for each stage of layer processing; namely preheating, support powder sintering and melting.

Prior to melting the first layer of a part, the start plate is preheated to an elevated temperature. The preheating of the plate serves multiple purposes :

- Decrease the amount of heat required to melt the powder for the first few layers.
- Minimize the thermal gradients in the first few layers of the build.
- Aid the welding of the part to the start plate. A loosely welded part can ruin an entire build due to swaying or the parts uprooting during the build.

The start plate preheating temperature can be considered to be another variable. As a rule of thumb, efforts have been made to use a plate heating temperature that lies somewhere between the solidus and liquidus temperatures of that alloy. This start plate initial temperature will be called T_{sp} . Increasing this value can cause excess fusing of loose metal powder to the plate; a problem that can be solved by elevating the parts on stilts. Using a low T_{sp} generally leads to unwanted powder charging during the preheating cycle.

The temperature of the plate is measured using a thermocouple attached to the bottom of the plate (plate thickness = 15mm). This leads to latency in the readings of the surface temperature of the plate.

7.1.1 Causes of “Smoke”

Smoke can be described as a cloud of metal powder generated due to the electrostatic interaction between the electron beam and the metal powder on the build plane.

There are two separate scenarios under which smoke is observed, namely during raster (Type I) and vector scans (Type II)

Type I Smoke

Type I smoke occurs when the system is raster scanning over a hatch pattern (Figure 7-2). Once the beam completes a vector scan it moves back to scan the second vector, separated from the first by a distance d_{LO} .

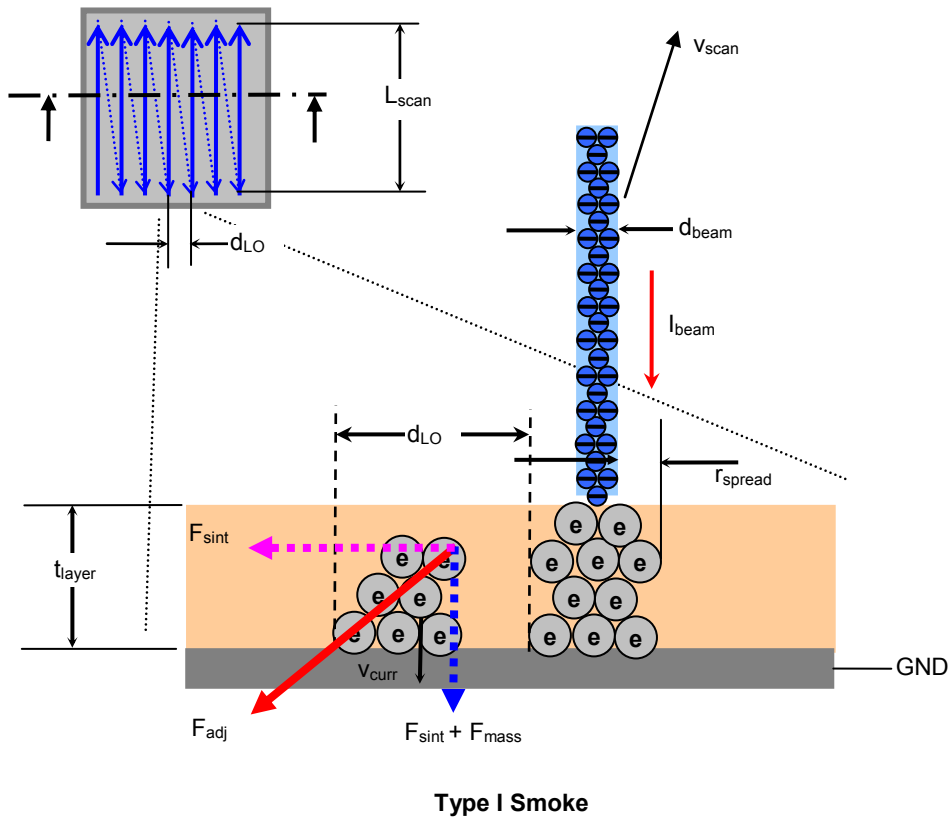


Figure 7-2 Type I particle charging

During the beam scan, the powder experiences electrostatic repulsion caused by charges on the previously scanned area. Smoke is caused if the forces of repulsion are greater than binding forces on the powder. The binding force consists of tensile strength of the sintered powder (or stiction) and the weight of the particles. Under ideal circumstances, it would be preferred that all the electrons from the previous vector scan have migrated into the solid material.

For a scan length L_{scan} , the time required for the beam with a beam diameter of d_{beam} to scan that length is given by :

$$t_{\text{scan}} = (L_{\text{scan}} - d_{\text{beam}}) / v_{\text{scan}} \text{ (sec)}$$

Upon entering the substrate, the electrons spread around as shown seen in simulations later in this chapter. Let us call this radial spread r_{spread} and assume the following

- $(d_{\text{beam}} + 2r_{\text{spread}})$ = circular spread of the electrons after entering the sample (current is limited to this diameter).
- ρ_{rel} = relative density of the powder with respect to the bulk density of the material ρ ; where $(0 < \rho_{\text{rel}} < 1)$.
- Z' = atomic weight of the material
- n = number of free electrons available in an atom/molecule of the substrate material
- v_{curr} = drift velocity of the electrons in the substrate.

- t_{layer} = layer thickness of the loose powder.
- A' = a coefficient dependent on the contact area between powder particles (would be a function of powder size, shape factor, packing and extent of sintering).

By the time the beam traverses a small distance of Δx , it has deposited $I_{\text{scan}} * \gamma_{\text{abs}} * \Delta x / v_{\text{scan}}$ coulombs into the substrate over an area (assuming uniform surface current density)

$$A = \Delta x (2r_{\text{spread}} + d_{\text{beam}}) + \pi (r_{\text{spread}} + d/2)^2$$

And $A' = A_{\text{min}}/A$; where A_{min} is the minimum cross section area created due to necking between the sintered particles.

The drift velocity of the electrons traveling through the substrate can be approximated to be

$$v_{\text{curr}} = \frac{I * \gamma_{\text{abs}} * Z'}{A * A' * N_o * \rho * \rho_{\text{rel}} * n * e} \text{ (cm/s)}$$

The time required by these electrons to travel through the thickness of the powder is $t_{\text{layer}}/v_{\text{curr}}$. So if $t_{\text{layer}}/v_{\text{curr}} < L_{\text{scan}}/v_{\text{scan}}$, it can be assumed that the possibility of smoke is minimized. This strategy would slightly change in case of overhanging surfaces supported by sintered supports, where the electrons need to travel a distance much larger than t_{layer} through the sintered supports.

In case $t_{\text{layer}}/v_{\text{curr}} > L_{\text{scan}}/v_{\text{scan}}$ there would be a residual charge on the powder during the scanning of an adjacent vector scan (lets call this scan 2). Electrostatic forces would act

on the powder due to the interactions between the residual charges, q and the beam hitting the surface on the adjacent scan with a charge density of λ C/m can. Assume the beam is cylindrical with a length of L . We can approximate the force acting on the adjacent scan with residual charge q using Gauss's Law:

$$F_{adj} = \frac{1}{4\pi\epsilon_0} \int_0^L \frac{q\lambda}{(d_{LO}^2 + x^2)} \frac{(\vec{d}_{LO} + \vec{x})}{|\vec{d}_{LO} + \vec{x}|} dx$$

The movement of the particles from the previous scan is opposed by their mass (F_{mass}) and the strength of sintering of the particles (F_{sint}).

Type II Smoke

This type of smoke is observed immediately after the beginning of a vector scan (it can occur both during contour and hatch scanning). The qualitative explanation for this phenomenon is as follows. At slow scan speeds a large amount of charge builds up for a given cross sectional area. For the sake of convenience, let's assume that the beam is pulsing at equal ON and OFF intervals of infinitesimally small amount of time Δt . The value of Δt could be dictated by the frequency with which electrons pass through the trailing region of the beam (thus the beam current).

Due to the small value of $v_{scan}\Delta t$ it can be assumed that the majority component of the force due to the interaction between the powder and the beam would be vertical. In order to prevent smoke, this component would need to be balanced by F_{mass} & F_{sint} .

Another way of looking into the occurrence of smoke during the electron beam scanning of vectors would be to look into the internal forces developed in a scanned region. As the beam scans over a region of powder; charge accumulates in the powder. This charge should cause the particles to strongly repel but they are held in place due to the sintering of the powder and the weight of the powder particles them self. In metal powder, the charge migration occurs on the surface of the particles (Gauss's Law[118]) and hence the electrostatic force acting on the particles is dependent on the nature of packing of the particles (and hence the particle geometry).

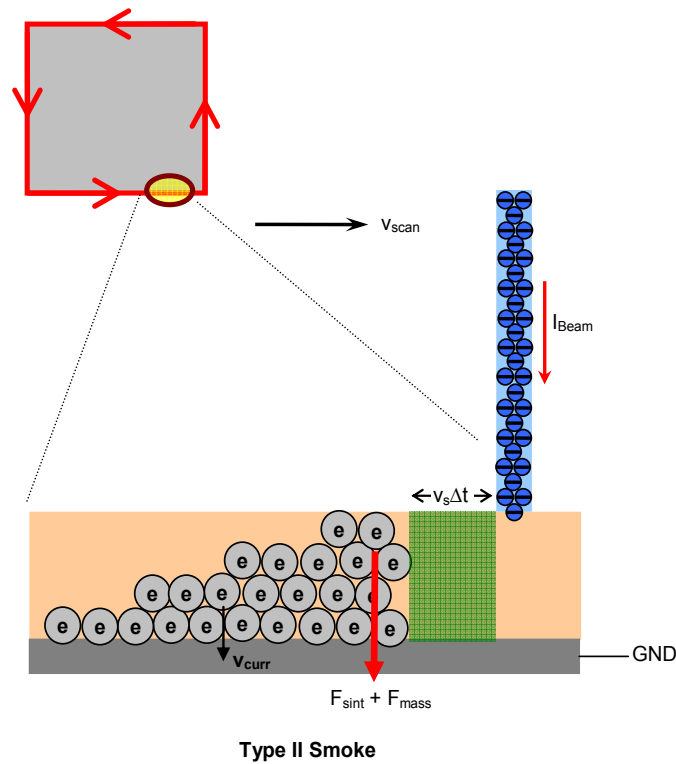


Figure 7-3 Type II particle charging

7.1.2 Melting cycles

The beam power that is not backscattered can be given as

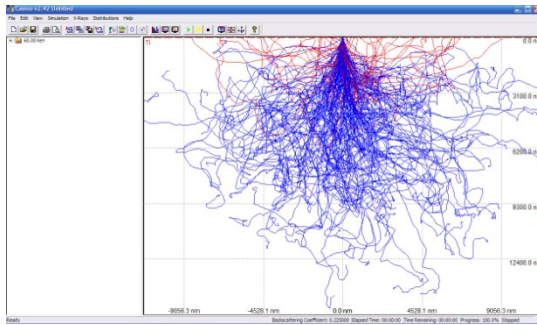
$$P = V_{\text{acc}} * I_{\text{scan}} * \gamma_{\text{abs}}$$

Let d'_{beam} represent the diameter over which the beam energy is spread where

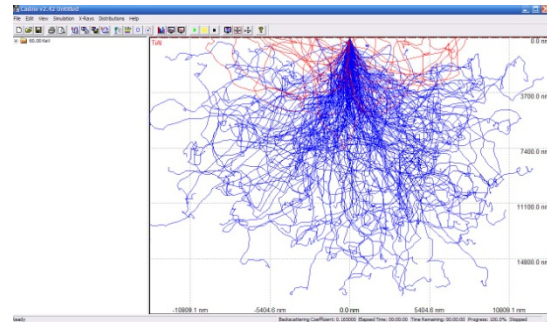
$$d'_{\text{beam}} = d_{\text{beam}} + 2r_{\text{spread}}$$

The values for r_{spread} and γ_{abs} can be determined using a Monte Carlo simulator for electron beams (Figure 7-4) [119].

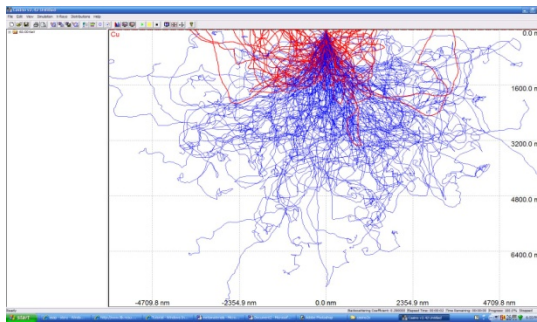
Since the value of d_{beam} is very small, the majority of the beam's energy is concentrated into a small region with very low energy loss during the exposure time of $d'_{\text{beam}}/v_{\text{scan}}$. The energy is then slowly transferred to the surrounding material by thermal diffusion.



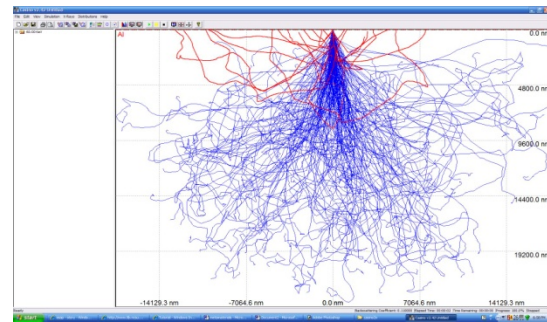
Titanium



Titanium Aluminide



Copper



Aluminum

Figure 7-4 Monte Carlo simulations of beam & substrate interactions[119]

The energy density over a unit cross section [120] is given by

$$Q = \frac{\pi P}{4d'_{beam} v_{scan}}$$

Since the distance between two scans is d_{LO} , the energy density per unit volume can be expressed as

$$\bar{Q} = \frac{\pi P}{4v_{scan} d_{LO} t_{layer}}$$

We shall ignore the case of energy distribution of two parallel scans overlapping one another as $d_{LO} \gg d_{beam}$

The heating of the above discussed region causes the rapid heating of the particles up to their melting point and causing the particles to bond without total melting of the powder. Call this the sintering temperature T_{sint} . The process parameters required to achieve this can be given as

$$T_{sint} = T_{sp} + \frac{1}{C} \left[\left(\frac{\pi}{4\rho_{rel}} \right) \left(\frac{P}{v_{scan} d_{LO} t_{layer}} \right) - \Delta H \right]$$

where

C = Heat Capacity (J/Kg.K)

ΔH = Latent heat of fusion

Note that the units need to be standardized and applied to the above formula.

Parameters for melting the material can be decided upon by eliminating the ΔH term.

Void fractions (porosity) in the sample as expressed as α with boundary conditions $\alpha_s \geq \alpha \geq \alpha_p$; where α_s is the void fraction in a solid part and α_p is the void fraction in free flowing powder. The densification in a given sample can be expressed as

$$D = \frac{\alpha - \alpha_s}{\alpha_s - \alpha_p}$$

It can be approximated that for sintering rate k' , the densification rate of the sample can be expressed as

$$\frac{\partial \alpha}{\partial t} = -k' \alpha$$

The extent of densification in the powder would have a direct effect on the occurrence of smoke that is encountered during the processing of the powder. The 2D example in Figure 7-5 illustrates this hypothesis.

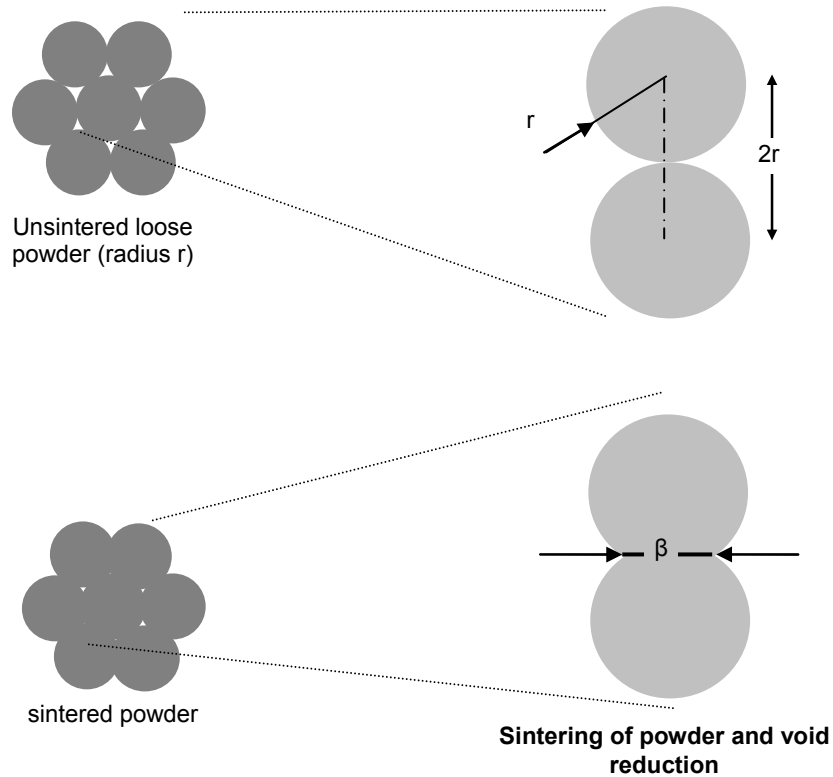


Figure 7-5 Influence of powder density on charging

The void fraction for this example is given by

$$\alpha = \frac{2}{\sqrt{3}} \left[\frac{\pi r^2 - 6 \left\{ \frac{r^2}{2} \cos^{-1} \left(\frac{\beta}{2r} \right) - \frac{3}{2} \beta \sqrt{4r^2 - \beta^2} \right\}}{4r^2 - \beta^2} \right]$$

The value of β would contribute to the value of the drift velocity in the form of increased effective cross sectional area. This added cross-sectional area would also increase the fracture force that the powder cake can withstand. This would mean an increase in F_{sint} .

The problem is determining level of sintering as most of the times the powder is too fragile for conducting any observations that would require handling of the powder cakes. An alternative to this is measuring the conductivity of a cake of powder held between two flat plate electrodes. The resistance of the sample along with its bulk resistivity and particle size could be used as a qualitative measure of the extent of sintering.

The table below shows a qualitative comparison between the ease of melting a powder and its bulk, resistivity and density (higher weight provides resistance for the particles from rising above the build plane). This table is based on experiments with a variety of powders.

Table 7-1 Electrical and physical properties of EBM materials

Material	Density	Bulk Resistivity	Density/ Resistivity	Ease to EBM
TiAl	3.91g/cc	1.0 $\mu\Omega\text{m}$	3.91	Very Difficult
Titanium	4.43	0.42 $\mu\Omega\text{m}$	10.52	Difficult
Aluminum	2.78	26.5n Ωm	104.9	Easy
Copper	8.96g/cc	16.78n Ωm	533.96	Very easy

In the experiments conducted to date, only titanium alloys had considerable smoking issues due to their higher density to resistivity ratios. It has been decided to currently focus the simulation models on the thermal model and evaluate an alloys ability to smoke during EBM processing on the ratio of bulk density to resistivity of the alloy.

As previously discussed the analysis of any direct metal freeform fabrication process varies from that of simulations of focused energy beam welding methods. Typical focused energy beam based welding techniques are limited to a single welding pass meant to weld two metals of uniform conductivity together.

Three dimensional layer fabrication processes are based on sequential deposition of layers of materials to form a 3D part. Varying heating parameters are used for the deposition of such layers as the areas within a layer can be segregated as preheating, support materials, melting and post melting. This study shall stay more focused on the Electron Beam Melting (EBM) Process by Arcam AB. As described earlier, this process involves the deposition of a layer of powdered metal that is selectively melted in order to generate the cross-section of a layer. Within a layer, a large area typically corresponding to the geometry of the start plate is heated prior to melting (this shall be referred to as preheat-I). This is carried out in order to minimize thermal gradients and eventually the internal stresses within a part. Blocks of materials are sintered using a scanning routine typically referred to as volume sintering. Melting routines can be divided into parameters for the mesh structures involving thin cross-sections and the ones for melting cross-sections that are larger than two beam scans wide.

Conventional processing in the EBM uses very high scan speeds during the preheat-I & volume sintering scans. These speeds are typically between 5,000 mm/sec-10,000 mm/sec. The scanning styles are also a modified version of typical raster scanning in

order to achieve uniform heating across the surface. The scanning speeds used for melting follow an S-shaped raster pattern defined by distance between two adjoining scan lines.

As previously discussed, electron beam interaction with any material is accompanied by energy loss in the form of elastic backscattered electrons. The amount of energy lost through back scattering is not just dependent on the atomic number of the substrate material, but, it is also dependent on the angle at which the electron beam hits the substrate[117].

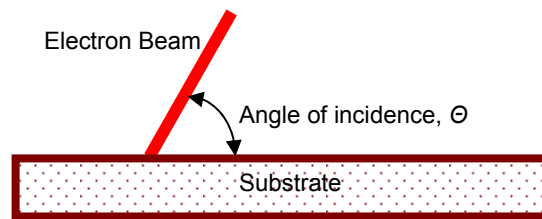
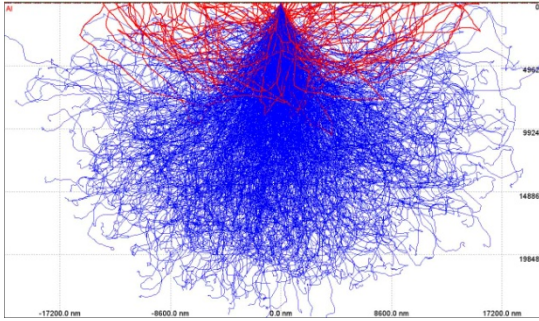


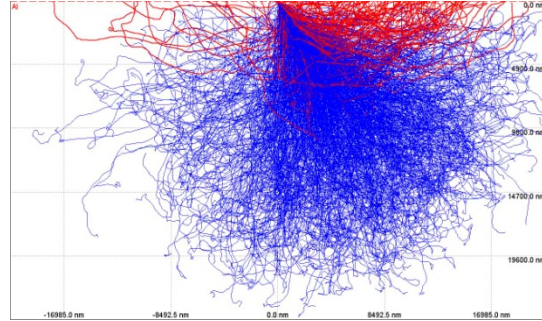
Figure 7-6 Angle of incidence of an electron beam

The figure below illustrates the variation in the amount of backscattering as a function of the incident beam angle. The images are generated using a Monte Carlo Simulation (CASINO V2.42) of the Electron Beam Interaction with a block of pure Aluminum. The incident electrons were modeled with energy of 60KeV.



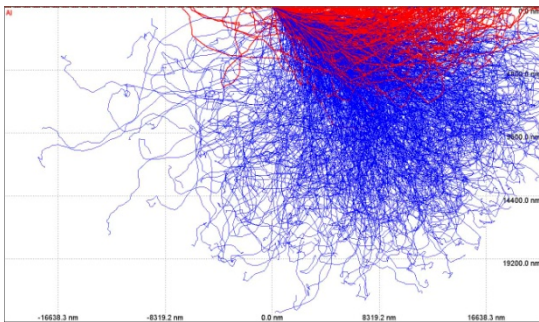
a)

90° Incidence angle, 0.106 backscattering coeff.



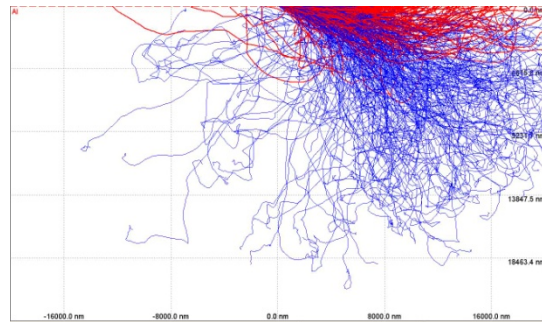
b)

60° Incidence angle, 0.145 backscattering coeff.



c)

30° Incidence Angle, 0.308 backscattering coeff.



d)

1° Incidence angle, 0.748 backscattering coeff

Figure 7-7 Relationship between backscattering and angle of the incident electron beam on aluminum substrate

Simulations were run for various angles of incidence and their corresponding backscattering coefficients. This has been represented in the figure 7-8.

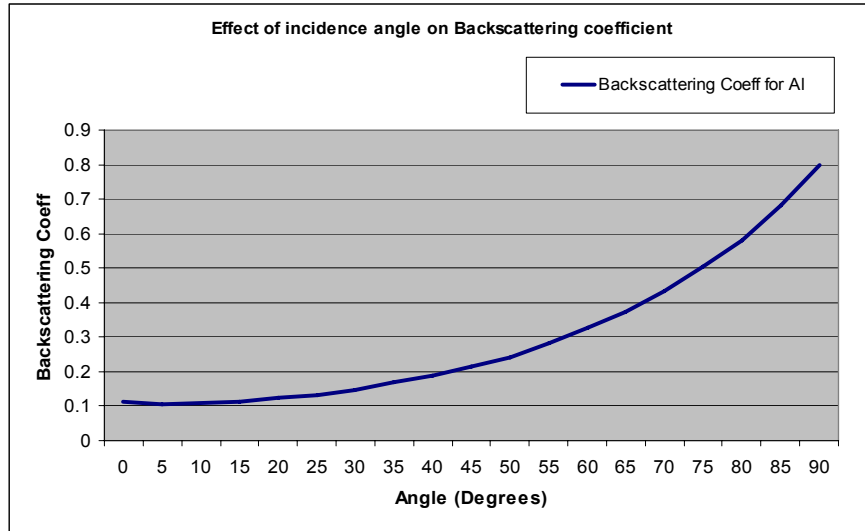


Figure 7-8 Relationship between backscattering coefficient and the angle of incidence of an electron beam

The relationship between the backscattering coefficient, ξ and its dependence on the angle θ is defined by the following equation

$$\xi(90^\circ - \theta) = \frac{1}{(1 + \text{Cos}(90^\circ - \theta))^p}$$

Where $p = 9/\sqrt{Z}$ and Z represents the Atomic number of the substrate material and θ is the electron beam's angle of incidence.

The powders used in the EBM system are typically spherical because of both the requirement for good flow characteristics during the raking process and as a result of gas atomizing methods used for manufacturing the powder. Due to the spherical shape of the

powder, the amount of backscattering would be considerably higher than that observed when the beam is normal to the surface of flat substrate.

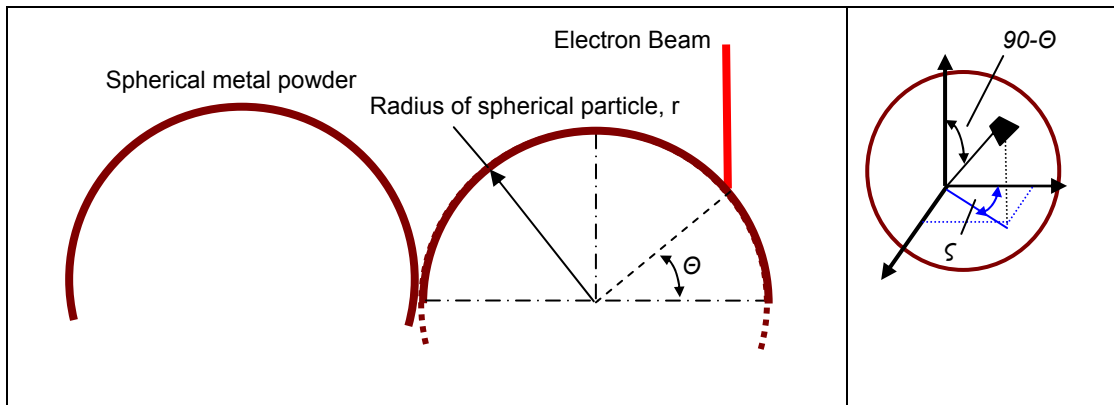


Figure 7-9 Interaction between spherical powder used in EBM processing and the electron beam

If the beam is assumed to be a point source of energy, a normalized backscattering coefficient across the entire surface of the powder can be approximated as, ξ_{total} , where,

$$\xi_{total} = \frac{1}{2\pi r^2} \int_{\theta=0}^{\pi/2} \int_{\phi=0}^{2\pi} r^2 \cos(\theta) \sin(\theta) \frac{1}{(1 + \cos(90^\circ - \theta))^{9/\sqrt{Z}}} d\phi d\theta$$

Since the distance between the cathode and the powder bed is much higher than the width of the powder bed the beam would be assumed to hit the powder bed vertically as shown in Figure 7-9. It is also assumed that the defocusing of an electron beam due to micro variations in the powder level and any charge build up on a particle due to the scanning beam shall be ignored.

7.2 Simulation

The main distinction between conventional welding and the EBM process is that the process uses powder metal as the raw material spread across the entire build envelope. Parameters such as thermal conductivity and emissivity vary as a function of the level of sintering (this includes melting), temperature, shape and size of the powder. The focused energy welding simulation models typically involve a single scan whose path can be represented as a single spine or point over a relatively homogenous material.

7.2.1 Finite Elements Method

Finite element methods were initially used with the aid of COMSOL Multiphysics® environment to simulate electron beam melting.

The heating of the start plate prior to starting the actual part build was simulated in COMSOL using a square (120x120x15mm) stainless steel start plate embedded in a bed of Aluminum alloy 7075 powder (250x250x40mm). The 7075 powder was assigned a thermal conductivity which was 5% of the bulk conductivity for that alloy. Heat loss due to radiation has been ignored in this model.

In the EBM, the beam is scanned over the stainless steel start plate under 60KV acceleration voltage at 10,000 mm/s with a beam current of 35 mA. Since the scan speeds are large over a relatively small surface area, it was possible to simplify the model by normalizing the incident heat over the scanned area as a planar heat source. The

incident power can be modeled using information on the geometry of the scanned area, acceleration voltage, normalized backscattering coefficient and scan parameters line offset (distance between two adjoining scans).

This model provides a reliable estimate of temperature on the surface of the plate with respect to temperature read at the bottom of the plate (Figure 7-10). A method for dynamically measuring variations in the conductivity and emissivity of the sample are yet to be determined.

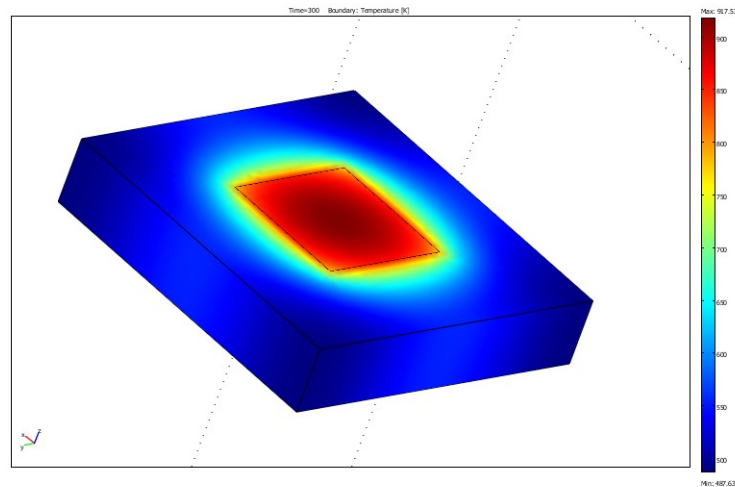


Figure 7-10 Simulation of the initial heating of a Start plate embedded in a bed of Aluminum Powder

Arcam AB, the developer of the electron beam melting systems has been using a model similar to the one described above for approximating the melting within a part [121]. The part is differentiated between regions that are solid and the rest which is in powder form.

The powder form is modeled with a low density meshing. The solid part is modeled with higher density mesh as is obvious from the figure below. The incident energy is modeled as a planar heat source spanning the entire region within a slice that is being melted. The primary limitation of this model is the lack of ability to model transitions between multiple layers as well as the lack of capability in modeling the actual tool path of the scan.

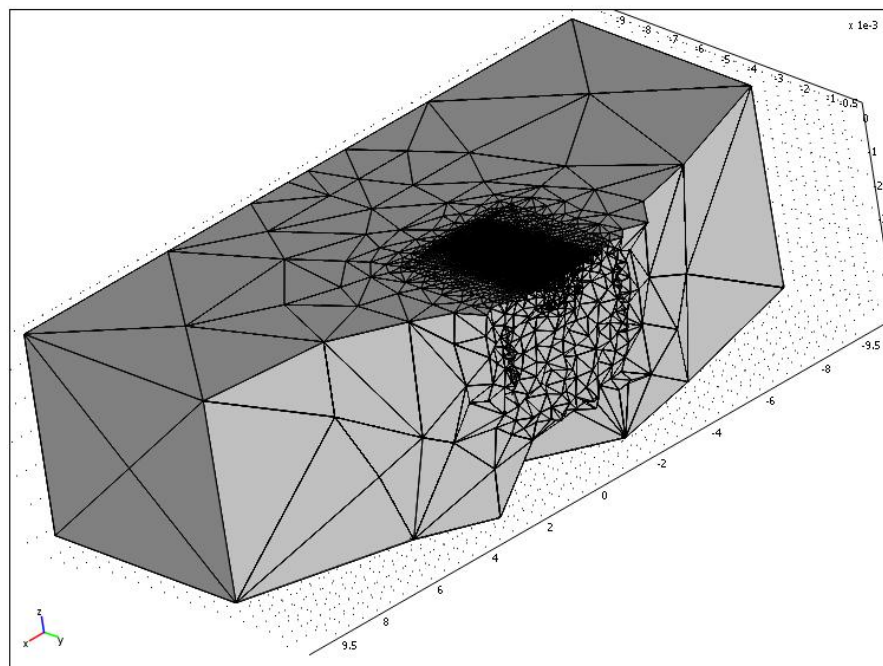


Figure 7-11 Arcam AB's model for electron beam melting

Two separate approaches were used for simulating electron beam melting. The first model involved representation of the electron beam scan as a point source of incident energy. The beam's intensity was modeled to exponentially decay as a function of the

depth of penetration. This behavior of the beam was modeled as a 1D model and it was mapped into the 3D model [122, 123].

$$\frac{\partial P}{\partial x} = -\left(1 - \xi_{total}\right)P$$

Variable meshing was used to achieve higher resolution around the region where beam interacts with the solid. The maximum mesh size around the scan path was set to 1 mm. The absolute thermal conductivity of the substrate was modeled as a function of the temperature of the system.

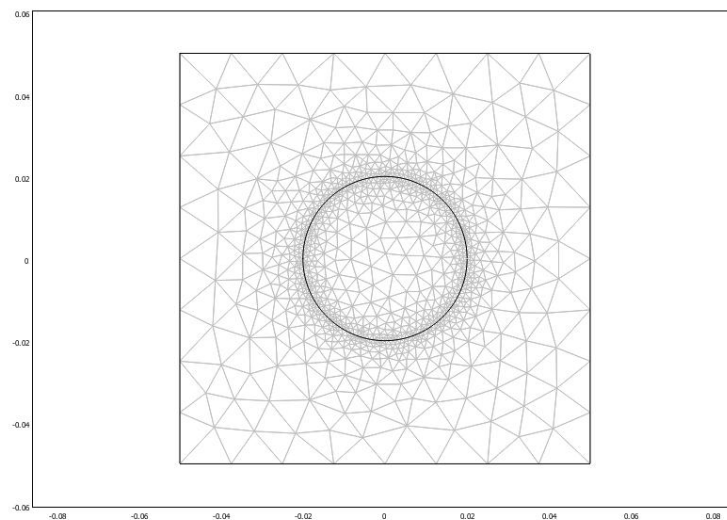


Figure 7-12 Variable density mesh generated along the circular path

This approach had more parallels with the interaction observed between a laser and a substrate as electron beams have a larger penetration depth. The electrons also dissipate

the energy upon entering the system in a form that resembles a cone. This model was developed by scripting the scan path into COMSOL using Matlab[®].

The limitation of this approach is that the scan paths during EBM processing span a large area and a large portion of the model would need to be meshed using a finer mesh size. The complexity of the model will increase drastically as the number of layers within a model increased. The figure below shows beam scan path using a uniform high density mesh across the entire region that was being evaluated. A script was written to scan the beam to trace the periphery of a box. As is evident from figure 7-13, the lower resolution of the mesh caused the beam path to scatter around the straight scan line it was meant to follow.

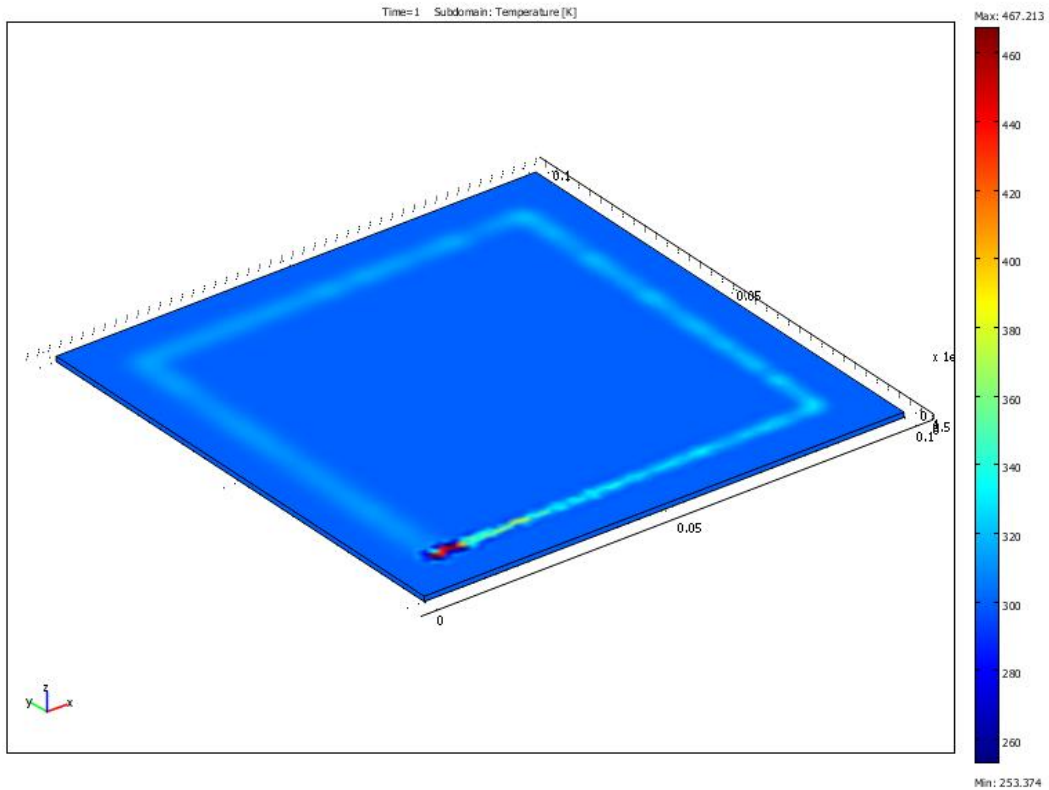


Figure 7-13 Beam scan path over a region meshed to uniform density

The methods described above required the beam path to be represented within the COMSOL[®] file. Freeform fabrication techniques like EBM melting might require variation of the beam path and processing parts for every single layer of the part. This would be difficult to achieve using a simple script. An alternative method for doing this was to sub-divide the part into smaller voxels (sub-domains). The specific surface of the voxel over which the beam was scanned was treated as a planar source of energy rather than a point source. Figure 7-14 shows this representation. Voxels could be represented in a manner to locally assign material properties to individual voxel. The creation of the

voxels could also be ordered in order to represent the relationships between neighbouring voxels. The simulation involved folding a planar energy source over a voxel conducting a transient analysis for a small amount of time and then moving the energy source to the adjoining voxel as per the beam path. The results from the previous simulation would be used as the input for the next simulation. A structured method of representing voxels made it possible to externally trigger the movement of the voxels using a code developed in Matlab[®].

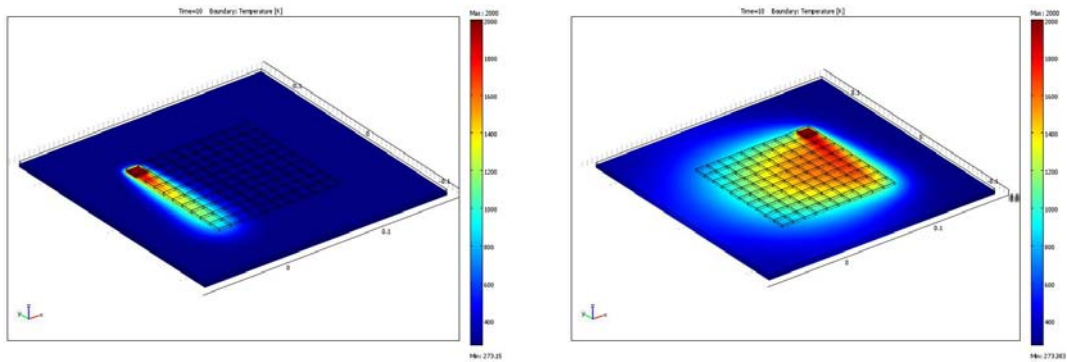


Figure 7-14 Simulation of e-beam scanned over 7075 powder carried out in COMSOL[®] by breaking down the part into voxels to facilitate the tracing of the beam.

The order in which the voxels were created could be set up in a fashion to retain the relationship between a voxel and its neighbors. This ordering made it possible to move the energy source by selectively changing boundary conditions on individual voxels to imitate a scanning beam. This behavior could be externally controlled through a secondary programming language like Matlab[®].

The limitation of this model was that the individual voxels were further sub-divided by meshing. The size of the voxel dictated the density of the mesh. The high density of the mesh greatly limited the size of the model. The voxels in figure 7-14 are 10x10x1mm in size. A model consisting of 100 voxels would make the simulation crash due to lack of memory.

7.2.2 Finite Difference Method

A big constraint in using commercial FEA software for modeling continuous but non-repetitive processes like layered manufacturing is the limitations set forth by the ability to script the process subtleties associated with such processes. As discussed previously, scripting methods had to be understood in order to develop scan paths. These scan paths would vary in every single layer and this limits the ability to have a consistent method for meshing and constraining the models for layered manufacturing. The other big problem with using commercial FEA software was the inability to consistently model the build up and remelting of subsequent layers. Recalculation of the temperature across the model in a subsequent layer would involve remeshing the added mass of powder without losing the temperature profiles generated during the melting of the previous layers.

The Finite Difference method was selected as a means for circumventing these limitations for multiple reasons. This method begins with discretization of both time and space such that every point in space and time can be broken down into integer values. For the sake of this study, the space is discretized into equal intervals that are 0.1mm

apart in Euclidean space. This works conveniently for this example as this is the maximum operating resolution required on the EBM.

The time interval between evaluations is dependent on the type of scan pattern being evaluated. The scan speeds during the sintering cycles are high enough to assume a time interval equal to the time required to complete one scan across the surface. This can be determined from the figure 7-15

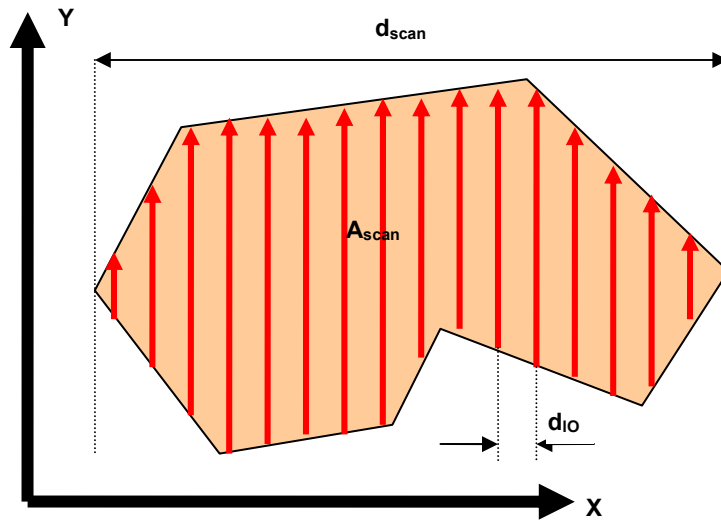


Figure 7-15 High speed electron beam scan paths during sintering

$$\Delta t_{sinter} = \frac{A_{scan}}{v_{scan} \times d_{LO} \times n_{sinter}}$$

$$n_{sinter} = \frac{d_{scan}}{d_{LO}} + 1$$

where n_{sinter} represents the number of raster scan per cross-section, A_{scan} is the total area to be scanned and d_{scan} is the width of the cross-section measured in the direction perpendicular to the scan direction.

The scan velocity during the melting scans is significantly lower than those used for the preheating scans. This can be determined as

$$\Delta t_{\text{melt}} = 0.1/v_{\text{scan}}$$

As previously discussed, the entire 3D space can be discretized into units that are 0.1mm apart. In a single dimension system, the interval in space is defined as

$$\Delta x = 0.1\text{mm} = x_{i+1} - x_i$$

Similarly, the time steps are defined as

$$\Delta t = t_{n+1} - t_n$$

The first order derivatives in time and space are defined as :

$$\left. \frac{\partial T}{\partial t} \right|_{x_i, t_{n+1/2}} \cong \frac{T_{i,n+1} - T_{i,n}}{\Delta t}$$

$$\left. \frac{\partial T}{\partial x} \right|_{x_{i+1/2}, t_n} \cong \frac{T_{i+1,n} - T_{i,n}}{\Delta x}$$

The second order derivatives in space can be approximated as:

$$\frac{\partial^2 T}{\partial x^2} \Big|_{x_i, t_n} \cong \frac{\frac{\partial T}{\partial x} \Big|_{x_{i+1/2}, t_n} - \frac{\partial T}{\partial x} \Big|_{x_{i-1/2}, t_n}}{\Delta x} \cong \frac{T_{i-1, n} - 2T_{i, n} + T_{i+1, n}}{(\Delta x)^2}$$

With a 0.1mm resolution in 3D space, the discretized space would consist of 2500 x 2500 points in the build plane. The number of discrete points along the Z axis would be dependent on the size of the part. Special methods are necessary for evaluating regions near the boundary of this 3D space.

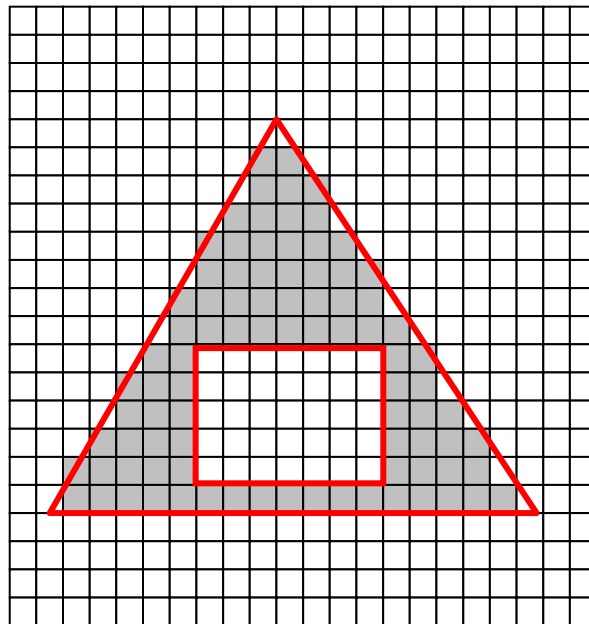


Figure 7-16 A discretized slice file (SLC)

This 3D space is discretized by evaluating the slice file (SLC file) and breaking a layer down into intervals 0.1 mm apart. This is achieved by parsing the SLC file; a collection

of 2D contours via ray tracing to form a bit map like image as show in the figure 7-16.

The heat transfer equation can be defined for EBM melting as

$$c_p \rho \frac{\partial T}{\partial t} - k \nabla^2 T = \dot{q} + A \varepsilon \sigma (T_{amb}^4 - T^4)$$

The rightmost component of this equation defines the energy in the form of radiant heat from the surface of the powder bed. The variable, A, defines the area emitting the heat and σ is the Stefan-Boltzman constant. Emissivity of the material is defined by ε . In actual EBM processing scenario, the emissivity of the material will change based on the level of sintering and temperature of the surface. For this model, it is assumed that the emissivity remains constant. For the sake of simplicity, it is assumed that the energy is lost only through the layer that is currently being processed (the top layer). The build chamber of the EBM system is assumed to be held at one hundred degrees Kelvin above room temperature, T_{amb} . This is a reasonable assumption given that the mass of the build chamber is considerably larger than that of the 100 microns layer that is being melted.

The bulk density of the material is defined as ρ , and the specific heat is defined as c_p . The effect of powder densification on the specific heat of the powder is ignored. The picture below shows the electron beam scanning in a homogeneous low conductivity medium. Effects of radiant heat loses are ignored

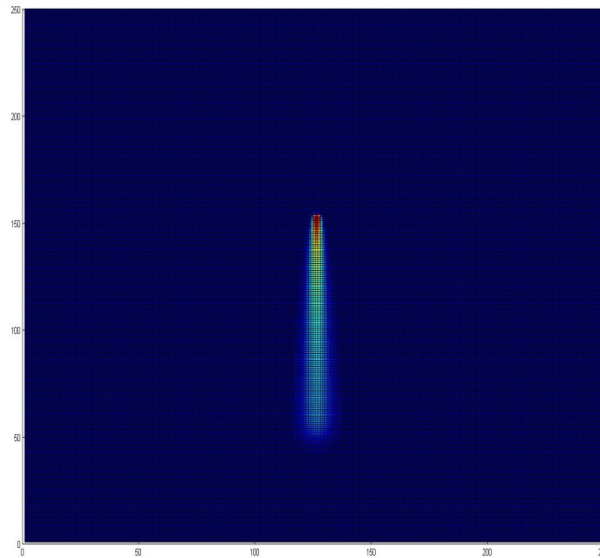


Figure 7-17 Profile of an electron beam scanning over homogenous low thermal conductivity material. Effect of radiant heat loss has been ignored

The thermal conductivity, κ , is also dependent on the extent of sintering and temperature of the material. The thermal conductivity can be broken down into two components, κ_{sint} & κ'_{temp} . The component κ_{sint} is the thermal conductivity of a material at room temperature for a specific level of sintering. The component κ'_{temp} is the ratio of the bulk conductivity of a material at temperature T, κ_{temp} , to the bulk thermal conductivity of the material at room-temperature, κ_{bulk} . These values are defined as

$$\kappa'_{\text{temp}} = \frac{\kappa_{\text{temp}}}{\kappa_{\text{bulk}}} \quad \text{and} \quad \kappa = \kappa'_{\text{temp}} \times \kappa_{\text{sint}}$$

Note that the sintering component of conductivity is dependent on densification of the powder and is independent of the temperature. Once the powder is sintered, the component, κ_{sint} is not reversed even if the temperature of the material decreases. The possibility that necks formed during sintering will break due to thermal contraction during cooling is ignored.

Though the above described finite difference model outputs a temperature measure, what it is actually doing is calculating the energy within a given voxel. This value can then be adjusted to account for any latent heat associated with fusion or phase transformations that occur in alloys.

As previously discussed, the void fraction or sintering within a material can be approximated as an exponential function of sintering rate. In order to simplify this further, it is proposed to inspect the time a given voxel of material spends between two threshold temperatures as a measure of their level of sintering. Let this amount of time be called t_{sint} . The threshold temperatures can be anywhere between the solidus and liquidus temperatures for an alloy (latent heat of fusion shall be calculated for pure metals). The threshold temperatures can be represented as T_{thresh1} & T_{thresh2} , such that $T_{\text{thresh1}} < T_{\text{thresh2}}$. As can be seen here, this assumption suggests a constant sintering rate. If a part is held between the threshold temperatures for a time greater than t_{sintmax} , one can assume that the voxel assumes the conductivity of the bulk material. The calculation of sintering within a voxel has been approximated below (figure 7-18).

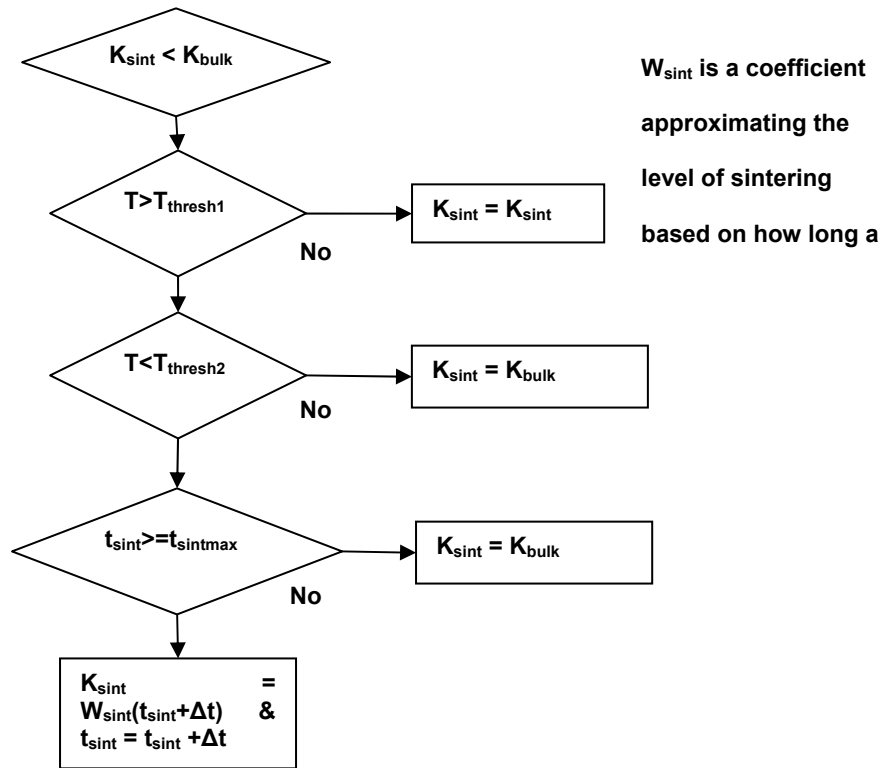


Figure 7-18 Approximating level of sintering

Future models could evaluate temperature gradients over time to establish better approximations for the level of sintering.

The model was defined using Matlab and it requires contiguous memory blocks for the processing of large data sets like the ones used in this model. Windows XP Operating system was used for running Matlab. Windows XP has thresholds on the maximum

amount of memory that can be used. Evaluation of large data sets can be simplified using two possible options.

The first option requires storage of large data sets as a file. The data files are opened and evaluated sequentially in smaller blocks every time a large computation is carried out. The opening and writing of the files during evaluation, substantially slows down the process.

A second option involves selectively discretizing 3D space based on the level of detail required in a localized region (Figure 7-19). The top couple of layers that are being melted can be evaluated at a high resolution (0.1mm). Lower layers can be evaluated at a lower resolution. The data between sections of layers of varying resolution can be interpolated by averaging values for voxels with higher resolution and mapping them into regions of lower resolution.

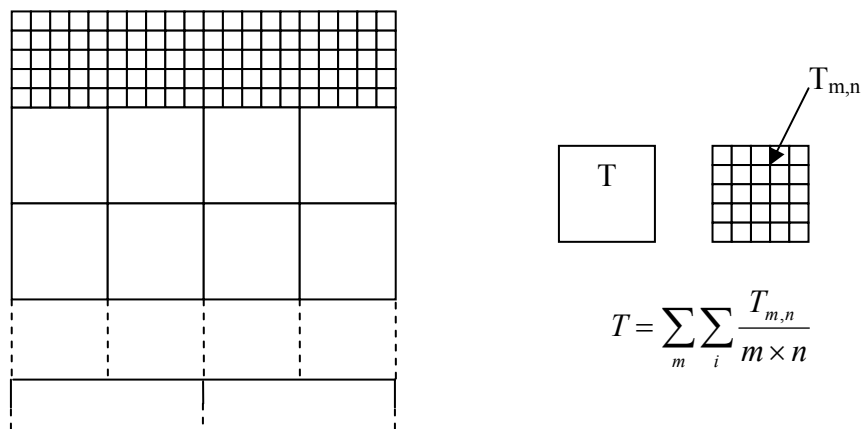


Figure 7-19 Selective resolution for large data sets

Just like Finite Element Models, the accuracy and stability of a finite difference model is defined by the Fourier number, F_o , for that given simulation model. This value is defined by

$$F_o = \frac{\kappa \Delta t}{\rho C_p (\Delta x)^2}$$

This value can be thought of as the ratio of the time step and the time required to equilibrate one step space interval. A lower Fourier number results in a stable system. Fourier numbers larger than 0.5 can cause new temperature values to overshoot those of its neighbors. Care would be required while selecting time intervals during large area sintering or while selectively changing space resolution in the data set.

Chapter 8 Conclusion

The past few chapters covered experiments related to development of new materials for processing using the electron beam melting process. Each new material development project described as part of this work required approximately 4-5 months of dedicated machine and operator time. As can be seen from the various materials development experiments, a commercially viable materials development approach needs to go beyond thermal analysis of the EBM process. Good processing parameters should produce parts that are accurate, dense, have the right grain structure, exhibit low internal stress and maintain the right composition. In order to achieve this, it is important to have a reliable simulation model based on the guidelines described in the previous chapter. Closed loop feedback needs to be built into the EBM system to extract data on the surface temperature, sintering levels, local conductivity, emissivity and evaporation during the build. This data can be fed back to the simulation model to make the necessary changes to the processing parameters.

In order to process a part it is critical that the metal powder does not develop a charge and “smoke” during the processing. An empirical analysis of the charging of the powder can be conducted based on the ratios of material density to powder resistivity, assuming particle size and shape factor remain constant amongst all new material powders. As part of initial feasibility study, fixed regions of the cold powder samples could be scanned over with a fixed line offset but with varying scan speeds and electron beam currents.

The combination of current and speed with respect to the scan length, L_{scan} , at which the powder particles repel to cause smoke could be noted and set as threshold conditions. It can be hypothesized that

$$\text{Chance of Powder Smoking} \propto \frac{(\text{Scan Speed}) * (\text{Beam Current}) * (\text{Line Offset})}{(\text{Scan Length}) * (\text{Density}) * (\text{Conductivity})}$$

The threshold combination of the scan speeds and beam currents can be used as constraints when determining optimizing processing parameters to achieve the desired level of melting without causing “smoking” during part processing.

The electron beam melting process is currently setup as an open loop process with the temperature at the bottom of the start plate along with the electron beam column and chamber pressures serving as the only means of feedback. Any quantitative analysis on the quality of the build was post-completion. So far, an infrared camera has not been integrated to read the surface temperature of the powder bed. X-rays are a by-product of the electron beam melting process. Lead glass covered by either a Kapton film or movable metal shutter are used on all view ports on the machine in order to shield the machine operator from X-rays. These viewports do not permit the transmission of infrared wavelengths. There are plans to integrate a combination of alternative materials for viewport glass and shutter mechanism in order to integrate an infrared camera into the EBM system at NC State University.

The feedback generated during the processing of the part and the corrective action taken by the operator was subjective. Feedback during preheating was based on the visible light emitted during the heating. This was monitored either with naked eye using the viewport or with the help of the CCD camera that is mounted on all the Arcam S12 system. The sintering of powder was approximated based on the nature of visible light radiated by the scanned region. When a powder is sintered, the heat from two consecutive line scans effectively transfers to the un-scanned powder between these scans, causing it to glow (Figure 8-1).

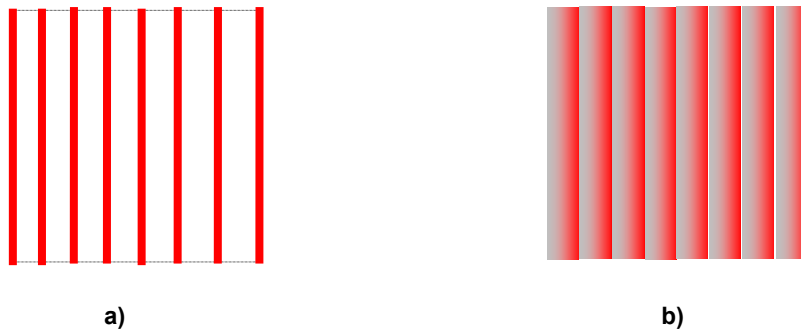


Figure 8-1 Visible light emitted by preheated powder bed when a) loose b) sintered

The level of sintering necessary during preheating of a part is very low and the sintered region does not have any structural integrity to evaluate the thermal conductivity after the completion of the build. Secondly, the level of sintering in loosely sintered powder varies as a function of the temperature as well. As the powder cools, its particles contract severing any little necking that might have been formed during the sintering of the powder.

In situ data on the extent of sintering could be extracted by observing the percentage of the scanned region that is above a threshold temperature. Higher the percentage of scanned region that is above the threshold temperature, higher would be the level of sintering.

Once this data on the level of sintering is extracted, the information could be mapped to approximate both the thermal conductivity and emissivity of that region.

Similar to the preheating cycles, it is also possible to observe images from the CCD camera to approximate the extent of melting during the melting cycle. It was observed that incomplete melting of the powder during the melt cycles caused the melt region to glow brighter. This was because the vacuum atmosphere in combination with the low contact area between powder particles caused the particles to be thermally isolated. The particles would absorb heat while they were not completely melted but were unable to dissipate this heat to the rest of the material. Once the melt layer is fully melted, the thermal conductivity of the region is drastically increased and the heat in the melt region can be rapidly dissipated to the rest of the part and start plate.

Experiments for the processing of aluminum alloy 7075 and 6061 have shed light on the need to monitor material composition during the build. The localized temperature and chamber vacuum data in combination with the Clausius-Clapeyron relationship [124] can be used to determine the localized evaporation of the alloying elements in a build. The computed vaporization can be compared with the actual composition of vapors in the

vacuum chamber using either mass spectroscopy or X-ray fluorescence spectroscopy (XRFS). The exact engineering of placing the probe in the system to accurately measure the chamber composition would have to be coordinated through with Arcam AB. XRFS would require incorporating a secondary source of x-rays pointed at a cold-surface where the metal vapors can condense.

The simulations described in the previous chapter are but the first step towards establishing a model for freeform electron beam melting (EBM) of parts. The voxelized thermal data obtained from the finite difference models can be easily changed by mapping data from an infrared imaging system back as an input to define the temperature, conductivity and sintering profile for the top layer of build. This can enable real time correction of processing parameters during a build. The temperature and thermal gradients within the model, plotted over time can help understand any internal stresses as well as grain structure within the part. This can open interesting possibilities in developing locally graded grain structures and compositions in freeform fabricated parts.

A closed loop system that can analyze different inputs to compute properties of the built part would require substantial computational resources. The current structure of the 3D voxel data slows down the computation. Previously, models were suggested for simplifying the representation and computation with large data sets. Another option for handling large data set within Matlab[®] would be to look into the option of using its

Parallel Computation Toolbox. The author had previously implemented the massively parallel algorithms for computing mechanical metamaterials. Figure 8-2 plots the time taken to compute vs. number of iterations in both parallel mode (quad core) and normal mode. Similar algorithms can be implemented in C++ to speed up the process.

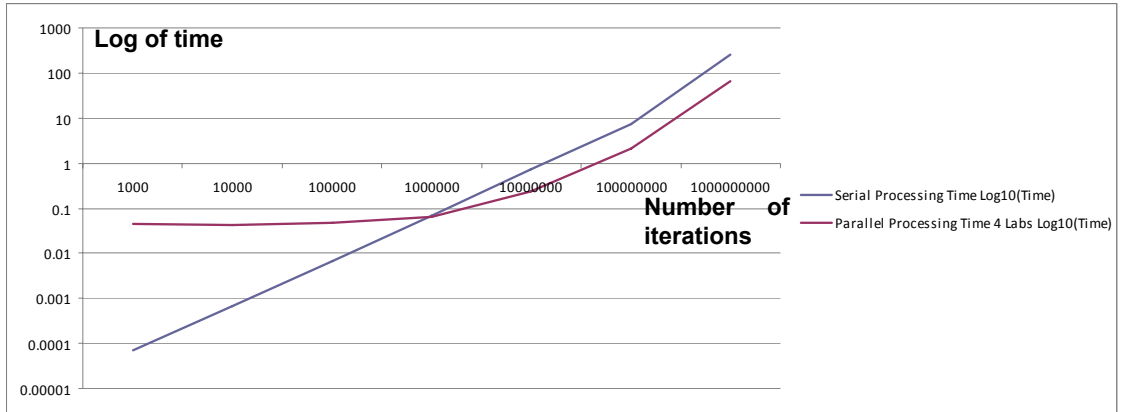


Figure 8-2 Massively parallel algorithms using Matlab® parallel computation toolbox

Another area that requires exploration is the influence of convection in electron beam melting. Convective heat transfer in welding is typically addressed by evaluating flows due to thermal gradients within and around a weld pool.

An electron has a finite mass and its velocity is dictated by the applied acceleration voltage. Just like a water jet hitting a pool of water, the electrons will churn the weld pool upon hitting purely because of the transference of momentum. This effect will be pronounced and a model needs to be established in order to examine it. It should be possible to control the convective heat flow in a weld pool by controlling scan

parameters like the localized spin in an electron beam to induce shear forces in the weld pool (refer figure 8-3). Shear forces could help retard the columnar grain structure and help promote more equiaxed grains.



Figure 8-3 Electron beam scanned a) without b) with a spin

The effect of the charge on the electron beam and its effect on metal solidification has not been studied but it remains an area of interest for researchers at NC State University.

In conclusion, this study provides guidelines for conducting new material development using the EBM process, as well as models for simulating new materials. Suggestions have been made to develop methods and supporting setups needed for closed loop feedback for temperature, powder density, thermal conductivity and composition during processing. Direct metal fabrication processes are still emerging as processes of choice for custom fabrication process for critical components. The inertia in adopting such processes is due to lack of absolute certainty in the characterization of parts built using such processes. The work presented here hopes to contribute towards better understanding the electron beam melting process.

REFERENCES

1. Himmer, T., T. Nakagawa, and M. Anzai, *Lamination of metal sheets*. Computers in Industry, 1999. 39: p. 27-33.
2. Nakagawa, T., *Recent developments in auto body panel forming technology*. Annals of CIRP, 1993. 42(2).
3. Himmer, T., et al., *Recent developments in metal laminated tooling by multiple laser processing*. Rapid Prototyping Journal, 2003. 9(1): p. 24-29.
4. Kong, C.Y. and R.C. Soar, *Characterisation of aluminum alloy 6061 for the ultrasonic consolidation process*. Materials Science and Engineering A, 2003. A363: p. 99-106.
5. Kong, C.Y. and R.C. Soar, *Fabrication of metal-matrix composites and adaptive composites using ultrasonic consolidation process*. Materials Science and Engineering A, 2005. 412(1-2): p. 12-18.
6. Sachs, E., S.P. Micheals, and S.M. Allen, *Tooling made by solid free form fabrication techniques having enhanced thermal properties*, in *US Patent Office*. 2000, Massachusetts Institute of Technology: USA.
7. Sachs, E.M., et al. *The distributed design and fabrication of metal parts and tooling by 3D Printing*. in *Proceedings of the 1999 NSF design and manufacturing grantees conference*. 1999. Long Beach, CA.
8. Micheals, S., E.M. Sachs, and M.J. Cima. *Metal parts generation by three dimensional printing*. in *Solid Freeform Fabrication Symposium*. 1992. Austin, TX; USA.
9. Shivpuri, R., et al., *Evaluation of 3D printing for dies in low volume forging of 7075 aluminum helicopter parts*. Rapid Prototyping Journal, 2005. 11(5): p. 272-277.
10. Souveignier, C.W., et al., *Freeform fabrication of aluminum metal-matrix composites*. Journal of materials research, 2001. 16(9): p. 2613-2618.
11. Agarwala, M.K., et al., *Structural quality of parts by fused deposition*. Rapid Prototyping Journal, 1996. 2(4): p. 4-19.

12. Greulich, M., M. Greul, and T. Pintat, *Fast, functional prototypes via multiphase jet solidification*. Rapid Prototyping Journal, 1995. 1(1): p. 20-25.
13. Dimov, S.S., et al., *Rapid tooling applications of the selective laser sintering process*. Assembly automation, 2001. 21(4): p. 296-302.
14. Evans, R.S., et al., *Rapid manufacturing of silicon carbide composites*. Rapid Prototyping Journal, 2005. 11(1): p. 37-40.
15. Tolochko, N.K., et al., *Mechanisms of selective laser sintering and heat transfer in Ti powder*. Rapid Prototyping Journal, 2003. 9(5): p. 314-326.
16. Agarwala, M.K., et al., *Direct selective laser sintering of metals*. Rapid Prototyping Journal, 1995. 1(1): p. 26-36.
17. Agarwala, M.K., et al., *Post-processing of selective laser sintering parts*. Rapid Prototyping Journal, 1995. 1(2): p. 36-44.
18. Das, S., et al., *Direct laser freeform fabrication of high performance metal components*. Rapid Prototyping Journal, 1998. 4(3): p. 112-117.
19. Dalgarmno, K.W., *Production grade tooling via layer manufacture*. Rapid Prototyping Journal, 2001. 7(4): p. 203-206.
20. Engel, B. and D.L. Bourell, *Titanium alloy powder preparation for selective laser sintering*. Rapid Prototyping Journal, 2000. 6(2): p. 97-106.
21. Subramanian, K., et al., *Selective laser sintering of alumina with polymer binder*. Rapid Prototyping Journal, 1995. 1(2): p. 24-35.
22. Taylor, C.S., et al., *"Spatial Forming" A three dimensional printing process*, Advanced Cardiovascular Systems Inc: Santa Clara, CA.
23. Chait, A.L., *High volume print forming, HVPF A new method for manufacturing large volume of complex metal-ceramic and hybrid components*, Eoplex Inc: Redwood City, CA.
24. Oh, J.H., et al., *Process control of reactive rapid prototyping for nickel-aluminides-II*. Materials Science and Engineering A, 2003. 349(1-2): p. 292-297.
25. Oh, J.H., et al., *Process control of reactive rapid prototyping for nickel-aluminides*. Materials Science and Engineering A, 2002. 334(1-2): p. 120-126.

26. Orme, M., et al., *Electrostatic charging and deflection of nonconventional droplet streams formed from capillary stream breakup*. Physics of fluids, 2000. 12(9): p. 2224-2235.
27. Orme, M., et al., *Molten Aluminum micro-droplet formations and deposition for advanced manufacturing applications*. Aluminum transactions journal, 2000. 3(1): p. 95-103.
28. Orme, M., Q. Liu, and J. Fischer. *Mono-disperse aluminum droplet generation and deposition for net-form manufacturing of structural components*. in *8th International conference on liquid atomization and spray systems*. 2000. Pasadena CA.
29. Orme, M. and R.F. Smith, *Enhanced aluminum properties by means of precise droplet deposition*. Transactions of the ASME, 2000. 122: p. 484-493.
30. Schiaffino, S. and A.A. Sonin, *Molten droplet deposition and solidification at low Weber numbers*. Physics of fluids, 1997. 9(11): p. 3172-3187.
31. Fessler, J.R., et al. *Functional gradient metallic prototypes through shape deposition manufacturing*. in *Proceedings of the solid freeform fabrication symposium*. 1997. Austin, TX.
32. Merz, R., et al. *Shape Deposition Manufacturing*. in *Proceedings of the solid freeform fabrication symposium*. 1994. Austin, Tx.
33. Atwood, C., et al. *Laser Engineered Net Shaping (LENS): A tool for direct fabrication of metal parts*. in *International Congress on Application of Lasers & Electro-optics (ICALEO)*. 1998. Orlando, FL.
34. Hofmeister, W., et al., *Solidification in direct metal deposition by LENS processing*. Journal of Metals, 2001. 53(9): p. 30-34.
35. Mazumder, J., A. Schifferer, and J. Choi, *Direct materials deposition: designed macro and microstructure*. Materials research innovations, 1999. 3(3): p. 118-131.
36. Cormier, D., O. Harrysson, and H. West, *Characterization of high alloy steels produced via electron beam melting*. Rapid prototyping journal, 2004. 10(1): p. 35-41.
37. Haftka, R.T., *Structural shape optimization-a survey*. computer methods in applied mechanics and engineering, 1986. 57: p. 91-106.

38. Ellis, D.L., *GRCop-84: A High Temperature Copper Alloy for High Heat Flux Applications*. 2005.
39. Ellis, D.L. and D.J. Keller, *Thermophysical properties of GRCop-84*. 2000.
40. Ogbuji, L. and D. Humphrey, *Comparison of oxidation rates of some new copper alloys*. *Oxidation of Metals*, 2003. 60(3/4): p. 271-291.
41. Thomas-Ogbuji, L., D. Humphrey, and J. Setlock, *Oxidation Reduction Resistance of Advanced Copper Alloys*. 2003.
42. Hickman, R., et al. *Materials Properties of Net Shape, Vacuum Plasma Sprayed GRCop-84*. in *39th AIAA/ASME/SAE/ASEE Joint Propulsion Conference and Exhibit*. 2003. Huntsville, Alabama.
43. Boyer, R., G. Welsch, and E. Collings, *Materials Property Handbook: Titanium Alloys*. 1994, ASM International.
44. Merzhanov, A.G., *The chemistry of self-propagating high-temperature synthesis*. *Journal of materials chemistry*, 2004. 14: p. 1779-1786.
45. Froes, F.H., C. Suryanarayana, and D. Eliezer, *Review: Synthesis, properties and applications of titanium aluminides*. *Journal materials science*, 1992. 27: p. 5113-5140.
46. Wu, X., *Review of alloy and process development of TiAl alloys*. *Intermetallics*, 2006. 14: p. 1114-1122.
47. Loria, E.A., *Review: Quo vadis gamma titanium aluminide*. *Intermetallics*, 2001. 9: p. 997-1001.
48. Donachie, M., *Titanium: A technical guide*. 2000: ASM International.
49. Lasalmonie, A., *Intermetallics: Why is it so difficult to introduce them in gas turbine engines?* *Intermetallics*, 2006. 14: p. 1123-1129.
50. Weaver, M.L., C.W. Calhoun, and H. Garmestani, *Microstructure, texture and mechanical properties of continuously cast gamma TiAl*. *Journal materials science*, 2002. 37: p. 2483-2490.
51. Rahaman, M.N., R.E. Dutton, and S.L. Semiatin, *Fabrication of dense thin sheets of gamma-TiAl by hot isostatic pressing of tape-cast monotapes*. *Materials Science and Engineering A*, 2003. A360: p. 169-175.

52. Habel, U. and B. McTiernan, *HIP temperature and properties of gas atomized gamma-titanium aluminide alloy*. Intermetallics, 2004. 12: p. 63-68.
53. Rawers, J.C. and W.R. Wrzesinski, *Reaction-Sintered hot-pressed TiAl*. Journal materials science, 1992. 27: p. 2877-2886.
54. Bertolino, N., et al., *Ignition mechanisms in combustion synthesis of Ti-Al and Ti-Ni systems*. Intermetallics, 2003. 11: p. 41-49.
55. Wang, C., et al., *Laser-induced self-propagating reaction synthesis of amorphous-based composite Zr-Al-Ni-Cu alloys* Journal of Materials Science, 2003. 38(7): p. 1377-1381.
56. Kuang, J.P., R.A. Harding, and J. Campbell, *Microstructure and mechanical properties of an investment cast gamma titanium aluminide*. Materials Science and Technology, 1999. 15: p. 840-850.
57. Wang, J., J. Yang, and Y. Wang, *Grain refinement of a Ti-47Al-8Nb-2Cr alloy through heat treatments*. Scripta Materialia, 2005. 42(4): p. 329-334.
58. Zheng, R., et al., *The ambient temperature tensile behavior of duplex γ -TiAl-based alloys* Materials Science and Engineering A, 2003. 362(1-2): p. 192-199.
59. Srivastava, D., *Microstructural characterization of the γ -TiAl alloy samples fabricated by direct laser fabrication rapid prototype technique* Bulletin of Materials Science, 2002. 25(7): p. 619-633.
60. Srivastava, D., *The effect of process parameters and heat treatment on the microstructure of direct laser fabricated TiAl alloy samples* Intermetallics, 2001. 9: p. 1003-1013.
61. Srivastava, D., et al., *The influence of thermal processing route on the microstructure of some TiAl-based alloys* Intermetallics, 1999. 7(10): p. 1107-1112.
62. Srivastava, D., I. Chang, and M. Loretto. *Microstructural studies of Direct Laser Fabricated TiAl*. in *Proceedings of the Symposium on Gamma Titanium Aluminides*. 1999. San Diego, CA: TMS.
63. Moll, J., et al. *Laser forming of gamma Titanium Aluminide*. in *Proceedings of the symposium on gamma titanium aluminides*. 1999. San Diego, CA.

64. Liu, W. and J. DuPont, *Fabrication of Carbide Particle Reinforced Titanium Aluminide Matrix composites by Laser Engineered Net Shaping*. Metallurgical and Materials Transactions A, 2004. 35A: p. 1133-1140.
65. Liu, W. and J. DuPont. *Fabrication of Titanium Aluminide Matrix Composites by Laser Engineered Net Shaping*. in *Proceedings of Symposium on Solid Freeform Fabrication*. 2002. Austin, TX.
66. Cao, W.B., et al., *Development of freeform fabrication method for Ti-Al-Ni intermetallics*. Intermetallics, 2002. 10(9): p. 879-885.
67. Wenbin, F., et al., *Microstructure and properties of a TiAl alloy prepared by mechanical milling and subsequent reactive sintering* Materials Science and Engineering A, 2005. 403(1-2): p. 186-190.
68. Shishkovsky, I.V., et al., *Laser-induced combustion synthesis of 3D functional materials: computer-aided design*. Journal of materials chemistry, 2004. 14: p. 3444-3448.
69. Cagran, C., et al., *Thermophysical properties of a Ti-44%Al-8%Nb-1%B alloy in the solid and molten states* Intermetallics, 2003. 11(11-12): p. 1327-1334.
70. Matsugi, K., et al., *Microstructure of spark sintered titanium-aluminide compacts* Intermetallics, 1996. 4(6): p. 457-467.
71. Chandrasekeran, M. and Z.S. Xia, *Effect of alloying time and composition on the mechanical properties of Ti alloy* Materials Science and Engineering A, 2005. 394(1-2): p. 220-228.
72. Sujata, M., S. Bhargava, and S. Sangal, *On the formation of TiAl₃ during reaction between solid Ti and liquid Al*. Journal of materials science letters, 1997. 16: p. 1175-1178.
73. Lee, J.-M., et al., *Evolution of iron aluminide in Al/Fe in situ composites fabricated by plasma synthesis method* Materials Science and Engineering A, 2003. 362(1-2): p. 257-263.
74. Cao, W.B. and Y. Miyamoto, *Freeform fabrication of aluminum parts by direct deposition of molten aluminum*. journal of materials processing technology, 2006. 173(2): p. 209-212.

75. Ouyang, J.H., H. Wang, and R. Kovacevic, *Rapid Prototyping of 5356-aluminum alloy based on variable polarity gas tungsten arc welding: Process control and microstructure*. Materials and manufacturing process, 2002. 17(1): p. 103-124.
76. Matz, J.E., *Carbide formation in a nickel-based superalloy during electron beam solid freeform fabrication*, in *Materials Science and Engineering*. 1999, Massachusetts Institute of Technology: Cambridge MA. p. 94.
77. Taminger, K.M.B. and R.A. Hafley. *Characterization of 2219 aluminum produced by electron beam freeform fabrication*. in *Proceedings of solid freeform fabrication symposium*. 2002. Austin TX: University of Texas, Austin.
78. Watson, J.K., et al. *Development of a prototype low voltage electron beam freeform fabrication system*. in *13th solid freeform fabrication symposium*. 2002. Austin TX: University of Texas, Austin.
79. Ackelid, U., *The aluminum alloy 6061 produced with the arcam EBM process: A feasibility study*. 2006, Arcam AB: Molndal, Sweden. p. 1-10.
80. Sercombe, T.B. and G.B. Schaffer, *Rapid manufacturing of aluminum components*. Science, 2003. 301(5637): p. 1225-1227.
81. Sercombe, T.B. and G.B. Schaffer, *On the role of tin in the infiltration of aluminium by aluminium for rapid prototyping applications*. Scripta Materialia, 2004. 51(9): p. 905-908.
82. Avner, S.H., *Introduction to physical metallurgy*. 1997 ed. 1997: Tata McGraw Hill.
83. Li, J.R., et al., *Effect of dual-size mix on the stiffness and strength of open cell aluminum foams*. Materials Science and Engineering A, 2003. A362: p. 240-248.
84. Smith, D.R., J.B. Pendry, and M.C. Wiltshire, *Metamaterials and negative refractive index*. Science, 2004. 305: p. 788-792.
85. Cho, A., *Voila! Cloak of invisibility unveiled*. Science, 2006. 314: p. 403.
86. Johnson, S. and J. Joannopoulos, *Photonic Crystals: the road from theory to practice*. 2002, Boston, MA: Kluwer Academic Publishers.
87. Yang, S., et al., *Ultrasound tunneling through 3D Phononic Crystals*. Physical Review Letters, 2002. 10: p. 104301.

88. Pasko, A., et al., *Function representation in geomtric modeling: concepts, implementation and applications*. The Visual Computer, 1995. 11(8): p. 429-446.
89. Abboud, J.H., D.R.F. West, and R.D. Rawlings, *functionally gradiaent titanium-aluminide composites produced by laser cladding*. Journal materials science, 1994. 29: p. 3393-3398.
90. Ashby, M.F., et al., *Metal foams: a design guide*. 2000, UK Butterworth-heinemann.
91. Banhart, J., *Manufacturing Routes for Metallic Foams*. Jom, 2000. 52: p. 22-27.
92. Banhart, J. and J. Baumeister. *Production methods for metallic foams*. in *MRS Symposium Proceedings*. 1998.
93. Brothers, A.H. and D.C. Dunand, *Amorphous metal foams*. Scripta Materialia, 2006. 54: p. 513-520.
94. Deshpande, V. and N. Fleck, *High strain rate compressive behaviour of alluminum alloy foams*. International journal of Impact Engineering, 2000. 24(3): p. 277-298.
95. Hall, I., M. Guden, and C. Yu, *Crushing of aluminum closed cell foams: density and strain rate effects*. Scripta Materialia, 2000. 43(6): p. 515-521.
96. Medlin, D.J., et al., *Metallurgical characterization of a porous tantalum biomaterial (Trabecular Metal) for orthopaedic implant applications*, in *Materials & Processes from Medical Devices Conference*. 2004: Anaheim, CA; USA. p. 394-398.
97. Zhang, X., et al., *Combustion synthesis of porous materials for bone replacement*. Biomedical sciences instrumentation, 2001. 37: p. 463-468.
98. Chen, C., T. Lu, and N. Fleck, *Effects of imperfections in the yielding of two dimensional foams*. Journal of the mechanics and physics of solids, 1999. 47(11): p. 2235-2272.
99. Sugimura, Y., et al., *On the mechanical performance of closed cell Aluminum alloy foams*. Acta Materialia, 1997. 45: p. 5245-5259.
100. Gibson, L.J. and M.F. Ashby, *Cellular solids: Structure & properties*. 1988: Oxford: Pergamon Press.

101. Wadley, H.N.G., *Cellular Metals Manufacturing*. Advanced Engineering Materials, 2002. 4(10): p. 726-733.
102. Li, J.P., et al., *Porous Ti6Al4V scaffold directly fabricating by rapid prototyping: preparation and in vitro experiment*. Biomaterials, 2006. 27(8): p. 1223-1235.
103. Wen, C.E., et al., *Novel titanium foam for bone tissue engineering*. Journal of Materials Research, 2002. 17: p. 2633-2639.
104. Kusakabe, H., et al., *Osseointegration of a hydroxyapatite-coated multilayered mesh stem*. Biomaterials, 2004. 25: p. 2957-2969.
105. Melican, M.C., et al., *Three-dimensional printing and porous metallic surfaces: A new orthopedic application*. Journal of Biomedical Material Research, 2001. 55: p. 194-202.
106. Reyrier, M., F. Kircher, and B. Levesy. in *Advances in Cryogenic Engineering: Proceedings of the International Cryogenics Materials Conference*. 2002: American Institute of Physics.
107. Tritt, T.M., *Thermal Conductivity: Theory Property and Applications*. 2004: Kluwer Academic/Plenum Publishers, New York.
108. Tritt, T., *Thermal Conductivity: Theory, Properties and Applications*. 2004: Kluwer Academic/ Plenum Publishers.
109. Porter, D.A. and K.A. Easterling, *Phase Transformations in Metals and Alloys*. 2nd ed. 2004, Boca Raton: CRC Press. 366-372.
110. Fan, Y., et al., *Effect of phase transformations on laser forming of Ti-6Al-4V alloy*. Journal of Applied Physics, 2005. 98(013518): p. 1-10.
111. Tarin, P., et al., *Characterization of the $\alpha \leftrightarrow \beta$ transformations in a Ti-6Al-2Sn-4Zr-6Mo (wt%) alloy*. Materials Science and Engineering A, 2008. 481-482: p. 559-561.
112. Tarin, P., et al., *Transformations in the Ti-5Al-2Sn-2Zr-4Mo-4Cr (Ti-17) alloy and mechanical and microstructural characteristics*. Materials Science and Engineering A, 2006. 438-440: p. 364-368.
113. Mohandas, T., D. Banerjee, and V.V.K. Rao, *Fusion Zone Microstructure and Porosity in Electron Beam Welds of an $\alpha + \beta$ Titanium Alloy*. Mechanical and Materials Transactions, 1999. 30A(3): p. 789-798.

114. Frigola, P., et al. *A Novel fabrication technique for the production of RF Photoinjectors*. in *11th European Particle Accelerator Conference*. 2008. Genoa, Italy.
115. Frigola, P., et al. *Development of Solid Freeform Fabrication (SFF) for the production of RF Photoinjectors*. in *Particle Accelerator Conference*. 2009. Vancouver Canada.
116. Taylor, L.A. and T.T. Meek, *Microwave sintering of Lunar Soil: Properties theory and practise*. *Journal of Aerospace Engineering*, 2005. 18(3): p. 188-196.
117. Goldstein, J., et al., *Scanning electron microscopy and X-ray microanalysis*. third edition ed. 2003: Springer.
118. Griffiths, D.J., *Introduction to electrodynamics*. third ed. 1999: Prentice-Hall Inc.
119. Drouin, D., et al., *CASINO: Monte Carlo Simulations of electron trajectories in solids*. 2001, University of Sherbrooke: Sherbrooke, Quebec, CANADA.
120. Simchi, A., *Direct laser sintering of metal powders: Mechanism, kinetics and microstructural features*. *Materials Science and Engineering A*, 2006. 428: p. 148-158.
121. AB, S.m.f.E.u.a.A., *Mikael Wassmur, Arcam AB*. 2008: Gothenburg, Sweden.
122. *COMSOL Multiphysics Model Library*. Vol. Version 3.4: COMSOL AB.
123. *COMSOL Script User's Guide*. Version 3.4 ed: COMSOL AB.
124. Feynman, R., R. Leighton, and M. Sands, *The Feynman Lectures on Physics*. Vol. 1: Addison-Wesley Publishing Company Inc.